UNIVERSITY OF CALIFORNIA

SANTA CRUZ

CARBON ISOTOPES AS TOOLS FOR UNDERSTANDING NATURAL AND ENGINEERED OCEAN ALKALINITY ENHANCEMENT

A dissertation submitted in partial satisfaction of the

requirements for the degree of

DOCTOR OF PHILOSOPHY

in

EARTH SCIENCES

by

Ryan A. Green

March 2025

The Dissertation of Ryan A. Green
is approved:

Professor Mathis P. Hain, Chair

Professor Patrick A. Rafter

Professor Christopher A. Edwards

Professor James C. Zachos

Peter Biehl
Vice Provost and Dean of Graduate Studies

Table of Contents

List of Figures

List of Tables

Abstract

Carbon Isotopes as Tools for Understanding Natural and Engineered Ocean Alkalinity Enhancement

by

Ryan A. Green

Carbon isotopes serve as powerful tools for understanding ocean carbon cycle processes, both past and present. This dissertation investigates two distinct applications of carbon isotopes in the context of ocean alkalinity enhancement (OAE): as tracers of natural geologic carbon and alkalinity release in the past, and as monitoring tools for future carbon dioxide removal. Using a combination of global and regional modeling approaches paired with geochemical data, this work provides new insights into both geologic carbon release during the last deglaciation and verification methods for future ocean-based carbon removal.

In Chapters 1 and 2, I investigate records of anomalously low (^{14}C) water in the eastern tropical North Pacific Ocean during the last deglaciation. First, through global carbon cycle modeling constrained by atmospheric CO_2 and Δ^{14}C records, I establish that large-scale release of neutralized geologic carbon (up to 2,400 Pg C) could have occurred without significantly disrupting the carbon cycle. Building on this, I develop a regional model of the eastern tropical North Pacific and combine it with new boron isotope (δ^{11}B) data to directly simulate these anomalies, demonstrating that this carbon release must have been neutralized by alkalinity—representing a natural analog for OAE.

In Chapter 3, I shift focus to the present day, examining how carbon isotopes can support modern climate solutions. Using a high-resolution regional model of the California Current System, I evaluate the utility of stable carbon isotopes (δ^{13}C) as a tool for verifying atmospheric CO_2 uptake following OAE deployment. This work demonstrates that δ^{13}C provides a diagnostic signal of CO_2 removal that persists longer than traditional carbonate measurements, offering a robust verification method for marine carbon dioxide removal.

Together, these chapters advance our understanding of both past ocean carbon cycle processes and future carbon removal strategies, while highlighting the versatility of carbon isotopes as tools for studying natural and engineered perturbations to the marine carbon cycle.

Acknowledgments

This dissertation would not have been possible without the guidance, support, and encouragement of many remarkable people who have accompanied me on this journey.

First and foremost, I am deeply grateful to my advisors, Mathis Hain and Pat Rafter, for their invaluable mentorship, patience, and unwavering support throughout my Ph.D. Their insights, thoughtful feedback, and encouragement have shaped my scientific thinking and helped me navigate the challenges of this research. Beyond their roles as advisors, I am thankful for the friendship I have developed with both of them. Our conversations, shared enthusiasm for science, and mutual respect have made this journey all the more meaningful.

I am also deeply grateful to Chris Edwards, whose guidance was instrumental in my journey to learning regional ocean modeling for Chapter 3. His expertise not only elevated the quality of this dissertation but has laid a foundation for my future career. Beyond his scientific mentorship, Chris's generous commitment of time and his genuine dedication to student success have been truly inspiring. His example of balancing scientific rigor with compassionate teaching is something I hope to carry forward in my own professional path.

I am profoundly grateful to my small but supportive lab community—Terra, David, and Colin—who made the lab a place of both collaboration and friendship. A special thanks goes to Terra, whose companionship in both science and life made the challenges of graduate school—and life in general—a lot easier to navigate. Whether we were tackling tricky research questions, venting about the ups and downs of grad school, or taking walks through the redwoods to clear our heads, her support and friendship made my time here especially meaningful. Together, the three of them helped create a lab environment filled with curiosity, encouragement, and humor that made it a truly special place to work.

To my friends outside of the lab, thank you for keeping me grounded and providing much-needed breaks from research. The ski trips to Tahoe, the long volleyball days, and

the late softball nights all contributed immensely to my well-being and made this time genuinely enjoyable. These moments of joy and connection sustained me through the challenges of graduate school and, quite simply, made me happier.

I extend my heartfelt gratitude to my family, especially my mom, whose unconditional support and belief in me have been my foundation. She celebrated every milestone and provided comfort during every setback, and this achievement is as much hers as it is mine.

I must also acknowledge the beauty of Santa Cruz itself, which has been a constant source of inspiration and solace. Searching for whales while commuting home along the bike path and taking contemplative walks along West Cliff Drive provided much-needed perspective and tranquility during the most demanding periods of this journey. The beauty of the ocean and redwoods served as a constant reminder of why I pursued the earth and ocean sciences in the first place.

Finally, I am grateful to the broader scientific community for fostering a culture of curiosity, rigor, and discovery. At its core, science is a relentless pursuit of understanding—a means of uncovering the underlying mechanisms that shape our world. This shared endeavor, driven by collective inquiry and a commitment to truth, has been a continuous source of inspiration throughout my doctoral studies. While the work of researchers dedicated to addressing climate change is particularly motivating, what sustains my passion is the deeper, universal impulse to explore, question, and make sense of complexity. It is this fundamental drive—the pursuit of knowledge for its own sake and for the betterment of society—that I hope to carry forward not only in my scientific career but in a lifelong commitment to learning, discovery, and intellectual growth in all aspects of life.

Contributions to this work: Mathis Hain and Pat Rafter supervised the research that forms the basis for this dissertation. The text of this dissertation includes a reprint of the following previously published material:

> Green, R. A., Hain, M. P., and Rafter, P. A. (2024). Deglacial pulse of neutralized carbon from the Pacific seafloor: A natural analog for ocean alkalinity enhancement? *Geophysical Research Letters*, 51, e2024GL108271.

Introduction

The ocean plays a fundamental role in Earth's carbon cycle, containing approximately 38,000 Gt C—roughly 45 times more carbon than the present atmosphere (Friedlingstein et al., 2022) (1 Gt = 1 billion metric tons). This vast reservoir has already absorbed nearly 40% of anthropogenic CO_2 emissions since the industrial revolution (Sabine & Tanhua, 2010), highlighting the ocean's crucial role in moderating climate change. While natural ocean processes and weathering will eventually draw down atmospheric CO_2, these processes operate over hundreds of thousands of years (Archer et al., 2009; Lord et al., 2016)—far too slowly to address our immediate climate crisis. Meeting global climate targets requires both rapid emissions reductions and active carbon dioxide removal within decades, not millennia (Lee et al., 2023; Masson-Delmotte et al., 2021).

As the need for gigaton-scale carbon dioxide removal (CDR) becomes increasingly clear (Lee et al., 2023; Masson-Delmotte et al., 2021), the ocean—covering 71% of Earth's surface—must play a central role in these efforts (NASEM, 2021; NOAA, 2023). Among proposed marine CDR approaches, ocean alkalinity enhancement (OAE) has emerged as a promising strategy with a high theoretical CO_2 sequestration potential of 3–30 Gt CO_2 $yr^{-}1$ (Feng et al., 2017; Köhler et al., 2013; Renforth & Henderson, 2017). OAE aims to accelerate natural weathering processes by adding alkaline minerals to the surface ocean, either in a crushed or dissolved form (NASEM, 2021; Oschlies et al., 2023). While the theoretical potential of OAE is well established, scaling up deployment requires both advancing our fundamental understanding and developing robust monitoring and verification approaches. One valuable path forward is studying natural analogs, which provide real-world examples of relevant processes operating at meaningful scales (Bach & Boyd, 2021). Equally important is developing verification methods that can reliably

detect and quantify CO_2 removal against the dynamic background variability of the marine carbonate system (Ho et al., 2023).

To address these challenges, we need tools that can both identify past instances of alkalinity addition and verify carbon uptake after modern OAE deployment. Carbon isotopes provide a powerful approach to addressing both objectives. Isotopes are variants of an element that contain the same number of protons but different numbers of neutrons, resulting in different atomic masses. Carbon has three naturally occurring isotopes: ^{12}C, the most abundant form (98.9%); ^{13}C, a stable isotope comprising about 1.1% of natural carbon; and ^{14}C, a rare, radioactive isotope that decays with a half-life of 5,730 years. These isotopes behave slightly differently in physical, chemical, and biological processes, leading to measurable variations in their relative abundances across different carbon reservoirs. These differences create isotopic "fingerprints" that allow scientists to track its movement through Earth's reservoirs over time.

^{13}C is particularly useful for studying the carbon cycle because isotopic fractionation causes its ratio to ^{12}C to vary across different reservoirs. Biological processes, such as photosynthesis, preferentially assimilate the lighter isotope, ^{12}C, leaving organic matter and fossil fuels depleted in ^{13}C relative to atmospheric and oceanic carbon. These fractionation effects create distinct isotopic signatures, making $\delta^{13}C$ a powerful tool for identifying carbon sources, tracking ocean-atmosphere CO_2 exchange, and reconstructing past biogeochemical changes. The $\delta^{13}C$ notation quantifies this variability by expressing the deviation of a sample's $^{13}C/^{12}C$ ratio from an internationally recognized standard.

Long-term records of $\delta^{13}C$ from marine carbonates and sedimentary organic matter have been instrumental in assessing past shifts in ocean circulation, biological productivity, carbon storage, and atmospheric CO_2 levels (Westerhold et al., 2020; Zachos, 2001). Additionally, the depletion of $\delta^{13}C$ in atmospheric and oceanic carbon—known as the Suess Effect—demonstrates how fossil fuel-derived CO_2 has altered Earth's carbon cycle (Keeling, 1979). This same principle can be applied to OAE: because atmospheric CO_2 has a distinct $\delta^{13}C$ signature, changes in oceanic $\delta^{13}C$ following OAE deployment could provide a measurable fingerprint of atmospheric carbon uptake. If OAE effectively moves CO_2 from the atmosphere and into the ocean, the added carbon should carry this

isotopic signature, offering a potential tool for verifying and quantifying oceanic carbon sequestration. This makes $\delta^{13}C$ a promising candidate for monitoring the effectiveness of OAE.

Unlike ^{13}C, ^{14}C is radioactive, allowing it to act as a natural clock for tracking carbon movement over time. Since ^{14}C is only produced in the atmosphere while simultaneously decaying at a known rate, its presence (or absence) in a particular carbon reservoir provides insight into how long that carbon has been separated from the atmosphere. This property makes ^{14}C especially valuable for determining the ventilation age of deep ocean waters, dating marine sediments, and reconstructing past ocean circulation patterns.

For example, sediment records from the Eastern Tropical North Pacific during the last deglaciation reveal extremely low $\Delta^{14}C$ values (Lindsay et al., 2016; Marchitto et al., 2007; Rafter et al., 2018, 2019), indicating the presence of ancient, carbon-rich water masses. Although initially attributed to a slowdown in ocean circulation, the degree of ^{14}C depletion is too extreme to be explained by circulation alone (Hain et al., 2011). Instead, this anomaly suggests the addition of ^{14}C-depleted carbon, likely neutralized by alkalinity (Rafter et al., 2019; Skinner & Bard, 2022)—potentially providing a natural analog for OAE. If large-scale alkalinity addition occurred naturally in the past, it could serve as critical empirical evidence for assessing the feasibility, risks, and long-term impacts of engineered OAE deployment.

Despite these insights, key uncertainties remain: Was this low $\Delta^{14}C$ water caused by a natural OAE analog? If so, what can it reveal about future OAE deployment? And can carbon isotopes serve as reliable monitoring tools for OAE in a dynamic ocean environment? **The overarching aim of this dissertation is to leverage carbon isotopes as tools to better understand both natural and engineered alkalinity addition in the ocean.**

Through a combination of global and regional modeling approaches, paired with isotopic constraints, this work bridges paleoceanographic observations with modern carbon removal strategies. **Chapter 1** investigates the feasibility of large-scale neutralized carbon release during the last deglaciation using global carbon cycle modeling constrained by atmospheric CO_2 and $\Delta^{14}C$ records. This work establishes fundamental constraints on both the magnitude of carbon release possible within the global radiocarbon budget

and the amount of alkalinity required to neutralize this carbon. **Chapter 2** builds on these findings by developing a regional model of the eastern tropical North Pacific to directly simulate observed radiocarbon anomalies, complemented by new boron isotope (δ^{11}B; ratio of ^{11}B to ^{10}B) measurements. Together, these results demonstrate that the deglacial radiocarbon anomalies can only be explained by carbon release that was neutralized by alkalinity—providing evidence for a natural OAE analog during the last deglaciation. **Chapter 3** shifts the focus to modern climate solutions by evaluating stable carbon isotopes (δ^{13}C) as a verification tool for OAE. Using a high-resolution regional ocean model of the California Current System, I first show that OAE effectively removes carbon from the atmosphere and then demonstrate that δ^{13}C measurements provide a persistent diagnostic signal of that net CO_2 uptake that outlasts other traditional carbonate system measurements. This work assesses the detectability of various chemical parameters against background variability and measurement precision to inform future monitoring strategies for OAE.

By integrating isotope-based insights across past and present carbon cycle dynamics, this dissertation advances our understanding of both paleoceanographic processes and modern carbon removal strategies. The findings not only reinforce the plausibility of large-scale neutralized carbon fluxes in the ocean's past but also demonstrate the practical utility of isotopes for monitoring future OAE deployments.

Chapter 1

Deglacial Pulse of Neutralized Carbon From the Pacific Seafloor: A Natural Analog for Ocean Alkalinity Enhancement?

This chapter is a reproduction of an article published in *Geophysical Research Letters*: Green, R. A., Hain, M. P., & Rafter, P. A. (2024). Deglacial pulse of neutralized carbon from the Pacific seafloor: A natural analog for ocean alkalinity enhancement? *Geophysical Research Letters*, 51, e2024GL108271. Supplemental data can be accessed at https://doi.org/10.1029/2024GL108271.

1.1 Abstract

The ocean carbon reservoir controls atmospheric CO_2 on millennial timescales. Radiocarbon (^{14}C) anomalies in eastern North Pacific sediments suggest a significant release of geologic ^{14}C-free carbon at the end of the last ice age but without evidence of ocean acidification. Using inverse carbon cycle modeling optimized with reconstructed atmospheric CO_2 and $^{14}C/^{12}C$, we develop first-order constraints on geologic carbon and alkalinity release over the last 17.5 thousand years. We construct scenarios allowing

the release of 850–2,400 Pg C, with a maximum release rate of 1.3 Pg C yr^{-1}, all of which require an approximate equimolar alkalinity release. These neutralized carbon addition scenarios have minimal impacts on the simulated marine carbon cycle and atmospheric CO_2, thereby demonstrating safe and effective ocean carbon storage. This deglacial phenomenon could serve as a natural analog to the successful implementation of gigaton-scale ocean alkalinity enhancement, a promising marine carbon dioxide removal method.

1.2 Introduction

Global climate, the global carbon cycle, and the atmospheric concentration of the greenhouse gas CO_2 have been tightly coupled over recent ice age cycles (Siegenthaler et al., 2005), including the relatively abrupt ice age terminations and deglacial periods (Marcott et al., 2014; Shakun et al., 2012). Coupled changes in deep ocean circulation, polar ocean biological nutrient consumption, and air-sea CO_2 exchange are thought to be the dominant drivers of the observed CO_2 change (Khatiwala et al., 2019; Rafter et al., 2022; Sigman et al., 2021), but changes in land carbon storage and seafloor carbon burial in direct response to climate change are also clearly implicated (Cartapanis et al., 2018; Joos et al., 2001; Köhler et al., 2014). The primary challenge to all these hypotheses comes from unexplained "anomalies" in the radiocarbon (^{14}C) content within marine foraminifera during deglacial CO_2 rise in the atmosphere, between about 18,000 and 11,500 years before 1950 (18–11.5 thousand years before present or kyr BP, Figure 1.1). These deglacial records of ^{14}C depletion (decay-corrected ^{14}C:^{12}C ratio, expressed as $\Delta^{14}C$; Stuiver and Polach, 1977) have been uncovered throughout the intermediate-depth (>500 m & <1,000 m) eastern tropical North Pacific (ETNP) Ocean (Lindsay et al., 2016; Marchitto et al., 2007; Rafter et al., 2018, 2019; L. Stott et al., 2009); associated with the weakly ventilated Pacific shadow zone (Gehrie et al., 2006; Holzer et al., 2021).

These regional depletions in seawater $\Delta^{14}C$ were initially attributed to a release of dissolved inorganic carbon (DIC) that had been sequestered for thousands of years in the abyssal ocean, hinting at deglacial changes in ocean circulation (Bova et al., 2018; W. Broecker & Barker, 2007; W. Broecker, 2009; Marchitto et al., 2007). However,

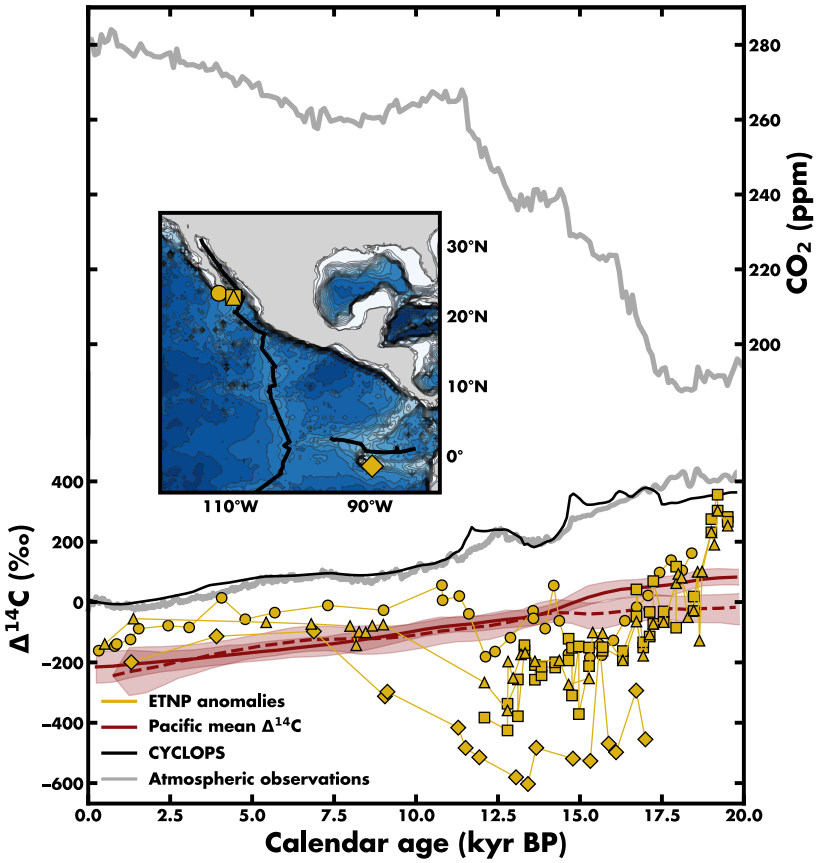

Figure 1.1: Unexplained Δ^{14}C anomalies from the intermediate-depth (>500 m and <1,000 m) eastern tropical North Pacific (ETNP). The ETNP anomalies shown are foraminifera from Marchitto et al. (2007) (benthic; circles), Stott et al. (2009) (benthic; diamonds), and Rafter et al. (2018) (squares for benthic, triangles for planktic). The ETNP anomalies are compared with compilation means from the Pacific (red lines; Rafter et al., 2022). Solid and dashed lines represent mid-depth and bottom water, respectively, with red shading denoting the 95% confidence interval. The atmospheric Δ^{14}C for our CYCLOPS control simulation is shown as a solid black line. Reconstructed Δ^{14}C (Reimer et al., 2020) and CO_2 (Bereiter et al., 2015) are shown in gray. Individual Δ^{14}C records are overlaid on ocean bathymetry (blue contours) and tectonic spreading centers (black lines) in the map inset.

this ocean release interpretation has two main shortcomings (Hain et al., 2011): (a) the Last Glacial Maximum (LGM) deep ocean was not sufficiently ^{14}C-depleted (dashed red line in Figure 1.1) to be the source of the mid-depth anomalies, and (b) once the isotopic signature of anomalously ^{14}C-depleted carbon is transported to the mid-depth Pacific it would rapidly dissipate into the global carbon cycle via ocean circulation and

air-sea gas exchange. This hypothesis is further contradicted by a new compilation showing no appreciable ^{14}C-depletion at any depth for the basin-scale Pacific during the deglaciation (red lines in Figure 1.1; Rafter et al., 2022), as would be required if the abyssal ocean caused the ETNP ^{14}C anomalies. Additionally, deep-sea coral ^{14}C records from the Galápagos with excellent age model controls (Chen et al., 2020) and South Pacific ^{14}C records bathed in modern Antarctic Intermediate Water (De Pol-Holz et al., 2010; Rose et al., 2010; Siani et al., 2013; Zhao & Keigwin, 2018) show no ^{14}C-depletion comparable to the ETNP anomalies. This lack of basin-wide mid-depth Δ^{14}C depletion is an important observational constraint we will consider below.

An alternative set of proposals suggests these anomalously low Δ^{14}C values reflect an addition of ^{14}C-free carbon from a geologic source (Rafter et al., 2018, 2019; Ronge et al., 2016; Skinner & Bard, 2022; L. Stott & Timmermann, 2011; L. Stott et al., 2009). A common objection to this hypothesis is the potential for ocean acidification, which would contradict the evidence of ETNP carbonate preservation during the last deglacial (Lindsay et al., 2015; Marchitto et al., 2007; Ortiz et al., 2004; Rafter et al., 2019; Skinner & Bard, 2022; L. Stott et al., 2009). However, if a proportional influx of alkalinity neutralized the geologic carbon—e.g., carbon introduced in the form of "neutralized" bicarbonate ion instead of "acidic" CO_2—there would be muted effects on seawater pH, $CaCO_3$ burial, and atmospheric CO_2 (Rafter et al., 2019).

Neutralized ^{14}C-free carbon could be generated within marine sediments via metamorphic or hydrothermal processes (Rafter et al., 2019; Skinner & Bard, 2022). Subsequently, it would be transported and dispersed throughout the ocean and atmosphere, leading to the dilution of the atmospheric ^{14}C reservoir and a reduction of atmospheric Δ^{14}C. While the majority of the atmospheric Δ^{14}C decline during the last

deglaciation has been attributed to Southern Ocean CO_2 release, changes in Atlantic circulation, and a decline in cosmogenic ^{14}C production due to a strengthening of Earth's magnetic field (black line in Figure 1.1; Hain et al. (2014) and Skinner and Bard (2022)), these processes alone do not fully account for changes observed in reconstructed atmospheric Δ^{14}C records (Reimer et al., 2020). This discrepancy indicates a possible opportunity within the planetary ^{14}C budget for ^{14}C-free geologic carbon addition.

This study presents the first carbon cycle model results investigating the possibility of

coupled geologic carbon and alkalinity release during the last deglaciation. Our experiments build on the deglacial model scenario of (2014) and test the sensitivity of our results to changes in terrestrial carbon storage. We use a stepwise numerical model optimization method that assimilates observed atmospheric CO_2 and $\Delta^{14}C$ data to find the internally consistent rates of geologic carbon and alkalinity release, permafrost carbon destabilization, and land biosphere regrowth. This is intended to raise important questions relevant to different fields of research: can seafloor spreading centers respond to climate change? What subsurface processes could mobilize carbon and alkalinity at relevant specific rates? And do deglacial radiocarbon anomalies provide a natural analog for purposeful ocean alkalinity enhancement (OAE) as a means of marine carbon dioxide removal (Bach & Boyd, 2021; NASEM, 2021)?

1.3 Methods

Motivated by the regional ETNP anomalies (Figure 1.1), we use the CYCLOPS global carbon cycle model (Hain et al. (2010, 2011, 2014) and Keir (1988); see Text S1 in Supporting Information S1 for model configuration) to simulate the flux of geologic carbon from Pacific mid-ocean ridge systems. This involves four experiments, progressively adding optimized open-system carbon and alkalinity fluxes, along with an imposed initial ^{14}C inventory change (top row of Figure 1.2): (a) We invert for the optimal rates of carbon and alkalinity release to the intermediate-depth (200–1500m) North Pacific region of the model (experiment NP); (b) We add the possibility of land carbon uptake to the optimization (experiment NP + LC); (c) We include the release of ^{14}C-free permafrost carbon to the atmosphere (experiment NP + LC + PF); and (d) We adjust the initial LGM ^{14}C inventory by +3.5% to account for the uncertain history of Earth's magnetic field, ^{14}C production, and reconstructed $\Delta^{14}C$ near the LGM (Figure 1.3a, Dinauer et al. (2020) and Roth and Joos (2013)) (experiment NP + LC + PF + RC).

All experiments include the identical background forcings of the control run, based on the deglacial carbon cycle scenario from (2014). Although this is an idealized model scenario, we use it as our starting point because the LGM carbon cycle forcing of CYCLOPS is well documented (Hain et al., 2010) and consistent with reconstructed surface ocean pH changes (Chalk et al., 2017; Hain et al., 2018). Additionally, the deglacial model scenario

agrees reasonably well with subsequent ^{14}C measurements and data compilations (Rafter et al., 2022; Zhao & Keigwin, 2018), as shown by the direct comparison for the Pacific and all other basins (Figure S1 in Supporting Information S1). More in-depth descriptions of each experiment can be found in Text S3 of Supporting Information S1.

For all experiments, the optimized open-system carbon and alkalinity fluxes were determined by a numerical algorithm that minimizes the deviation between simulated atmospheric CO_2 ($CO_2{}^{model}$) and $\Delta^{14}C$ ($\Delta^{14}C^{model}$), compared to reconstructed atmospheric CO_2 ($CO_2{}^{obs}$) from the most recent compilation of Antarctic ice core CO_2 data (Bereiter et al., 2015) and $\Delta^{14}C$ ($\Delta^{14}C^{obs}$) from IntCal20 (Reimer et al., 2020). The algorithm's objective function f is scaled to the 90ppm glacial/interglacial CO_2 range and the $\sim$250‰ atmospheric $\Delta^{14}C$ change after accounting for Earth's magnetic field strengthening:

$$f(CO_2, \Delta^{14}C) = \frac{|CO_2^{obs} - CO_2^{model}|}{90\text{ppm}} + \frac{|\Delta^{14}C^{obs} - \Delta^{14}C^{model}|}{250‰}$$

We do not permit unrealistic 'negative' geologic fluxes, permafrost growth, or land carbon contraction that could otherwise help the model align with the observations. For experiments that include land carbon uptake, we included a deliberate heuristic favoring land carbon uptake during the Holocene. If CO_2 model was greater than CO_2 obs and the atmospheric $\Delta^{14}C$ model-data misfit was less than 20‰, then the optimized carbon flux is added to the terrestrial biosphere rather than the intermediate-depth North Pacific (with an alkalinity flux of zero). For experiments that include carbon release from permafrost destabilization, the optimized flux is only activated when the optimization algorithm would otherwise add CO_2 (ALK-to-DIC$<$0.5) into the intermediate-depth North Pacific, instead releasing the equivalent amount of CO_2 directly to the atmosphere. Further algorithm details can be found in Text S2 of Supporting Information S1.

1.4 Results

1.4.1 Atmospheric Constraints on Geologic Carbon Addition

All four simulations improve the overall CO_2 and $\Delta^{14}C$ model-data misfit compared to the control run (blue vs. black line, Figure 1.2). This model-data misfit is progressively minimized as more open-system carbon and alkalinity fluxes are added, with the NP + LC + PF + RC simulating the smallest model-data misfit. Each simulation has two main pulses of geologic carbon, one during the deglaciation and one smaller pulse during the Holocene. Our optimization triggers these geologic pulses when $\Delta^{14}C$ model rises above $\Delta^{14}C$ obs, which we call ^{14}C opportunities. Most geologic carbon is added as bicarbonate ion (61%–84%, Table S1 in Supporting Information S1), with net ALK-to-DIC ratios between 1.08 and 1.19 (Table S1 in Supporting Information S1) across all four simulations.

For our first three experiments (NP, NP + LC, NP + LC + PF)–which include no adjustment to the initial ^{14}C inventory–a total of 846–929 Pg C geologic carbon was added over the 20-kyrs (Table S1 in Supporting Information S1), with peak rates as large as 0.9 Pg C yr^{-1} (Figures 2i–2k) during the first pulse of addition (∼15-kyr BP). Of those experiments that included terrestrial regrowth (NP + LC, NP + LC + PF), simulated carbon uptake is between 279 and 300 Pg C (Table S1 in Supporting Information S1), mainly during the Holocene. When we include terrestrial carbon release from permafrost thaw (NP + LC + PF), 105 Pg C (Figure 1.2k, Table S1 in Supporting Information S1) is released around 16-kyr BP during the first pulse of carbon addition. Our fourth experiment, NP + LC + PF + RC, includes an adjusted ^{14}C inventory at the LGM initial state alongside all the above open-system fluxes. The higher initial $\Delta^{14}C$ model increases the opportunity for the subsequent addition of ^{14}C-free carbon, leading to a greater amount of total carbon added (2,396 Pg C, Table S1 in Supporting Information S1), higher release rates (up to 1.3 Pg C yr^{-1}, Figure 1.2l), more land carbon uptake (550 Pg C; Table S1 in Supporting Information S1), but a similar carbon release from permafrost thaw around 16-kyr BP (97 Pg C).

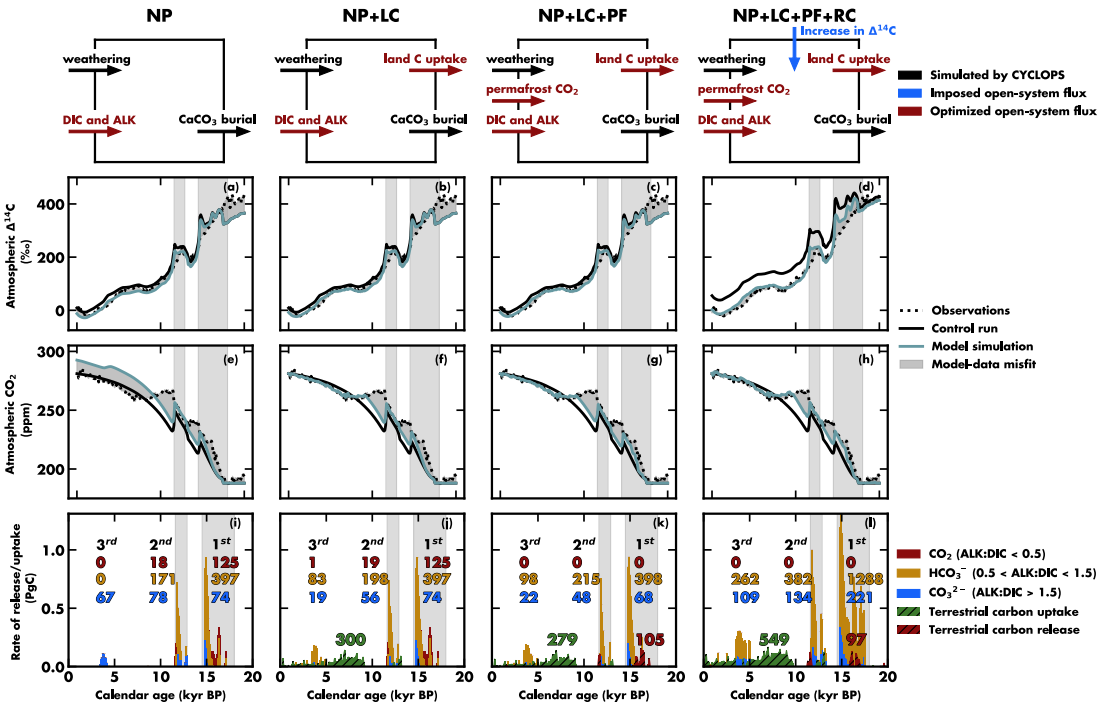

Figure 1.2: Simulated atmospheric response to optimized geologic carbon release scenarios. The top row illustrates our experimental design that progressively introduces optimized and imposed open-system fluxes (colored arrows). Subsequent rows illustrate simulation results for atmospheric $\Delta^{14}C$ (a–d), atmospheric CO_2 (e–h), and carbon release/uptake rates (i–l). In panels (i–l), colored numbers represent the amounts of CO_2 (red), HCO_3^- (yellow), and CO_3^{2-} (blue) released with each geologic carbon pulse. Similarly, terrestrial carbon uptake (regrowth) is shown in green, and terrestrial carbon release (permafrost destabilization) is in red, all in units of Pg C. Gray bars denote Heinrich Stadial 1 and Younger Dryas, while model-data misfit is shaded in gray.

1.4.2 Regional and Bulk Ocean Impacts From Large-Scale Geologic Carbon Addition

The most severe carbon cycle impacts should arise during our largest geologic carbon addition scenario (NP + LC + PF + RC). However, only minor $\Delta^{14}C$ anomalies are simulated in the intermediate-depth North Pacific box where the carbon is released (solid blue line, Figure 1.3a). Consequently, the simulated intermediate-depth North Pacific $\Delta^{14}C$ is in broad agreement with the mean $\Delta^{14}C$ from the mid-depth (neutral density of 27.5–28 kg m^{-3}) Pacific, calculated from a new proxy ^{14}C:^{13}C compilation (red line in Figure 1.3a and Rafter et al. (2022)). Given that the present-day mid-depth Pacific contains the oldest waters in the ocean, it serves as a conservative benchmark

for comparing our simulated intermediate-depth results. Furthermore, the lack of severe $\Delta^{14}C$ depletion in the NP + LC + PF + RC simulation is supported by a deep-sea coral record considered representative of the ^{14}C content of intermediate waters near the Galápagos islands (red circles in Figure 1.3a and Chen et al. (2020)).

Similarly, we find limited impacts on deep ocean [CO_3^{2-}] –which largely determines $CaCO_3$ saturation and thus $CaCO_3$ burial–when the geologic carbon is added as HCO_3^- (ALK-to-DIC $\sim$ 1). This is clear from Figure 1.3b and as the NP + LC + PF + RC only simulates a moderate increase ($\sim$5 μmol kg^{-1}) in deep-ocean [CO_3^{2-}] compared to the control simulation. With a deglacial increase in deep-ocean [CO_3^{2-}] due to a weakened biological pump and a subsequent decrease in deep-ocean [CO_3^{2-}] from carbonate compensation, both the control and NP + LC + PF + RC simulation broadly follow [CO_3^{2-}] observations (Yu et al., 2010, 2013).

In addition to $\Delta^{14}C$ impacts, geologic carbon will impact the ocean's stable isotope ratio of carbon (^{13}C:^{12}C, reported as $\delta^{13}C$), but this ultimately depends on the source. We run an additional set of experiments by calculating the bulk ocean $\delta^{13}C$ change for two endmember sources of neutralized geologic carbon (described in Text S4 of Supporting Information S1): bicarbonate from anaerobic oxidation of thermogenic methane (AOM; Rafter et al. (2019)) and geologic CO_2 neutralized by carbonate dissolution (Skinner & Bard, 2022), with $\delta^{13}C$ values of -25‰ and -2.5‰, respectively. When 2,396 Pg C is added (as suggested by our NP + LC + PF + RC experiment), we simulate bulk $\delta^{13}C$ ocean changes of -1.5‰ for AOM and -0.2‰ for carbonate dissolution.

Given that reconstructed oceanic $\delta^{13}C$ values have not fluctuated more than $\sim$1‰ over the last 800-kyrs (Hodell et al., 2003), our simulations suggest geologic carbon from a methane source ($\delta^{13}C \leq$ -25‰) is unlikely for our extreme carbon addition scenario of 2,396 Pg C. Considering the decoupled nature of neutralized geologic carbon addition and atmospheric CO_2, along with the limited impact on basin-scale $\Delta^{14}C$, deep ocean [CO_3^{2-}], and bulk ocean $\delta^{13}C$, these findings underscore that the global ^{14}C budget is the strongest constraint available for assessing geologic carbon addition at the global scale.

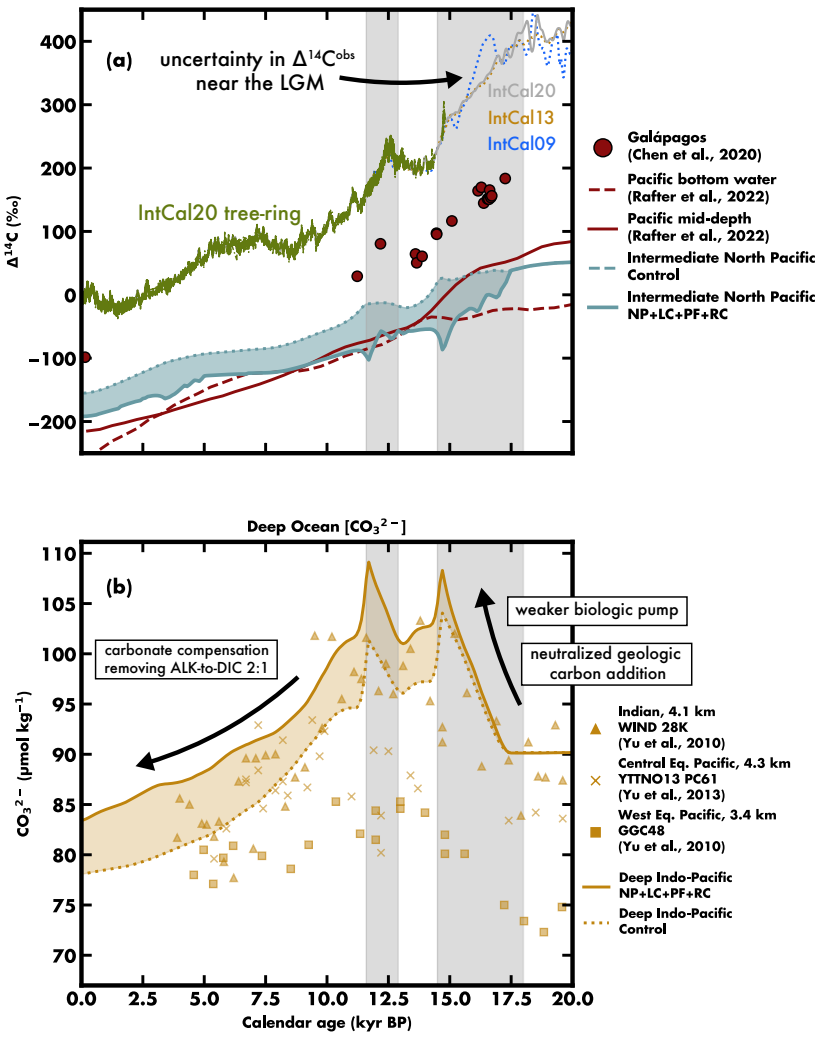

Figure 1.3: Neutralized carbon release has limited impacts on basin scale $\Delta^{14}C$ and deep ocean CO_3^{2-}. In Panel a, NP + LC + PF + RC drives mild $\Delta^{14}C$ depletion from the control run (shaded blue area), consistent with various data sets: deep-sea coral near the Galápagos (red circles), mean $\Delta^{14}C$ from Pacific mid-depth and bottom water (solid and dashed red line), and atmospheric $\Delta^{14}C$ (solid gray and green, dotted yellow and blue). There is a notable discrepancy in $\Delta^{14}C$ near the Last Glacial Maximum in the last three IntCal iterations before converging when tree-ring data becomes available (solid green line). Panel b illustrates NP + LC + PF + RC causing an increase in CO_3^{2-} in the Indo-Pacific deep ocean compared to the control run (shaded yellow). Simulated CO_3^{2-} align broadly with observations from the Indian (yellow triangle) and Equatorial Pacific (yellow square and X). Gray bars represent Heinrich Stadial 1 and Younger Dryas.

1.5 Discussion

1.5.1 Large Amounts of Bicarbonate Allowable

The core outcome of our study is that atmospheric CO_2 and $CaCO_3$ burial are effectively blind to carbon release neutralized by alkalinity in a ratio near 1:1, with the timely implication that OAE may be an effective pathway for the mitigation of anthropogenic carbon emissions (NASEM, 2021). In the specific context of the deglacial period, this insensitivity allows for large-scale geologic carbon addition scenarios constrained most directly by the planetary radiocarbon budget, as long as there was concomitant natural OAE. Additionally, our most extreme carbon addition scenario is insufficient to drive significant $\Delta^{14}C$ depletion across the North Pacific, which agrees with observations representative of the North Pacific and Pacific basins. This supports the idea that the enigmatic $\Delta^{14}C$ anomalies of the ETNP are likely regional or localized phenomena that could be exploited to derive a set of local constraints on possible carbon and alkalinity release that would be completely independent of the global CO_2 and ^{14}C budget constraints used in this study.

We optimized our carbon cycle modeling simulations, which include different open-system fluxes and changes to the ^{14}C inventory, with the addition of geologic carbon. The simulations show that up to 2,396 Pg of geologic carbon, mainly as HCO_3^-, can be consistent with the observed deglacial changes in atmospheric CO_2 and $\Delta^{14}C$. Due to the alkalinity accompanying DIC during HCO_3^- addition, geologic carbon in this form can be added at rates as large as 1.3 Pg C yr^{-1} (Figure 1.2l) with limited impacts on atmospheric CO_2 and deep-sea $[CO_3^{2-}]$.

Prior work has estimated that deglacial geologic CO_2 emissions from mantle decompression could have reached up to 0.2 Pg C yr^{-1} (Cartapanis et al., 2018; Roth & Joos, 2012), much smaller than our maximum yearly rates. However, these lower rates were derived assuming the geologic carbon came only as CO_2 rather than as HCO_3^-. When carbon is added without alkalinity (i.e., CO_2), atmospheric CO_2 and $CaCO_3$ burial constraints are highly sensitive to any carbon added to the system. However, when adding neutralized carbon (HCO_3^-), atmospheric CO_2 and $CaCO_3$ burial constraints become effectively blind to the carbon release, no longer constraining the carbon release rate or total. During HCO_3^- addition, the constraining factor shifts to the planetary ^{14}C

mass balance and its reflection in the atmospheric $\Delta^{14}C$ record (via IntCal20, Reimer et al. (2020)), which can indirectly record the dilution of ^{14}C-enriched environmental carbon by ^{14}C-free geologic carbon. This $\Delta^{14}C$obs constraint on HCO_3^- release leads to an upper bound of 800–1,000 Pg C in our first three simulations (NP, NP + LC, NP + LC + PF)—a 2%–2.5% increase of total ocean carbon inventory. Furthermore, if we take into consideration the uncertainty in the planetary ^{14}C mass balance (Dinauer et al., 2020; Roth & Joos, 2013) by increasing the initial LGM ^{14}C inventory by 3.5%, the opportunity for subsequent geologic carbon release increases to ∼2,500 Pg C (6.5% increase of total ocean carbon inventory). In other words, a higher initial LGM ^{14}C:/thirteenC can substantially increase the opportunity for ^{14}C-free geologic carbon release since the LGM.

Considering the idealized nature of our experiments and because of biases inherited from our control run (Hain et al., 2014), our optimization results should not be taken as estimates of geologic carbon release or of other simulated open-system carbon fluxes (e.g., LC, PF). Instead, we argue that geologic carbon release greater than 800–1000 Pg C is rendered unlikely, and release greater than 2,400 Pg C is implausible in the face of $\Delta^{14}C$obs. Further, if indeed there was substantial geologic carbon release since the LGM, it must have been in the neutralized form of HCO_3^- with a net ALK-to-DIC ratio near 1, as proposed by (2019), to avoid violating constraints from atmospheric CO_2 and $CaCO_3$ burial. Therefore, we argue that geologic carbon release played only a minor role in raising CO_2 at the end of the last ice age, even if the total amount of carbon release was substantial. This contrasts with prior deglacial geologic carbon addition research, which attributes glacial/interglacial CO_2 variability to liquid CO_2 release (L. Stott & Timmermann, 2011; L. Stott et al., 2019; L. D. Stott et al., 2019).

1.5.2 Geologic Carbon as an Explanation for $\Delta^{14}C$ Anomalies?

When first discovered, the $\Delta^{14}C$ anomalies in the ETNP were taken to be the signature of carbon release from the deep ocean to the atmosphere (Marchitto et al., 2007). This earlier view of the $\Delta^{14}C$ anomalies buttresses the longstanding notion that stagnation of deep ocean circulation during the LGM created an isolated ^{14}C-deplete reservoir for the sequestration of atmospheric CO_2 (W. Broecker & Barker, 2007; Skinner et al., 2010)—and this view remains prevalent (e.g., Bova et al. (2018)). However, deep ocean

carbon storage and its effect on atmospheric CO_2 is more closely tied to the degree of nutrient consumption in the polar ocean regions that form new deep water (Hain et al., 2010, 2014; Ito & Follows, 2005; Marinov, Follows, et al., 2008; Marinov, Gnanadesikan, et al., 2008; Sigman & Haug, 2003; Sigman et al., 2010, 2021) rather than being a simple function of the rate of deep ocean overturning. Further, a new compilation of global ocean Δ^{14}C records reveals that the LGM ^{14}C age of the global deep ocean was about ∼1,000 years greater than today (Rafter et al., 2022), sufficient to explain a large portion of the observed Δ^{14}Cobs decline during the deglacial period (W. Broecker & Barker, 2007; Hain et al., 2014), but not nearly ^{14}C-deplete enough to produce the ETNP Δ^{14}C anomalies (Figure 1.3a). Rather than becoming a plank in our evolving understanding of coupled glacial/interglacial changes in ocean circulation and the global carbon cycle, the existence of these Δ^{14}C anomalies has become its own vexing problem, defying conventional explanations based on ocean circulation.

There are numerous reasons why a given sample would yield an anomalously low reconstructed ^{14}C/^{13}C, but the spatial-temporal clustering of ^{14}C anomalies in the upper 1 km of the ETNP water column is remarkable (e.g., Bova et al. (2018), Lindsay et al. (2015), Marchitto et al. (2007), Rafter et al. (2018, 2019), L. Stott et al. (2019), and L. D. Stott et al. (2019)), especially when contrasted with nearby records that broadly track atmospheric ^{14}C change without discernible ^{14}C anomalies (e.g., Bova et al. (2018), De Pol-Holz et al. (2010), Rose et al. (2010), Siani et al. (2013), and Zhao et al. (2018)). Previous modeling of the problem suggests that any ^{14}C anomaly in the upper ocean would rapidly dissipate by ocean circulation and air-sea gas exchange (Hain et al., 2011) such that upper ocean Δ^{14}C is expected to track atmospheric Δ^{14}C change since the LGM (Hain et al., 2014), as is observed in independently dated coral ^{14}C records from the Atlantic and Pacific (e.g., Chen et al. (2020)) and other records outside the anomalous ETNP cluster. Our new results advance the argument by demonstrating that even the release of >2,000 Pg C is insufficient to generate a significant ^{14}C anomaly on the basin scale resolved in our current model (Figure 1.3a), related to the rapid global dissipation of ^{14}C isotope anomalies in the global carbon cycle (Hain et al., 2011). That is, the absence of anomalies in most upper ocean ^{14}C reconstructions is normal and expected, even in the case of substantial simulated carbon release. The caveat to the argument is that a a small Δ^{14}C reduction simulated at the basin scale would be consistent with a

severe ^{14}C anomaly concentrated in a small sub-region, such as observed in the ETNP.

The ^{14}C anomalies of the ETNP may record carbon release associated with processes linked to spreading centers separating the Cocos, Nazca, and Pacific plates that produce very high regional geothermal heat flux (>0.1 W m^{-2} throughout the region; Pollack et al. (1993)). While we cannot usefully comment on whether these geologic systems are dynamic enough to yield defined pulses of carbon release, our results highlight that only a neutralized form of carbon release would be consistent with the atmospheric CO_2 constraint and observations of good (sometimes improved) seafloor carbonate preservation (Figure 1.3b; Yu et al. (2008, 2010, 2013)) during the main purported geologic carbon pulses. Indeed, the temporal coincidence of the ^{14}C anomalies with stadial/interstadial climate change, deglacial ocean heat uptake (Poggemann et al., 2018), and circulation change (e.g., McManus et al. (2004) and Rafter et al. (2022) may point to a climatic or environmental trigger of carbon release, rather than a being a purely stochastic volcanogenic phenomenon.

However, why would severe ^{14}C anomalies persist for millennia in the ETNP upper ocean water column if ocean circulation and air-sea gas exchange act to rapidly dissipate the anomalous carbon globally (Hain et al., 2011)? We propose two alternative resolutions that we cannot distinguish based on our current model and existing data: Either the anomalies are localized and reflect geologic carbon diffusion out of the underlying sediment stack rather than bottom water $\Delta^{14}C$, or the anomalies are regional and reflect the accumulation of geologic carbon in the ETNP shadow zone of ocean circulation with a sharp and persistent chemical gradient to the open ocean mid-depth Pacific.

If the anomalies are localized, we might expect each anomalous record to differ in magnitude and timing. Finding individual mid-depth sites in the ETNP where ^{14}C anomalies are missing (e.g., Bova et al. (2018) and Chen et al. (2020)) alongside records with ^{14}C anomalies that are only broadly similar would tend to support the localized explanation. Conversely, if geologic carbon were added to a dynamically isolated region, such as the upper ocean ETNP (Margolskee et al., 2019), seawater $\Delta^{14}C$ might diverge substantially from the $\Delta^{14}C$ of the open Pacific and atmosphere. However, that regional signal would need to be shared by all radiocarbon records in the hydrody- namic region (cf. Chen et al. (2020)). If the anomalies did reflect the restricted regional ocean circulation of

the ETNP, it would seem plausible that the carbon release mechanism also operated in regions outside the ETNP (e.g., Bryan et al. (2010)).

1.6 Conclusion

We document a set of carbon cycle model scenarios since the LGM that include substantial (800–2,400 Pg C) release of geologic carbon broadly consistent with reconstructed atmospheric CO_2 rise, $\Delta^{14}C$ decline, and $CaCO_3$ burial patterns. In all simulations, geologic carbon release is primarily released as HCO_3^- ion (i.e., with an ALK-to-DIC near 1), with minimal effect on the marine carbon cycle and atmospheric CO_2. That is, we demonstrate the possibility of climate-neutral geologic carbon and alkalinity release during the deglacial period in a way that is consistent with a dominant Southern Ocean control on climate-carbon coupling over ice age cycles. As such, we do not prove that such geologic carbon release happened, but rather we hope to expand what is deemed possible. The central outcome of this study is that the deglacial $\Delta^{14}C$ anomalies from the ETNP region may represent a natural analog for the successful application of OAE as a means to neutralize anthropogenic carbon emissions.

Introducing geologic carbon will dilute the planetary inventory of cosmogenic radiocarbon (^{14}C) such that the largest release of ^{14}C-free carbon (2,400 Pg C) can reduce the average $\Delta^{14}C$ of environmental carbon by about $\sim$50‰. Therefore, the planetary ^{14}C budget can be used to rule out the most extreme scenarios for geologic carbon release, offering an upper-bound constraint for carbon transfers from geologic and terrestrial carbon reservoirs to the ocean/atmosphere carbon cycle. That is, our model scenarios are designed to explore the limit of what appears to be possible in the context of global constraints from CO_2 and ^{14}C reconstructions. We find that HCO_3^- release was likely limited to less than 1,000 Pg C, but when considering uncertainty in the history of cosmogenic ^{14}C production, the limit for HCO_3^- release may be as high as 2,400 Pg C.

The spatial cluster of deglacial $\Delta^{14}C$ anomalies in the upper water column of the ETNP may be evidence for geologic carbon release associated with the seafloor spreading center defining the East Pacific Rise (Figure 1.1; Lindsay et al. (2015), Marchitto et al. (2007), Rafter et al. (2018, 2019), and L. Stott et al. (2009)). Confirming or rejecting this hypothesis would have several implications: Without large-scale carbon release, we lack

an adequate explanation for the ETNP $\Delta^{14}C$ anomalies, suggesting an open gap in our understanding of the ^{14}C-proxy system used to reconstruct ocean circulation changes in response to deglacial climate change. Alternatively, with large pulses of geologic carbon release in the ETNP, we lack an adequate explanation for how HCO_3^- is derived from geologic carbon sources during the deglaciation, suggesting a gap in our understanding of glacial/interglacial changes in seafloor spreading and its role in the global carbon cycle.

1.7 Acknowledgements

This research was funded by the National Science Foundation (Collaborative Research Grants OCE-2032340 to MPH and OCE-2032340 to PAR).

Chapter 2

Simulating deglacial radiocarbon anomalies with pH-neutral geologic carbon

This chapter will be submitted to *Paleoceanography and Paleoclimatology*: Green, R. A., Rafter, P. A., Sun, C., Gray, W. R., Rae, J. W. B., Pelly, M., Xu, C., Thirumalai, K. , Southon, J. R., Pavia F., and Hain, M. H. Simulating deglacial radiocarbon anomalies with pH-neutral geologic carbon.

2.1 Abstract

There currently is no explanation or carbon cycle model scenario for severe radiocarbon (^{14}C) depletion reconstructed in the intermediate depth eastern tropical North Pacific Ocean (ETNP) at the end of the last ice age. Here we develop new constraints on hypothesized geologic carbon release based on the boron isotope pH proxy and regional refinement of a global carbon cycle model, and we find that pH-neutral release of ∼800 Pg C over 5000 years can produce the radiocarbon anomalies in the ETNP while causing no $CaCO_3$ dissolution (as observed) and minimal CO_2 rise. Mass-balance considerations dictate that the anomalous carbon was concentrated near the source in the ETNP without affecting radiocarbon-based reconstructions of global ocean circulation change.

2.2 Main

The global distribution of the radioactive carbon isotope ^{14}C (radiocarbon) is a crucial tool for measuring the rate of carbon exchange between the atmosphere and the ocean (Bolin, 1960; Craig, 1957; Revelle & Suess, 1957). Radiocarbon is also a powerful constraint on the hypothesis that deep ocean circulation changes were responsible for the abrupt rise in atmospheric carbon dioxide (CO_2) concentration at the end of the last ice age (W. Broecker et al., 2004; Skinner & Bard, 2022). In what seemed to be a break-through moment (W. Broecker, 2009), Marchitto et al. (2007) found severe ^{14}C depletions (decay-corrected ^{14}C:^{12}C ratio, expressed as $\Delta^{14}C$ Stuiver and Polach, 1977) in intermediate-depth waters off Baja California in the Eastern Tropical North Pacific (ETNP). Broecker and Barker (2007) subsequently proposed that abyssal ocean overturning circulation must have stalled during peak ice age conditions. Subsequently, ocean overturning accelerated during termination, contributing the observed ^{14}C-depleted carbon to the mid-depth ocean and atmosphere. Further radiocarbon reconstructions and data compilations have since provided strong evidence that deep ocean circulation was reduced during the last glacial maximum (LGM) and accelerated during deglaciation, suggesting a role in ocean CO_2 release to the atmosphere (Rafter et al., 2022; Skinner et al., 2010).

However, the ocean ^{14}C depletions discovered by Marchitto et al (2007) were found to be too severe and too prolonged to be explained by changes in global ocean overturning (Hain et al., 2011). While radiocarbon anomalies have been reported across the Eastern Pacific (Bova et al., 2018; Lindsay et al., 2015; L. Stott et al., 2009; L. D. Stott et al., 2019), there is a particular spatial cluster of anomalies in the ETNP (Lindsay et al., 2016; Marchitto et al., 2007; Rafter et al., 2018, 2019) (Figure 1), existing alongside nearby records that show no such anomalies (Bova et al., 2018; Chen et al., 2020). This raises a significant problem for the paleoceanographic research community: if ocean circulation did not cause the radiocarbon anomalies, how can we trust radiocarbon reconstructions of ocean circulation?

One proposed solution would be to disregard the anomalous radiocarbon samples based on unspecified diagenetic overprint, which would erase the primary seawater radiocarbon signature in these specific ocean sediment samples. However, the sampled benthic and

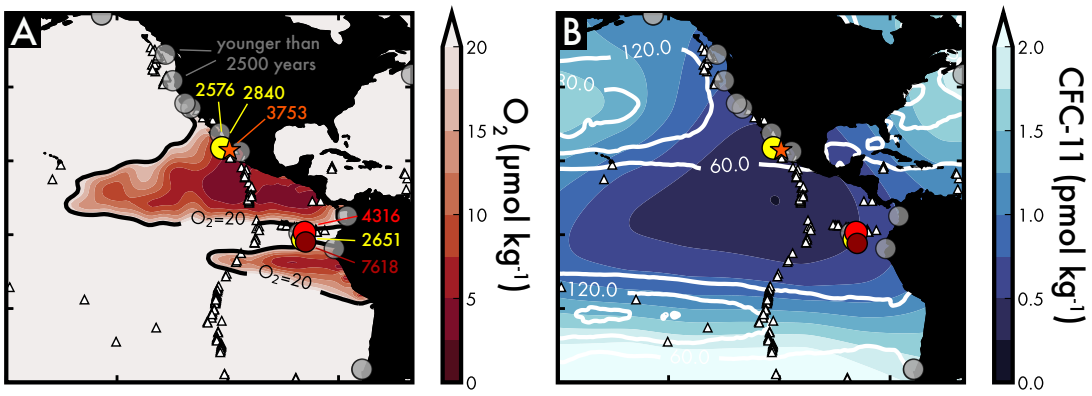

Figure 2.1: Intermediate depth ($< 1000\,\mathrm{m}$) $\Delta^{14}C$ anomalies (colored points; Lindsay et al., 2016; Marchitto et al., 2007; Rafter et al., 2018, 2019; L. Stott et al., 2009) in the context of modern Eastern Pacific hydrographic conditions. Anomalies are defined as having mean deglacial (18 kyr BP–12 kyr BP) ventilation ages greater than 2500 years, based on data from the Rafter et al. (2022) ^{14}C compilation. Each anomaly's age is shown in the plot, with non-anomalous ^{14}C data displayed in gray. The star marks the site of new data presented in this study. (A) Dissolved oxygen (µmol kg^{-1}) at 500 meters depth (Lauvset et al., 2024). (B) Concentrations of chlorofluorocarbons (CFC-11 in pmol kg^{-1}) with white contours representing potential vorticity (10^{-12} m^{-1} s^{-1}) at 500 meters depth (Lauvset et al., 2024). White and black triangles indicate the locations of hydrothermal vents.

planktonic foraminifera in the ETNP pass a wide range of preservation tests, replication on multiple benthic foraminifera species, and built on a high-quality sedimentary age model (based on ^{14}C-dated terrestrial wood fragments Rafter et al., 2018; Figure 2D). One specific concern is the possibility of overgrowth of authigenic carbonate onto foraminiferal tests, associated with sediment porewater sulfate reduction horizons. This authigenic carbonate addition is suspected of altering foraminifera ^{14}C ages in NW Pacific sediments (Cook et al., 2011). However, while these sulfate reduction horizons are associated with depth below the seafloor, the ETNP Δ^{14}C anomalies occur at the same stratigraphic age in cores with vastly different sedimentation rates and therefore at vastly different core depths (Marchitto et al., 2007; Rafter et al., 2018). This coincidence could be explained if there was active sulfate reduction in surface mixed layer sediments during the anomalous time periods. Indeed, the intensity of the eastern tropical Pacific oxygen-deficient denitrification zones seems to have transiently intensified during the deglacial period (Studer et al., 2021), possibly pointing to regional deoxygenation in subsurface waters of the ETNP during the time of the recorded radiocarbon anomalies. However, a dilution of foraminiferal calcite greater than 20%, which is needed to produce a 200‰ radiocarbon anomaly, would be visible upon inspection of the picked foraminifera samples and would surely fail the stable isotope preservation tests (Cook & Keigwin, 2015; Rafter et al., 2018). As such, we lack any sound basis to discount the ETNP radiocarbon anomalies, casting an uncomfortable light also on the interpretation of other spatially isolated occurrences of deglacial radiocarbon anomalies, such as those offshore (Bryan et al., 2010) and the Galapagos (L. Stott et al., 2009) (but see also Chen et al. (2020)).

To address these concerns, we investigate an alternative explanation for the deglacial radiocarbon anomalies, the idea that there was a release of ^{14}C-free carbon from geologic sources on the ETNP seafloor, possibly related to climate-paced variability in seafloor spreading and volcanism (Huybers & Langmuir, 2009; Lund et al., 2016; Lund & Asimow, 2011; Lund et al., 2019). In this scenario the anomalous foraminiferal samples grew in seawater with admixed geologic carbon. Some proponents of this hypothesis suggest the geologic carbon was released in the form of carbon dioxide (CO_2), contributing to the deglacial rise of atmospheric CO_2 (Ronge et al., 2016; L. Stott & Timmermann, 2011; L. Stott et al., 2009; L. D. Stott et al., 2019). However, ocean acidification from

the significant CO_2 release would have quantitatively titrated sea water carbonate ion (CO_3^{2-}) and corroded/dissolved the anomalous foraminifera sample material. More recently, Rafter et al. (2019) proposed that the geologic carbon was instead neutralized by an equimolar amount of alkalinity, converting the additional CO_2 into bicarbonate (HCO_3^-) and thereby mitigating localized seawater acidification. Further, inverse carbon cycle modeling based on reconstructed atmospheric CO_2 and $\Delta^{14}C$ records suggests that geologic carbon release unlikely exceeded ∼800 Pg C and, if so, must have been accompanied by a comparable input of alkalinity (Green et al., 2024), however that scenario fails to produce basin-scale $\Delta^{14}C$ anomalies. In this study, we directly assimilate the anomalous ETNP $\Delta^{14}C$ data to infer required carbon release when focused into a refined model representation of the Gulf of California region and we present new $\delta^{11}B$ data as a proxy for seawater pH to constrain concomitant alkalinity inputs.

2.3 Simulating the ETNP $\Delta^{14}C$ anomalies

The ETNP $\Delta^{14}C$ anomalies (Lindsay et al., 2016; Marchitto et al., 2007; Rafter et al., 2018, 2019) (Fig 1A) are situated in a 'shadow zone' of the geostrophic flow of the North Pacific gyre, where potential vorticity barriers limit exchange between the ETNP and the open Pacific. This hydrographic isolation of the ETNP leads to the observed low oxygen concentrations and minimal intrusion of anthropogenic CFC-11 (Fig. 1B). To represent the relative isolation of the ETNP target region we couple a regional box model into the global model framework, integrating advection and mixing processes across both regional and global scales. Our regional model comprises three interconnected boxes: the 'Marchitto box' (representing the intermediate depth shadow zone), the 'GoC subsurface', and the 'GoC surface', each optimized with equimolar carbon and alkalinity release to meet the three respective observational data sets (See more details in "Methods" section; Extended Data Fig. 1). The ocean and air/sea boundary fluxes of the regional model are then applied to the global model to update the boundary condition of the regional model, a sequence that is repeated until the boundary condition and carbon release converge on the internally consistent solution. This setup enables us to evaluate the distinct effects of regional isolation and global dissipation on the $\Delta^{14}C$ signature of water as it moves through the ETNP and the global ocean.

The size and mixing of the GoC boxes are geographically constrained by the Baja California peninsula, but we systematically tested different sizes and varying degrees of isolation of the larger 'Marchitto box' that is an intermediary for water flowing from the global model boundary into the GoC (Extended Data Fig. 1). In our discussion we focus on two contrasting end members: (1) a "fast flushing" scenario with a small box volume (∼5 times the GoC volume) and high exchange rates (∼ 5 Sv, $1\,\mathrm{Sv} = 10^6\,\mathrm{m^3\,s^{-1}}$) that yield a short residence time of water in the region (red markers and lines in Figs. 2 and 3), and (2) a "slow flushing" scenario with low mixing rates (0.5 Sv) and a larger box volume (∼10 times the GoC volume) that yield longer residence time (yellow markers and lines in Figs. 2 and 3). Under the slow flushing conditions significantly less carbon (393 Pg C) is required than under fast flushing (1845 Pg C) to produce the observed Δ^{14}C anomalies within the Marchitto box (Fig. 2C). However, both scenarios required a consistent amount of carbon (∼600 Pg C) to match the observed anomalies in the downstream GoC boxes (Fig. 2A and B). These end-member scenario carbon totals broadly align with the conservative (∼800 Pg C) and speculative (∼2400 Pg C) upper bound estimates from the global radiocarbon budget (Green et al., 2024) (Fig 3A).

The large difference in total carbon release between our two end-member scenarios offers a useful contrast when comparing our model results to reconstructed atmospheric Δ^{14}C, CO_2, and regional pH data. The fast flushing experiment with 2482 Pg carbon release slightly undershoots reconstructed atmospheric Δ^{14}C consistent with a possible bias in the simulated ^{14}C production history before the LGM (Green et al., 2024), and it overshoots reconstructed CO_2 related to the fixed equimolar carbon and alkalinity release flux that we invert to match the ETNP Δ^{14}C anomalies. While the low flushing scenario yields a better fit with atmospheric Δ^{14}C and CO_2, both scenarios are broadly consistent with these data considering uncertainty in the Δ^{14}C budget and the carbon-to-alkalinity assumed in our simulations. The fundamental reason why vastly different carbon release scenarios can yield similar CO_2 histories is that equimolar carbon and alkalinity release have minimal effect on seawater pH, as confirmed by our new pH reconstruction for the GoC site (Fig. 2F, 3B), derived from new δ^{11}B benthic foraminifera measurements.

If the carbon were instead released as pure CO_2 without accompanying alkalinity, it would lead to substantial local and regional acidification as well as elevated atmospheric CO_2 levels. In our conservative, slow flushing scenario, CO_2 addition results in a sus-

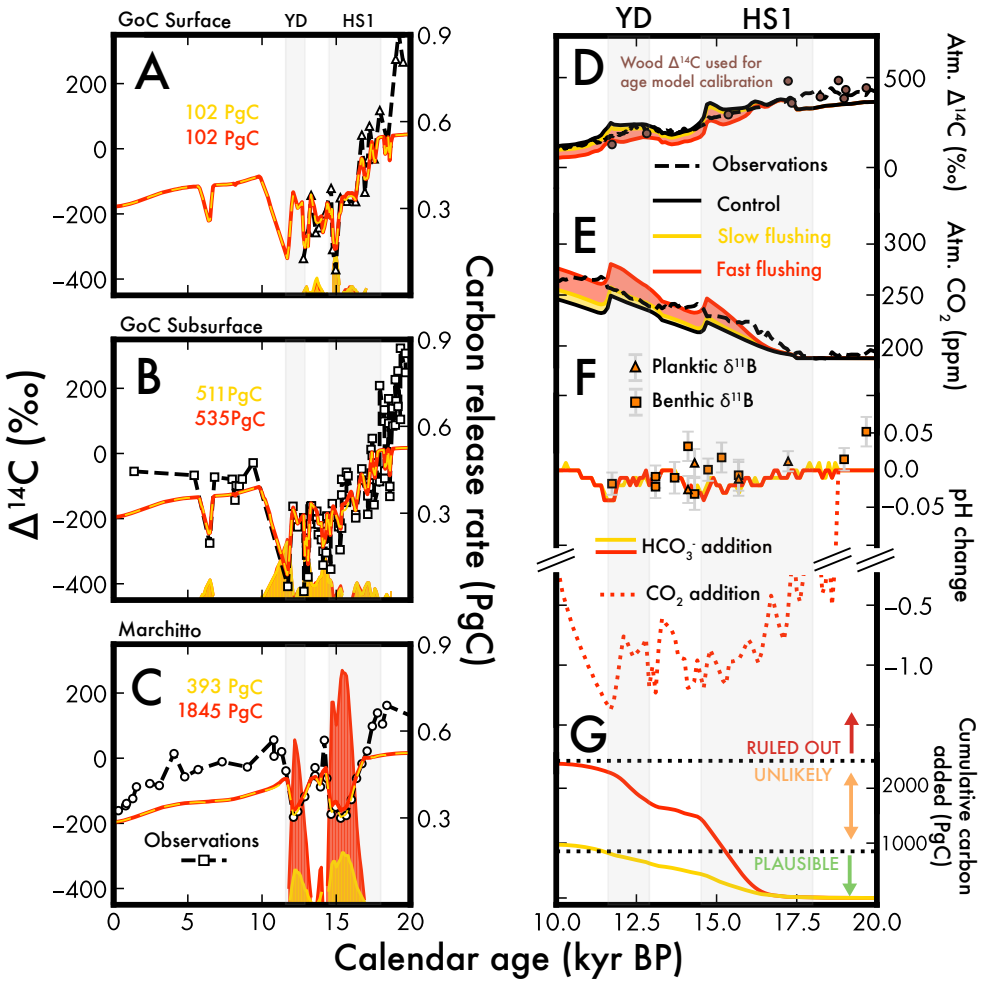

Figure 2.2: Comparison of simulated and observed Δ^{14}C anomalies, atmospheric data, pH effects, and modeled geologic carbon release rates for both slow and fast flushing experiments. Panels A–C display the simulated Δ^{14}C anomalies and release rates for the Marchitto box (Panel C), the GoC subsurface (Panel B), and the surface (Panel A), with observational Δ^{14}C data shown as markers: circles for the Marchitto box (Marchitto et al., 2007), squares for GoC subsurface (benthic) (Rafter et al., 2018), and triangles for GoC surface (planktic) (Rafter et al., 2018). Simulated Δ^{14}C results are shown as lines, with shaded areas representing release rates. Yellow and red correspond to the slow and fast flushing experiments, respectively. Panels D and E display atmospheric Δ^{14}C (Reimer et al., 2020) and CO_2 (Bereiter et al., 2015), respectively, alongside simulated results. Wood Δ^{14}C data is shown with brown circles, which were used for calibrating the age model in Rafter et al. (Rafter et al., 2018, 2019) and for the new data presented in this study. Panel F shows the pH change (calculated using Eqn. 12 from Hain et al. (2018)) based on δ^{11}B data from GoC benthic and planktic foraminifera against the simulated pH change. Panel G displays cumulative carbon addition, with dashed black lines showing constraints based on the global radiocarbon budget (Green et al., 2024).

tained pH drop of more than 1 unit over the entire deglacial period, far exceeding the minor pH change (∼0.05) observed in δ^{11}B-derived ΔpH (Fig. 2F, Extended Data Fig. 2B). Additionally, this CO_2 addition would cause atmospheric CO_2 levels to greatly overshoot reconstructed values, reaching approximately 300 ppm by ∼12-kyr BP (Extended Data Fig. 2A).

This is also shown in Fig. 3B, as generating the observed Δ^{14}C anomalies without deviation from the observed ΔpH requires the geologic carbon source to have an alkalinity-to-dissolved inorganic carbon (ALK:DIC) ratio between 1:1 and 1.2:1. In contrast, pure CO_2 addition (ALK:DIC of 0:1) immediately drives unobserved acidification before producing any notable Δ^{14}C anomaly.

2.4 Role of Hydrodynamic Isolation

It is quite intuitive that geologic carbon release can drive localized Δ^{14}C anomalies, but previous attempts to simulate such anomalies in the equatorial and south Pacific (Ronge et al., 2016; L. Stott et al., 2019) failed even though the simulated rate of carbon release was similar to our high flushing scenario. To understand this discrepancy in model results we need to consider the carbon isotope mass balance of a region affected by a persistent Δ^{14}C anomaly: First, a larger volume (V) of affected water requires more ^{14}C-free geologic carbon input (ΔC) to attain a given Δ^{14}C anomaly (A) against the background seawater DIC. And, more importantly, to maintain a given anomaly ($\partial A/\partial t = 0$) against the tendency of the affected volume to be flushed by mixing (M) with the global ocean requires a persistent flux (F) of geologic carbon release that is reciprocal to the flushing timescale ($\tau = V/M$) of the affected volume, but not the volume itself.

$$\Delta C \approx \frac{-A}{A+1} \cdot V \cdot \mathrm{DIC}, \tag{2.1}$$

$$\frac{\partial A}{\partial t} = 0 = F - \frac{\Delta C}{V} \cdot M = F - \frac{\Delta C}{\tau}, \tag{2.2}$$

$$\int F\, dt = \frac{\Delta C \cdot \Delta t}{\tau}. \tag{2.3}$$

The key insight from this consideration is that a relatively large affected region would

require a relatively large amount of initial carbon release (ΔC) to develop observed anomalies (i.e., A of -0.2 $\approx$ -200‰), but over time it is the flushing timescale of the affected volume that determines the cumulative carbon release required to maintain the anomalies as observed. For example, generating a $\sim$200‰ anomaly across a 100m depth interval of the North Pacific thermocline ($V \sim 8 \times 10^{15}\ m^3$) or the GoC ($V \sim 1.45 \times 10^{14}\ m^3$) requires an initial carbon input of 48 Pg C and 0.84 Pg C, respectively. And, to maintain anomalies at this level for 1000 years against 1 Sv of exchange flux requires 189 Pg C cumulative release in both cases, because the larger volume is flushed slower (254 years) than the smaller (4.6 years)

To explore these fundamental constraints linking the magnitude of the observed anomalies, the spatial extent of the affected region and its relative isolation from the rest of the ocean we systematically change the size (V) and different mixing rates (M) of the 'Marchitto box' in our regional model (Fig. 3A). We find that regions at the scale of the GoC can support the observed ETNP Δ^{14}C anomalies with plausible cumulative carbon release even if the region is flushed with a timescale of less than 5 years (lower left corner in Fig. 3A), while any sustained anomaly in a larger region would require significant hydrodynamic isolation (decades long residence/flushing time, τ) with respect to the basin scale circulation of the open Pacific (lower right corner in Fig. 3A). As such, we demonstrate that the spatial cluster of Δ^{14}C anomalies in the ETNP can be reproduced within global ^{14}C budget constraints (Green et al., 2024).

Estimates based on zonal oxygen supply to the eastern tropical Pacific oxygen deficient zones (ODZs north and south of the equator) suggest a mean flushing time of 17 years for the larger region (Sonnerup et al., 2019), and CFC-derived ventilation ages for the ETNP are $>$ 30 years on the 26.8 isopycnal (Fine et al., 2001). Indeed, as of 1999 there was a sharp CFC front on the 26.8 isopycnal adjacent to Baja California, with concentrations dropping from 0.50.5 $\mathrm{pmol\,kg^{-1}}$ at 28°N to 0.1 $\mathrm{pmol\,kg^{-1}}$ at 24°N (van Geen et al., 2006), firmly placing the Marchitto site and the GoC into the most isolated corner of the ETNP shadow zone. More conspicuously, these authors argue that the reconstructed expansion of the ETNP ODZ during the deglacial period (Ganeshram & Pedersen, 1998; Gardner et al., 1997; Keigwin & Jones, 1990; Studer et al., 2021) is consistent with a large reduction in the flow that delivers oxygen and CFC from the subpolar North Pacific to Baja California. It is this hydrodynamic isolation of the GoC

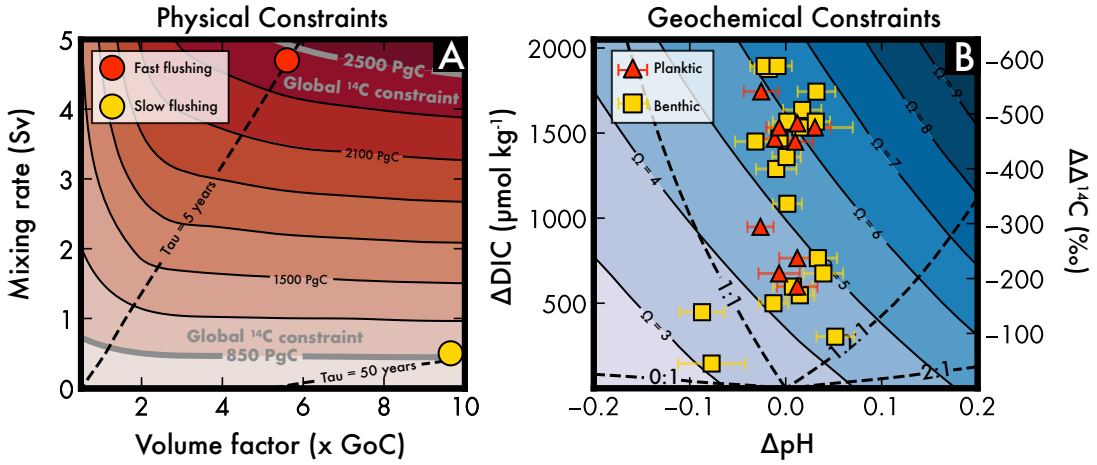

Figure 2.3: Physical and geochemical constraints on geologic carbon addition. (A) Physical constraints showing simulated carbon release across a range of mixing rates (y-axis) and Marchitto box sizes (x-axis, in multiples of GoC volume). Contours represent the total carbon required to simulate $\Delta^{14}C$ anomalies, with gray lines indicating global radiocarbon budget limits (Green et al., 2024). Yellow and red circles denote slow and fast flushing end-member experiments, respectively, with black dashed lines showing their respective residence times of the Marchitto box. (B) Geochemical constraints based on PyCO2SYS (Humphreys et al., 2021) solver results and observations. We apply a scaling relationship between ^{14}C-free carbon addition and resulting $\Delta^{14}C$ anomalies from the CYCLOPS carbon cycle model ($\Delta\Delta^{14}C = -0.31 \times \Delta DIC$) to align PyCO2SYS-derived aragonite saturation state (Ω) contours with calculated ΔpH and $\Delta\Delta^{14}C$ from observed GoC data (yellow squares for benthic and red triangles for planktic). Ω contours are calculated from a range of DIC and pH values, assuming a baseline DIC concentration of 2150 $\mu mol\,kg^{-1}$ and a pH of 8.07. Dashed black lines indicate ALK:DIC ratios for different hypothetical geologic carbon sources.

region that predisposes it to develop relatively large $\Delta^{14}C$ anomalies. Any deglacial reduction in GoC flushing time would proportionally decrease the cumulative carbon release needed to meet the observed $\Delta^{14}C$ anomalies. This is in contrast to other Pacific sites where $\Delta^{14}C$ anomalies have been reported in regions that lack significant isolation from the basin-wide circulation (Ronge et al., 2016; L. Stott et al., 2009).

2.5 Carbon Cycle Implications

We find no discernible change in reconstructed seawater pH associated with severe $\Delta^{14}C$ anomalies in benthic and planktic foraminifera from the GoC (Fig. 3B), consistent with the recent discovery of carbon-rich, pH-neutral, and $CaCO_3$-forming hydrothermal vents in the southern GoC (Paduan et al., 2018). The expected regional pH anomaly (ΔpH) and effect on seafloor $CaCO_3$ saturation ($\Delta \ln \Omega$) depends both on the ambient seawater carbonate ion concentration ($[{CO_3}^{2-}]$ of 50–80 μmol kg^{-1}) and the difference in carbon and alkalinity release flux ($F_{CO_2} - F_{ALK}$) divided by the flushing timescale τ:

$$2.3 \cdot \Delta\text{pH} \approx \Delta \ln \Omega = \frac{\text{CPF}}{[{CO_3}^{2-}]} \cdot \frac{(F_{CO_2} - F_{ALK})}{\tau}, \tag{2.4}$$

where CPF stands for the "carbonate proton fraction" (see Hain et al. (2015)) and equates to the fraction of total seawater buffering that is due to the bicarbonate/carbonate ion buffer. Thus, the absence of a pH anomaly or signs of corrosion in our foraminifera samples suggests that CO_2 and alkalinity fluxes were approximately equimolar ($F_{CO_2} \approx F_{ALK}$), supporting the hypothesized 'neutralized carbon' release as the most probable explanation for ETNP $\Delta^{14}C$ anomalies (Green et al., 2024; Rafter et al., 2019).

Once dissipated globally, equimolar release of carbon and alkalinity would have muted effects on global deep ocean Ω and cause relatively small atmospheric CO_2 change ($\Delta \ln CO_2$) after accounting for $CaCO_3$ compensation:

$$\Delta \ln CO_2 \approx \frac{0.06\%}{\text{Pmol}} \cdot \left(2 \cdot \int F_{CO_2}\, dt - \int F_{ALK}\, dt\right), \tag{2.5}$$

where the scaling factors account for seawater buffering and equilibration with a finite atmosphere (see Supplement Text Hain et al., 2015). For example, the cumulative release

of 800 Pg geologic carbon in the form of 67 Pmol CO_2 would cause severe ocean acidification and 67 Pmol net $CaCO_3$ dissolution, yielding about an 8% CO_2 rise. Compare this with a concomitant equimolar CO_2 and alkalinity release, which would be pH-neutral, cause no $CaCO_3$ dissolution, and raise CO_2 by 4%, consistent with the +12 ppm CO_2 rise in our slow flushing scenario (Fig. 2E).

Hence, geologic release of neutralized carbon may explain the pH-neutral ETNP $\Delta^{14}C$ anomalies, but even when taken to the likely limit of the global ^{14}C budget constraint (Green et al., 2024), it would yield only a minor contribution to the +47% observed deglacial CO_2 rise. In this scenario, $\Delta^{14}C$ anomalies are highly concentrated in the ETNP shadow zone, without significant impact on the use of radiocarbon dating to reconstruct ocean circulation in the rest of the global ocean.

2.6 Methods

2.6.1 ETNP Regional Model

To simulate geologic carbon addition in the Eastern Tropical North Pacific (ETNP), we developed a regional three-box carbon cycle model specifically tailored to this region. The model comprises three connected boxes: (1) the intermediate-depth ETNP shadow zone, which interacts with the Gulf of California (GoC) via the Mexican Coastal Current (MCC; Gómez-Valdivia et al., 2015), (2) the northward-flowing subsurface GoC waters, and (3) the southward-flowing surface waters in the GoC. These are referred to as the "Marchitto box" (honoring Prof. Thomas Marchitto for his original discovery of the $\Delta^{14}C$ anomalies Marchitto et al., 2007), the "GoC subsurface box," and the "GoC surface box" (Extended Data Fig. 1).

The GoC subsurface and surface boxes are assigned depths of 600 m and 200 m, respectively, with the subsurface depth based on benthic radiocarbon records at 624 m (Rafter et al., 2018) and the surface depth based on Lavín and Marinone (2003). The northern boundary is defined at the Guaymas Basin, approximately 550 km north of the GoC core site (Rafter et al., 2019). The GoC box width is set to 150 km, following Nix (2013).

Given uncertainty in the spatial extent and relative isolation of the anomalous ^{14}C-

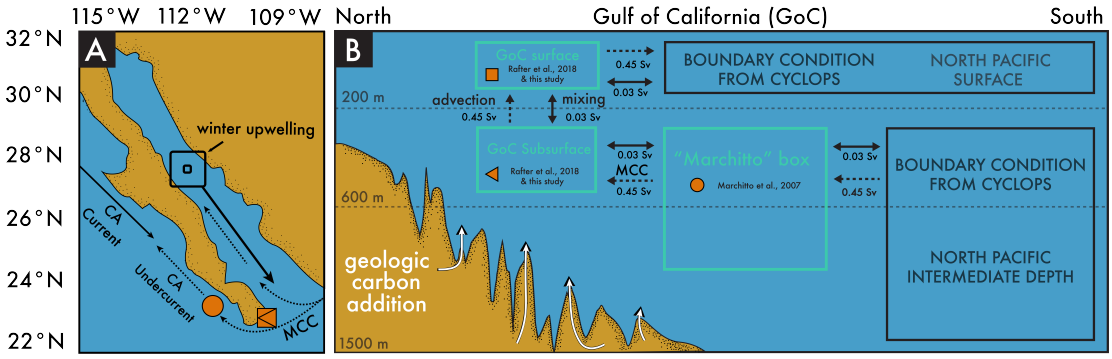

Figure 2.4: Regional model framework and observational data used to inform the model. Seafloor spreading along the East Pacific Rise and Gulf of California influence seawater characteristics both at depth and at the surface. Mean Gulf circulation is in at depth and out at the surface (dashed arrows; (Lavín & Marinone, 2003)). The regional model framework is shown by the teal boxes (Panel A). The model's boundary conditions, derived from the global carbon cycle model CYCLOPS, are represented by black boxes (Panel A). Markers indicate the location of the California Undercurrent (orange circle) and Gulf of California (orange sideways triangle and square) site LPAZ-21P (Panels A and B). In Panel A, the markers are shown in each regional box where that data is used to inform the regional model. There are two markers for the Gulf of California site LPAZ-21P because the core site includes planktic and benthic data. Note that the subsurface (200 to $\approx$ 700 m) Mexican Coastal Current (MCC) feeds into the deep Gulf and California Undercurrent (Gómez-Valdivia et al., 2015), bathing both the Gulf and Undercurrent core sites (Marchitto et al., 2007). Thus, the Undercurrent core site (orange circle) can be assumed representative of water "upstream" to the Gulf of California core site. Figure adapted from Rafter et al. (Rafter et al., 2019).

depleted water mass entering the GoC, we conduct experiments across a range of Marchitto box sizes (0 to 10 times the volume of the GoC) and mixing rates (0–5 Sv) between the Marchitto box and the intermediate North Pacific boundary (Fig. 3A). We highlight two end-member simulations:

1. *Fast flushing:* A smaller Marchitto box volume (5.6 times the GoC) with a high mixing rate (4.7 Sv).

2. *Slow flushing:* A larger Marchitto box volume (9.65 times the GoC) with a low mixing rate (0.5 Sv).

The regional model simulates a suite of tracers: phosphate (P), δ^{13}C, Δ^{14}C, dissolved inorganic carbon (DIC), alkalinity, and pH. Key processes include advection, mixing, air-sea gas exchange, biological productivity, geologic carbon addition, and alkalinity addition. Advection is set at 0.45 Sv (Rafter et al., 2019), correcting a typographical error in the original manuscript that reported 0.3 Sv. Mixing within the GoC is assigned a rate of 0.03 Sv, approximately 15 times smaller than the advection flux. Further details on model parameters are in Extended Data Fig. 1.

2.6.2 Coupling with CYCLOPS

To incorporate global carbon cycle dynamics, we coupled the regional model with the global carbon cycle model CYCLOPS (Green et al., 2024; Hain et al., 2011, 2014) through an iterative process. First, we initialize the regional model using outputs from a deglacial scenario in CYCLOPS (Hain et al., 2014), applying these as time-evolving boundary conditions.

At each time step, concentrations of P, δ^{13}C, Δ^{14}C, DIC, and ALK from CYCLOPS are incorporated into the regional model via advection and mixing. The regional model calculates the optimal rate of geologic carbon addition to replicate observed Δ^{14}C anomalies in the Marchitto, GoC subsurface, and GoC surface boxes (Marchitto et al., 2007; Rafter et al., 2018, 2019). Optimization is conducted using the `minimize` function in the SciPy library (Virtanen et al., 2020), identifying the rate of carbon addition that brings simulated Δ^{14}C values within a threshold of 0.1‰ of observed values.

The global CYCLOPS model is then rerun with geologic carbon added to the surface

North Pacific, where water exits the GoC. The regional model is rerun with updated boundary conditions, repeating the optimization until the total geologic carbon addition stabilizes within 1 Pg C over two consecutive simulations.

In most simulations presented in the main text, geologic carbon is added with an equimolar amount of alkalinity (ALK:DIC ratio of 1:1, simulating bicarbonate addition) and a δ^{13}C value of $\pm -2.5\,‰$ based on Green et al. (2024). To explore other potential sources of geologic carbon, we also simulate the slow flushing scenario with carbon added as pure CO_2 (ALK:DIC ratio of 0) and a δ^{13}C value of $\pm -8.9\,‰$, based on CO_2 from GoC hydrothermal vents (Paduan et al., 2018).

2.6.3 Δ^{14}C Data Used in the Regional Model

Our regional model framework is informed by Δ^{14}C data from benthic and planktic foraminifera collected at the mouth of the Gulf of California (GoC) and along the Pacific margin of Baja California. For the GoC, benthic and planktic foraminiferal data were gathered from a depth of 624 meters (Rafter et al., 2018). The deep Δ^{14}C record was built using benthic foraminifera *Planulina ariminensis* and *Uvigerina spp.*, both of which are good recorders of bottom water Δ^{14}C (Rafter et al., 2018). The surface water Δ^{14}C record was built by measuring planktic foraminifera record *Globigerina bulloides*. For years with multiple benthic records, we used the average Δ^{14}C value of both species to provide a representative estimate.

The GoC core site is influenced by the MCC, which transports poorly ventilated subsurface waters northward (Gómez-Valdivia et al., 2015). This current also supplies water to the California Undercurrent, overlying sediment core sites along the Pacific margin of Baja California, where the earliest deglacial Δ^{14}C anomalies were observed (Marchitto et al., 2007). Accordingly, we use the mixed benthic foraminiferal record from California Undercurrent waters (Marchitto et al., 2007) as a proxy for conditions in the MCC and the ETNP shadow zone (see Extended Data Fig. 1).

The GoC follows an estuarine circulation pattern, with deep inflowing seawater and surface outflow. Within this structure, benthic foraminiferal data represent the characteristics of poorly ventilated subsurface inflow from the MCC, while planktic foraminifera reflect the outflowing surface water conditions.

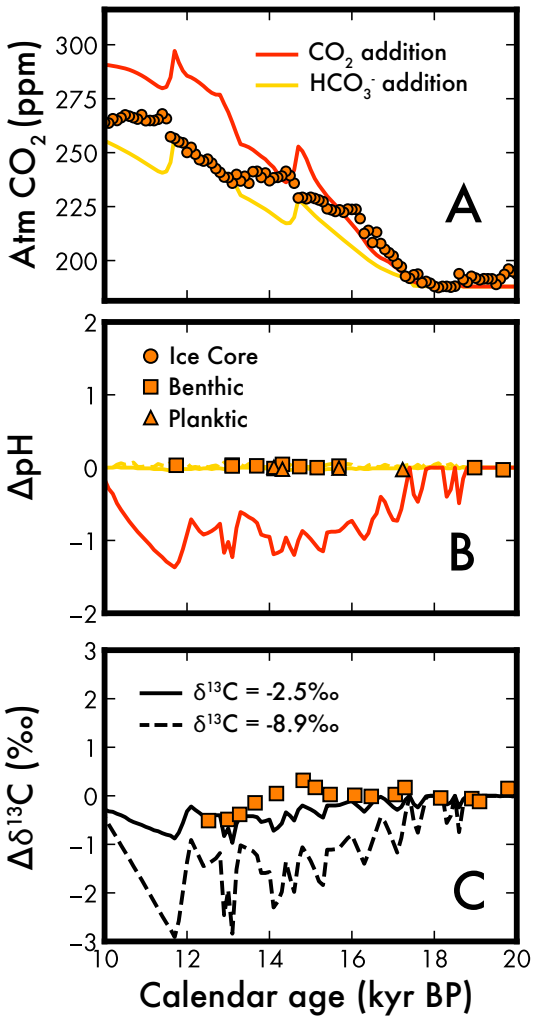

Figure 2.5: Comparison of simulated and observed changes in atmospheric CO_2, pH, and $\delta^{13}C$ in response to different sources of geologic carbon addition scenarios using our fast-flushing scenario. (A) Simulated atmospheric CO_2 for bicarbonate addition (ALK:DIC = 1) versus CO_2 addition (ALK:DIC = 0) compared to reconstructed observations (Bereiter et al., 2015). (B) Simulated pH changes for bicarbonate addition (ALK:DIC = 1) versus CO_2 addition (ALK:DIC = 0). Adding CO_2 results in a large ΔpH of approximately -1, which is inconsistent with observational data, while bicarbonate addition shows minimal pH change, aligning better with observations. (C) Simulated $\delta^{13}C$ changes based on two different $\delta^{13}C$ sources: $-2.5‰$ and $-8.9 \pm 0.2‰$. New high-resolution benthic $\delta^{13}C$ observations from the GoC are overlaid, showing minimal $\delta^{13}C$ change, suggesting that the $-2.5‰$ source aligns more closely with observed values.

In addition to $\Delta^{14}C$, we also measured $\delta^{13}C$ and $\delta^{11}B$ from the same sediment core as the GoC $\Delta^{14}C$ anomalies (Rafter et al., 2018, 2019), derived from the benthic foraminifera *P. ariminensis*. These additional isotopic records provide further insights into the past carbonate chemistry and water mass characteristics of the ETNP, supplementing the $\Delta^{14}C$ data used to inform the model.

2.6.4 $\delta^{11}B$ Analytical Methods and ΔpH Calculations

Between 4-8 benthic and >50 planktic foraminifera tests were picked from the >250 μm and >125 μm size fraction for trace element and $\delta^{11}B$ analyses. Sample preparations were carried out in a low-boron clean lab at the University of St Andrews. Samples were cleaned based on the "Mg-cleaning" oxidation procedure (Barker et al., 2003; Rae et al., 2011). An aliquot ($\sim$3% of the total sample) was taken for trace element analyses, which were performed on an Agilent 8900 ICP-MS at the University of St Andrews using matrix-matched standards. Long-term reproducibility of Mg/Ca and B/Ca using this method is 1.2% and 2.3% (2 SD), respectively. Prior to $\delta^{11}B$ analysis, samples were screened for potential contamination by checking various elemental ratios (B/Ca, Mg/Ca, and Al/Ca). All samples have Al/Ca ratios <100 μmol/mol.

Boron was separated from the sample matrix using Amberlite IRA-743 boron specific anion exchange resin. For one set of samples, the protocol followed the 'column' method of Foster (2008) and Foster et al. (2013). For a subsequent set of samples, the 'batch' protocol of Trudgill et al. (2024) was used, which improves the precision of $\delta^{11}B$ analysis at low concentrations typical of foraminiferal samples. Analysis of the same standard by both techniques shows no significant offset between the techniques (Trudgill et al. (2024) and below).

$\delta^{11}B$ was measured on a Thermo Scientific Neptune plus MC-ICP-MS at the University of St Andrews, based on protocols described in Foster (2008), Rae et al. (2011), Rae (2018), but with the addition of high ohmage (1013 Ω) resistors and triplicate sample analyses (Trudgill et al., 2024; Xu et al., 2024). Samples were corrected for total procedural blank, which averaged 80 pg for the samples for through columns, and $\sim$9 pg for the samples analyzed by batch. Rae et al. (2011) previously reported uncertainties of $\pm$0.23‰ (2 SD) for samples of $\sim$20 ng, increasing at smaller sample sizes. This

has been improved given the developments in analyses described above (Trudgill et al., 2024). For example a boric acid standard (ERM-AE12161) run during these sessions at a similar concentration and under the same conditions as these samples (15-25 ppb) gave δ^{11}B = 19.64 ±0.06‰ (2 SD, n = 8). However as full description and quantification of this updated method is beyond the scope of the current study, we assign conservative analytical uncertainties following the relationships in Rae et al. (2011) for the samples analysed through columns. For the samples analysed by batch (which improves the precision of small samples relative to columns), we assign the external standard deviation of repeated analysis of NIST 8301 Foram (spanning the sample size range of the foraminiferal samples) by this method during the analytical session (±0.11 ‰ 2 SD, n=5), which agrees with the long-term reproducibility of the method within the lab as reported by Trudgill et al. (2024) in size range spanning the samples. Replicate purifications and measurements of NIST 8301 Foram (a dissolved carbonate standard with a composition mimicking planktic foraminifera), analysed during the same analytical sessions as the samples, gave a value and ±2 SD of 14.72±0.23 ‰ (n = 2) using the columns method at 25 ppb, and 14.63±0.11 ‰ (n = 6) at 15 ppb using the batch method. Thus no significant difference between the methods is evident. To calculate ΔpH from boron isotope data (δ^{11}B), we applied the approach outlined by Hain et al. (2018), which emphasizes reconstructing pH changes (ΔpH) over absolute pH. This method focuses on the difference in boron isotopic composition between two samples (δ_0 and δ_1), which minimizes errors associated with uncertainties in seawater boron isotopic composition ($\delta^{11}B_{SW}$) and reduces sensitivity to other parameters like temperature and salinity. Additionally, by focusing on ΔpH rather than absolute pH, this approach also mitigates the impact of systematic biases (e.g., vital effects or matrix differences between sample material and measurement standards) that affect both δ_0 and δ_1 similarly, making the ΔpH reconstruction more robust that absolute pH reconstructions. We compare our reconstructed ΔpH values with simulated ΔpH, calculated as the difference between the pH of the geologic carbon addition simulation and the control simulation with no geologic carbon added.

2.6.5 δ^{13}C Analytical Methods

Benthic δ^{13}C measurements of *P. ariminensis* were performed on a Thermo Kiel IV Carbonate Device connected to a Thermo MAT 253+ Isotope Ratio Mass Spectrometer at the Paleo^2 Laboratory at the University of Arizona. The δ^{13}C data are reported in permil notation relative to the Vienna Pee Dee Belemnite scale (‰, VPDB). IAEA-603 was analyzed (n=40) as an external standard, and the 1σ precision was 0.05‰ for ^{13}C, which is consistent with the long-term precision of this setup (0.05‰; n>1500).

2.6.6 CFC-11 Interpolation

To characterize the distribution of CFC-11 in the ETNP, we used data from the GLODAPv2 2023 dataset (Lauvset et al., 2024). Observational points within the ETNP were filtered for CFC-11 values at depths closest to 500 meters, then interpolated across a 2D grid using Ordinary Kriging with a linear variogram model, creating a continuous spatial representation of CFC-11 concentrations (Fig. 1B). Additionally, we note that Walczak et al. (2020), included in the global Δ^{14}C compilation for Figure 1A, required an updated age model. Consequently, it does not exhibit a mean deglacial Δ^{14}C reservoir age greater than 2500 years, as defined in our Δ^{14}C anomaly threshold.

Chapter 3

The isotopic fingerprint of marine CDR

3.1 Abstract

Achieving global climate targets requires large-scale carbon dioxide removal (CDR), with marine CDR (mCDR) offering significant potential due to the ocean's vast carbon reservoir and durable carbon storage. However, monitoring, reporting, and verification (MRV) of mCDR is challenging due to high background variability, slow air-sea gas exchange, and ocean dynamics. Conventional carbonate system measurements—such as alkalinity, dissolved inorganic carbon (DIC), pH, and pCO_2—reflect carbonate chemistry changes but cannot directly diagnose net atmospheric CO_2 uptake. Here, we demonstrate the utility of the stable carbon isotope $\delta^{13}C$ as a diagnostic tool for verifying CO_2 uptake following ocean alkalinity enhancement (OAE). Using a high-resolution ROMS-NEMUCSC simulation of the California Current System, we show that we show that changes in $\delta^{13}C$ track changes in DIC in a near-linear relationship before isotopic equilibrium occurs, providing a clear and direct fingerprint of net atmospheric CO_2 uptake. Unlike transient signals such as pH and pCO_2, the $\delta^{13}C$ signal persists on much longer timescales, providing an extended window for detecting and verifying carbon uptake, even in dynamic ocean environments where short-lived signals are often diluted by mixing and dispersion.

3.2 Introduction

Achieving global climate targets necessitates large-scale carbon dioxide removal (CDR) to complement emissions reductions (Lee et al., 2023; Masson-Delmotte et al., 2021). Among the suite of CDR strategies, marine CDR (mCDR) offers significant promise due to the ocean's vast carbon reservoir and its capacity for durable carbon storage (Friedlingstein et al., 2022; NASEM, 2021). However, monitoring, reporting, and verification (MRV) of CO_2 uptake remain formidable challenges (Ho et al., 2023). A primary hurdle is the high background variability of the marine carbonate system, which often exceeds the relatively small chemical perturbations induced by mCDR interventions (Wang et al., 2023). Moreover, due to the unique buffering capacity of carbon in the ocean, equilibration of CO_2 across the air-sea interface occurs over timescales of months to years (W. S. Broecker & Peng, 1974; Galbraith et al., 2015; Jones et al., 2014), further diluting the signal over broad spatial and temporal domains and complicating attribution to specific interventions (He & Tyka, 2023; Mu et al., 2023).

Given these measurement challenges, current MRV frameworks rely heavily on modeling to quantify carbon removal (Isometric OAE Protocol, 2024). While models remain critical tools for evaluating mCDR efficacy, determining how or if measurements can reliably verify these outcomes remains an active area of research and development (Ho et al., 2023). A typical MRV framework will include traditional carbonate system measurements—such as alkalinity, dissolved inorganic carbon (DIC), pH, and partial pressure of CO_2 (pCO_2)—to assess changes in seawater chemistry pre- and post-deployment. However, while these parameters effectively capture carbonate system dynamics, they cannot directly resolve net atmospheric CO_2 uptake without fully closing the carbon budget, a task that is logistically unfeasible due to the turbulent dispersion and dilution of the perturbed water mass over the timescales required for CO_2 equilibration (Ho et al., 2023).

Measuring the ratio of stable carbon isotopes ($^{13}C/^{12}C$), expressed using the $\delta^{13}C$ notation as a deviation from a standard $^{13}C/^{12}C$ ratio, offers a promising pathway to address this limitation. Due to their differing masses, certain physical, biological, and chemical processes preferentially utilize one carbon isotope over the other, a phenomenon known as isotopic fractionation. This process imparts distinct isotopic signatures to carbon

reservoirs within the Earth system, effectively giving carbon a source-specific fingerprint that can be used to track its origin and movement.

This ability to track carbon transfers using isotopes has been widely applied in climate and carbon cycle research. One of the earliest examples is the Suess Effect—the well-documented depletion of atmospheric δ^{13}C due to fossil fuel combustion (Keeling, 1979). As isotopically light anthropogenic CO_2 is absorbed by the ocean, it imprints a measurable δ^{13}C signal onto the marine DIC pool, making isotopes a key tracer of oceanic CO_2 uptake. Observational studies have tracked the progressive decline in surface ocean δ^{13}C, directly demonstrating the incorporation of anthropogenic carbon into the marine carbon cycle (P. Quay et al., 2003, 2007, 2017; P. D. Quay et al., 1992). Beyond simply quantifying uptake, oceanic δ^{13}C data have been instrumental in assessing interannual variability in the oceanic CO_2 sink, constraining biological fluxes, and improving estimates of the global carbon budget (Gruber et al., 2002; P. Quay & Stutsman, 2003; Schmittner et al., 2013; Tans et al., 1993).

Given its success in diagnosing natural ocean CO_2 uptake, δ^{13}C has also been applied to carbon capture and storage (CCS) to monitor geologically stored CO_2. Isotope-based monitoring techniques have been used to track injected CO_2 in subsurface reservoirs by leveraging the distinct isotopic signature of fossil-fuel-derived carbon (Flude et al., 2017). This same principle can be extended to the marine realm, where δ^{13}C provides a diagnostic tool for identifying net atmospheric CO_2 uptake in an open-ocean setting. Extending this approach to engineered interventions, this study evaluates the utility of δ^{13}C as a tracer for verifying CO_2 uptake following ocean alkalinity enhancement (OAE).

Using a high-resolution regional ocean model (ROMS) of the California Current System (CCS) coupled with the carbon isotope-enabled NEMUCSC biogeochemical model, we simulate OAE by adding 0.4 Tmole of alkalinity (equivalent to approximately 14 $GtCO_2$ removal at an efficiency of $\Delta DIC/\Delta ALK = 0.8$) over the course of one year off the coast of San Francisco. By comparing these results with a control simulation without OAE, we analyze the signals related to the carbonate system, including pH, pCO_2, DIC, alkalinity, and δ^{13}C.

Here, we define $\Delta\delta^{13}$C as the change in the isotopic composition of the DIC pool, calculated as the difference between the OAE simulation and the control ($\Delta\delta^{13}$CDIC, oae

- $\Delta\delta^{13}$CDIC, control). Our findings demonstrate that δ^{13}C provides a diagnostic signal that directly reflects net atmospheric CO_2 uptake, underscoring its potential as a robust tool for monitoring marine CDR interventions. Building on previous research that leverages δ^{13}C to diagnose air-sea gas exchange (W. S. Broecker & Peng, 1974; W. S. Broecker & Maier-Reimer, 1992; Charles et al., 1993; Galbraith et al., 2015; Lynch-Stieglitz et al., 1995; Tans, 1980), we evaluate the persistence and detectability of the δ^{13}C signal to assess its effectiveness as an MRV tool for marine CDR. These findings provide valuable insights into the practical application of δ^{13}C as a complementary tracer, strengthening MRV frameworks to ensure transparent, verifiable carbon removal necessary for addressing the climate crisis and supporting a credible CDR market.

3.3 δ^{13}C as a Diagnostic Signal of Marine CDR

Marine CDR is characterized by changes in dissolved inorganic carbon (DIC) concentrations driven by the uptake of atmospheric CO_2. Because atmospheric CO_2 holds a distinct isotopic fingerprint, a diagnostic relationship emerges between ΔDIC and $\Delta\delta^{13}$C. This relationship is evident in the surface $\Delta\delta^{13}$C and ΔDIC fields (Fig. 1A, 1B), which show nearly identical spatial patterns and distributions.

While the magnitudes of ΔDIC and $\Delta\delta^{13}$C changes differ—δ^{13}C declines by a maximum of $\sim$ -0.14‰, whereas ΔDIC increases by $\sim$25 mmol m^{-3} for this snapshot in time—their changes are highly correlated. This is highlighted in Fig. 1C, where grid-cell-level $\Delta\delta^{13}$C and ΔDIC values display a near-perfect linear relationship ($R^2 = -1.00$). This proportionality underscores the utility of δ^{13}C as a diagnostic tracer, as it reliably captures both the spatial distribution and relative magnitude of ΔDIC changes following marine CDR interventions.

The strong relationship between ΔDIC and $\Delta\delta^{13}$C arises because any CO_2 uptake driving ΔDIC carries a consistent isotopically light δ^{13}C signal. This signal is determined by the isotopic composition of atmospheric CO_2 (-8.4‰ in 2015, which will continue to decrease with fossil fuel emissions; Graven et al., 2020) and a small kinetic fractionation effect during air-sea exchange (ranging from -0.5 to -1.4‰; Jahn et al., 2015; see Methods). Consequently, CO_2 added to the ocean during mCDR has a predictable δ^{13}C fingerprint of approximately -10‰, which contrasts sharply with the ocean's relatively

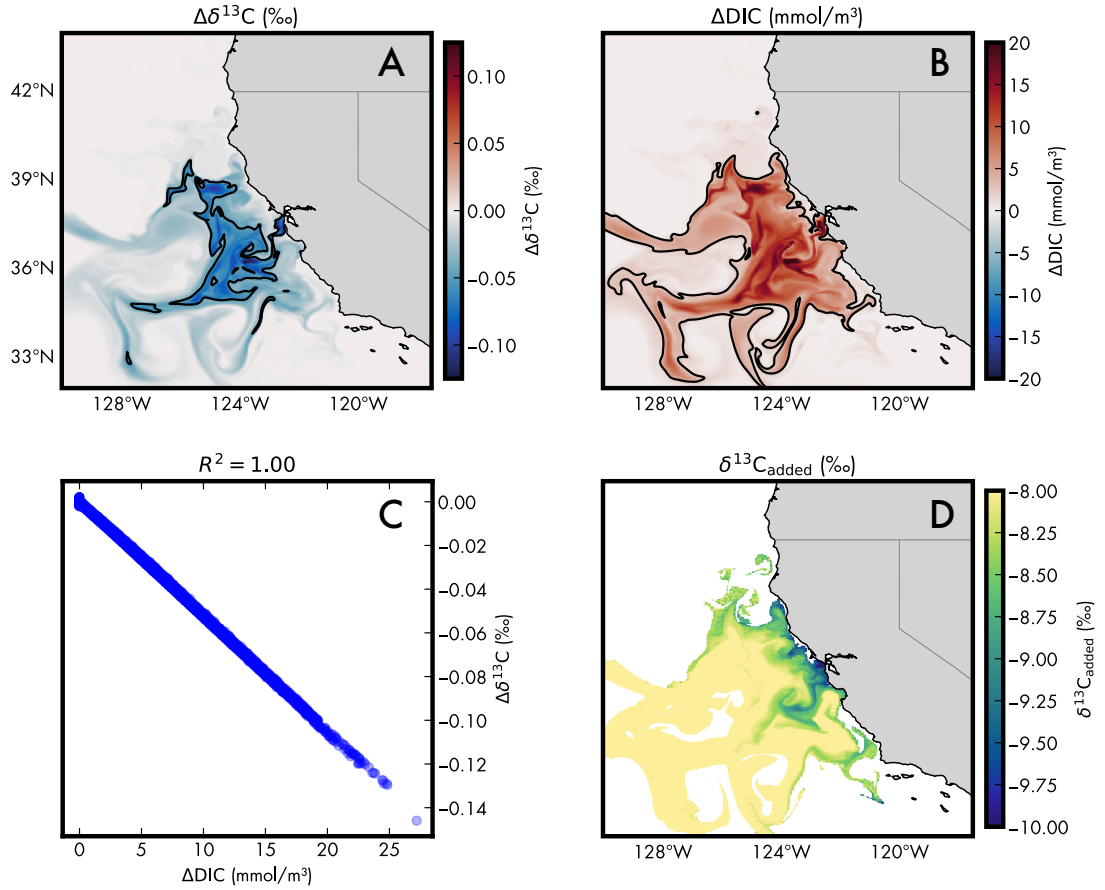

Figure 3.1: Surface maps and relationship of simulated $\Delta\delta^{13}$C and ΔDIC, and the δ^{13}C of added carbon for July 1 of year 1. Panel (A) displays the spatial distribution of $\Delta\delta^{13}$C (‰), with black contour lines indicating measurement precision at -0.05‰. Panel (B) illustrates the spatial distribution of ΔDIC (mmol/m^3), including black contour lines at a measurement precision of 2.5 mmol/m^3. The relationship between ΔDIC and $\Delta\delta^{13}$C for all grid cells at this time point is shown in Panel (C), which illustrates a highly linear relationship with an R^2 value of -1.00. Finally, Panel (D) shows the spatial distribution and magnitude of the $\delta^{13}C_{added}$ (‰) value of carbon introduced during mCDR.

heavy DIC pool (∼+1–2‰; Lauvset et al., 2024).

This relationship is robust in our controlled model setting, as other processes that could influence δ^{13}C are identical across simulations. We use a constant value for kinetic fractionation, given that the temperature dependence of kinetic fractionation is minimal (-0.81 ± 0.2‰ at 21°C and -0.95 ± 0.2‰ at 5°C; (Zhang & Quay, 1995)). Biological processes, while significant in natural systems, are held constant between the OAE and control simulations. These constraints ensure that simulated differences in $\Delta\delta^{13}$C arise solely from mCDR-induced CO_2 uptake.

Although the literature reports variability in kinetic fractionation factors (-0.5 to -1.4‰; Lynch-Stieglitz et al., 1995; Zhang and Quay, 1995), these differences are negligible compared to the ~ -10‰ offset between atmospheric CO_2 and the oceanic DIC pool due to temperature-dependent equilibrium fractionation (Lynch-Stieglitz et al., 1995; Schmittner et al., 2013). Because colder waters favor heavier δ^{13}C enrichment, the equilibrium fractionation offset between atmospheric CO_2 and oceanic DIC increases at lower temperatures. Specifically, δ^{13}C of DIC increases by approximately +0.1‰ per degree of cooling (W. S. Broecker & Maier-Reimer, 1992; Mook et al., 1974). This suggests that δ^{13}C signals may be particularly pronounced in colder regions such as the California Current System (CCS), where persistent coastal upwelling maintains low sea surface temperatures.

Our simulations confirm the isotopic fingerprint expected by theory, with regions of new CO_2 uptake showing δ^{13}C values of approximately -10‰. As this signal mixes with the background δ^{13}C of the DIC pool, it becomes slightly diluted to ~ -8‰ (Fig. 1D). However, this dilution occurs at the same rate as ΔDIC is integrated into the marine system, maintaining the strong relationship between $\Delta\delta^{13}$C and ΔDIC.

The CCS, as a western boundary current driving upwelling of CO_2-rich water, encompasses diverse air-sea CO_2 flux regimes, including coastal outgassing and offshore ingassing (Fiechter et al., 2014). Despite these flux variations, our simulations consistently show a clear δ^{13}C signal across different regimes. This outcome occurs because the $\Delta\delta^{13}$C signal reflects the net atmospheric CO_2 change rather than fluctuations in gross fluxes. These results demonstrate that δ^{13}C remains a reliable indicator of mCDR efficacy, even in complex ocean environments.

In contrast to δ^{13}C, pH and pCO_2 respond to carbonate chemistry changes driven first by alkalinity addition and later by CO_2 uptake. Initially, alkalinity addition increases pH and decreases pCO_2, reflecting shifts in the carbonate system. Over time, as atmospheric CO_2 is absorbed, these signals weaken as the system equilibrates. However, δ^{13}C remains unaffected by alkalinity addition itself; it changes only in response to atmospheric CO_2 uptake.

This distinction highlights the unique advantage of δ^{13}C as a tracer for marine CDR. Because pH and pCO_2 respond to both alkalinity addition and CO_2 uptake, distinguishing the signal from concurrent processes can be challenging, particularly when alkalinity is continuously added. In contrast, the δ^{13}C signal offers a direct fingerprint of net atmospheric CO_2 uptake, making it a powerful tool for monitoring and verifying marine CDR interventions.

However, as isotopic equilibrium progresses over time, deviations from the direct relationship between δ^{13}C and DIC will emerge as δ^{13}C values revert closer to the surface ocean baseline. This process and its implications will be explored in the next section.

3.4 Durability and Persistence of the δ^{13}C Signal

Given that it takes about 10 times as long to reach complete isotopic (δ^{13}C of DIC) equilibrium compared to CO_2 equilibrium (W. S. Broecker & Peng, 1974; Galbraith et al., 2015; Lynch-Stieglitz et al., 1995; Tans, 1980), the resulting δ^{13}C signal from a given mCDR intervention will also last $\sim$10 times longer than the pH or pCO_2 signals. This difference arises from the underlying equilibration mechanisms. While CO_2 equilibrium depends on the timescale of gas exchange ($\tau_{gasexchange}$) and the buffer capacity ($\partial CO_2/\partial DIC$, approximately 10 near our deployment site):

$$\tau_{CO_2} = \left(\frac{\partial DIC}{\partial CO_2}\right) \cdot \tau_{gasexchange},$$

the equilibration timescale for δ^{13}C scales linearly with the ratio of DIC to dissolved CO_2 (DIC/CO_2, approximately 115 near our deployment site):

$$\tau_{\delta^{13}C} = \left(\frac{DIC}{CO_2}\right) \cdot \tau_{gasexchange}.$$

The buffer capacity and DIC/CO_2 ratio vary spatially and temporally with changes in DIC and alkalinity, but our simulations confirm theoretical predictions that isotopic equilibration occurs on a timescale roughly 10 times slower than CO_2 equilibration. For example, the surface-average e-folding timescale of the δ^{13}C signal is 566 days, compared to 55 days for pCO_2 (Fig. 2A and 2C), demonstrating that isotopic signals persist far longer than carbonate chemistry signals following mCDR interventions.

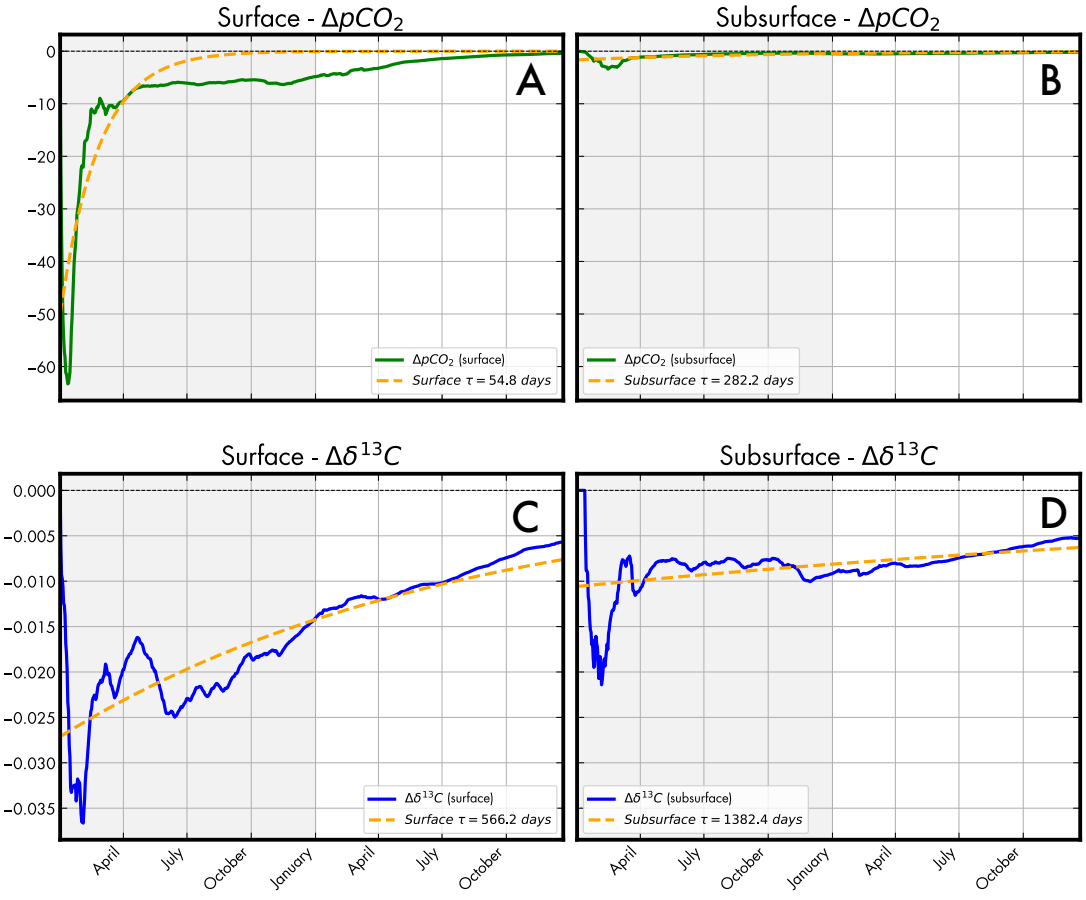

Figure 3.2: Time evolution of domain-averaged $\Delta\delta^{13}$C and ΔpCO$_2$ signals. Panels (A) and (B) show the change in ΔpCO_2 (green lines) for the surface layer (depth $<$ 50 m) and subsurface layer (depth $>$ 50 m), respectively. Panels (C) and (D) show the change in $\Delta\delta^{13}$C (blue lines) for the surface and subsurface layers. The signals are computed as domain-averaged values and fitted to an exponential decay function (dashed orange lines) to determine e-folding timescales, denoted as τ.

This durability is further evident in subsurface waters. Because pCO$_2$ equilibrates relatively quickly, its signal remains confined to the surface (Fig. 2B), which is beneficial for

maximizing CDR efficiency. In contrast, the longer equilibration timescale of δ^{13}C allows part of its signal to subduct into subsurface waters, where it can persist for years or even decades (Fig. 2D). Once isolated from the atmosphere, this subsurface δ^{13}C signal remains effectively locked in the DIC pool, providing a lasting record of mCDR-induced CO_2 uptake even after isotopic equilibrium occurs at the surface.

The persistence of the δ^{13}C signal offers a significant advantage for MRV frameworks in mCDR. While pH and pCO_2 are useful for detecting short-term changes, they are transient and quickly diminish as pCO_2 equilibrates. In contrast, δ^{13}C remains detectable long after the initial intervention, making it a robust tracer for tracking atmospheric CO_2 uptake, possibly even over decadal timescales.

Ultimately, the extended equilibration timescale of δ^{13}C reflects the slower turnover of the entire DIC pool via air-sea gas exchange (DIC/CO_2 compared to the timescale required for redistributing and re-equilibrating the DIC pool ($\partial DIC/\partial CO_2$) through air-sea gas exchange. The persistence of the δ^{13}C signal signal extends the time window for detecting and verifying carbon uptake, providing greater flexibility in sampling strategies and enhancing confidence in quantifying the impacts of mCDR interventions.

3.5 Detectability and Practicality of δ^{13}C for MRV

While δ^{13}C offers a persistent signal for long-term monitoring, its effectiveness as an MRV tool depends on its detectability against background variability and measurement uncertainty. Assessing its signal-to-noise ratio (SNR) and measurement precision is therefore critical for determining its practical utility in MRV frameworks.

To evaluate detectability, we compare the signals of δ^{13}C, DIC, pH, and pCO_2 against typical sensor or measurement uncertainties and calculate their SNR across the model domain (Fig. 3). The first column of Fig. 3 (A, D, G, and J) shows the intervention-induced Δ signal on July 1 of year one for each parameter. Overlaid black contour lines represent the thresholds for each variable's corresponding measurement precision: DIC = 2.5 μmol kg^{-1}, pH = 0.001, pCO_2 = 0.01 μatm (Briggs & Ringham, 2023), and δ^{13}C = 0.05 ‰ (Dubinina et al., 2024).

For this simulation, all variables exceed their respective measurement precision across

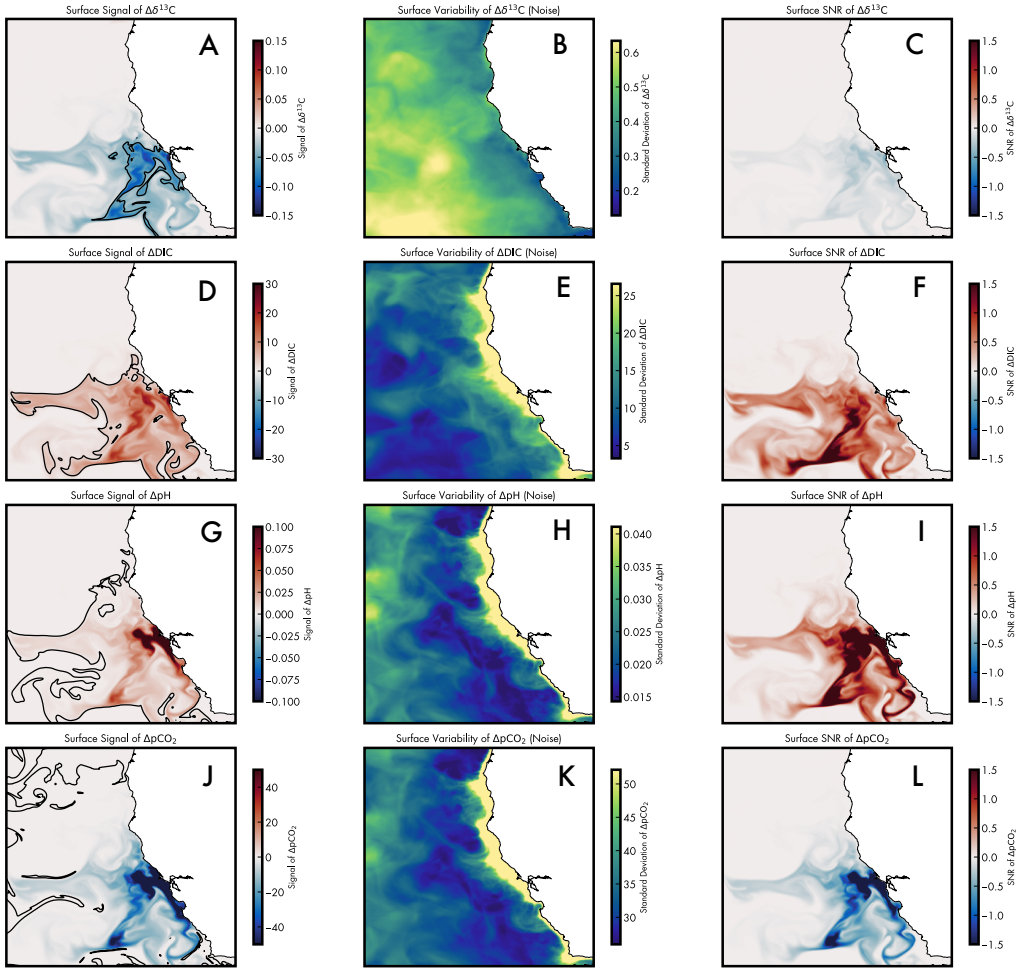

Figure 3.3: Detectability of each parameter on July 1 of the first simulation year. The first column (panels A, D, G, and J) shows the spatial distribution of the signal for $\Delta\delta^{13}$C, ΔDIC, ΔpH, and ΔpCO_2, respectively, with black contour lines representing the measurement precision for each parameter (DIC = 2.5 μmol kg^{-1}, pH = 0.001, pCO_2 = 0.01 μatm (Briggs & Ringham, 2023), and δ^{13}C = 0.05 ‰ (Dubinina et al., 2024)). The middle column (panels B, E, H, and K) shows the noise for each parameter, calculated as the one standard deviation of the parameter's variability over the course of a full year. The right column (panels C, F, I, and L) displays the signal-to-noise ratio (SNR) for each parameter.

large portions of the domain. The pCO_2 signal is the most prominent, exceeding precision by more than three orders of magnitude in many regions, followed by pH ($>$ 100 times precision), DIC ($>$ 10 times precision), and $\delta^{13}C$ ($>$ 3 times precision). While these results suggest that all parameters are detectable in principle, it is important to note that current precision thresholds are based on different methodologies. pCO_2, pH, and DIC can be measured in situ with sensors, while current $\delta^{13}C$ measurements typically require discrete water samples that must be collected and analyzed in the lab, presenting logistical challenges for large-scale sampling.

We further assess the detectability of these signals by calculating SNR, defined as the ratio of the intervention signal to natural background variability (Fig. 3, middle and right columns). Background variability (noise) is estimated as the standard deviation (σ) of each parameter over one year at each spatial location. Among the tracers, pH exhibits the highest SNR, followed by DIC and pCO_2, all of which have SNR values greater than 1, indicating strong detectability relative to background variability. In contrast, the SNR for $\delta^{13}C$ is less than 1, reflecting its smaller signal amplitude compared to natural variability.

These results demonstrate that for a gigaton-scale removal experiment (as modeled here), all variables except $\delta^{13}C$ are expected to be immediately detectable, as their SNR values exceed 1. While $\delta^{13}C$ has a lower SNR, it can still play a complementary role alongside high-SNR tracers like DIC, pH, and pCO_2, owing to its durable signal and direct connection to atmospheric CO_2 uptake. When validated through comparison with more measurable tracers, $\delta^{13}C$ could become a valuable complementary tool for verifying CO_2 uptake in MRV frameworks.

3.6 Discussion

This study underscores the utility of $\delta^{13}C$ as a diagnostic tracer for monitoring marine carbon dioxide removal (mCDR). By leveraging its unique isotopic fingerprint, $\delta^{13}C$ directly reflects net atmospheric CO_2 uptake. Unlike traditional parameters such as pH and pCO_2, which require closing the full carbon budget to quantify CO_2 uptake—a task often unfeasible in dynamic ocean environments (Ho et al., 2023)—$\delta^{13}C$ offers a distinct advantage. Its clear isotopic signal is tied directly to net CO_2 uptake and persists over

longer timescales than pH or pCO_2 signals. However, the results of this study indicate that $\delta^{13}C$ has a lower signal-to-noise ratio (SNR) compared to other tracers such as pH, DIC, and pCO_2. This result suggests that $\delta^{13}C$ is less immediately detectable, particularly in the short term, but retains significant value for long-term monitoring when combined with complementary tracers.

While these findings highlight the potential of $\delta^{13}C$, several steps are needed to advance its application in MRV. First, our calculation of noise in the SNR analysis was intentionally conservative, relying on a simple measure of variability (the standard deviation of one year of model output at each grid cell). This approach does not account for correlations between $\delta^{13}C$ and other oceanic tracers such as chlorophyll-a, oxygen, or DIC, which could be used to explain and predict some of the observed variability, thereby reducing noise and improving the effective SNR. Future analyses incorporating statistical or machine-learning approaches to isolate the $\delta^{13}C$ signal from biological and physical variability could provide a more refined estimate of detectability in real-world observations.

Second, scalable and reliable measurement techniques for measuring $\delta^{13}C$ are essential for its widespread adoption. While isotopic ratio mass spectrometry (IRMS) remains the gold standard, recent advances in field-deployable techniques such as cavity-enhanced laser absorption spectroscopy (CELAS) and cavity ringdown spectroscopy (CRDS) suggest growing feasibility for in situ measurements. These analyzers, when coupled with air-water equilibrators, have demonstrated their capability for quasi-continuous $\delta^{13}C$-CO_2 monitoring in aquatic environments (Becker et al., 2012; Friedrichs et al., 2010; Maher et al., 2015; Webb et al., 2016). However, operational challenges such as equilibration delays and response times remain significant barriers, and future work should prioritize refining calibration protocols and optimizing deployment strategies to enhance their applicability for MRV.

Finally, this study focuses on a gigaton-scale deployment in the California Current System using a regional model at 3 km resolution. While this scale emphasizes detectability in large interventions, current pilot projects operate at much smaller scales, where signals may be more difficult to resolve. Future work should explore $\delta^{13}C$'s detectability in these scenarios using higher-resolution models capable of capturing near-field processes.

Such efforts will help optimize monitoring strategies for small-scale experiments and enhance the feasibility of $\delta^{13}C$ for practical MRV applications.

By expanding the inclusion of carbon isotopes like $\delta^{13}C$ in ocean biogeochemical models and MRV frameworks, the scientific community can further validate their utility. Routine $\delta^{13}C$ measurements in pilot-scale mCDR deployments and model intercomparisons across diverse ocean conditions will be essential to refining these tools. Despite its lower SNR, the durability and diagnostic nature of $\delta^{13}C$ make it a valuable addition to MRV frameworks, particularly when used in conjunction with high-SNR tracers such as pH, DIC, and pCO_2. As global efforts to mitigate climate change accelerate, integrating isotopic tracers like $\delta^{13}C$ into MRV frameworks will be critical to ensuring the credibility and effectiveness of large-scale carbon removal strategies.

3.7 Methods

3.7.1 Model Description and Study Area

The physical circulation of the California Current System (CCS) was simulated using the Regional Ocean Modeling System (ROMS) (Haidvogel et al., 2008; Shchepetkin & McWilliams, 2005) This implementation features a high-resolution domain with a 1/30° (∼3 km) spatial resolution, spanning 30°N to 48°N and 115.5°W to 134°W (Figure S1). The vertical resolution of the model consists of 42 terrain-following levels with clustering near the surface and bottom. Surface wind and radiation forcing was derived from the ERA5 products (Hersbach et al., 2020), while boundary conditions were obtained from the GLORYS reanalysis (Jean-Michel et al., 2021). Versions of this model at different resolution and with different forcings have been described in (Drake et al., 2011; Fiechter et al., 2014; Veneziani et al., 2009). More information on its performance in this configuration can be found in Fiechter et al. (in prep).

The biogeochemical component of the model uses NEMUCSC, an adaptation of the North Pacific Ecosystem Model for Understanding Regional Oceanography (NEMURO) (Kishi et al., 2007) described in Fiechter et al. (2014). NEMUCSC includes key biogeochemical processes, modeling three macronutrients (nitrate, ammonium, and silicic acid), two functional phytoplankton groups (nanophytoplankton and diatoms), three

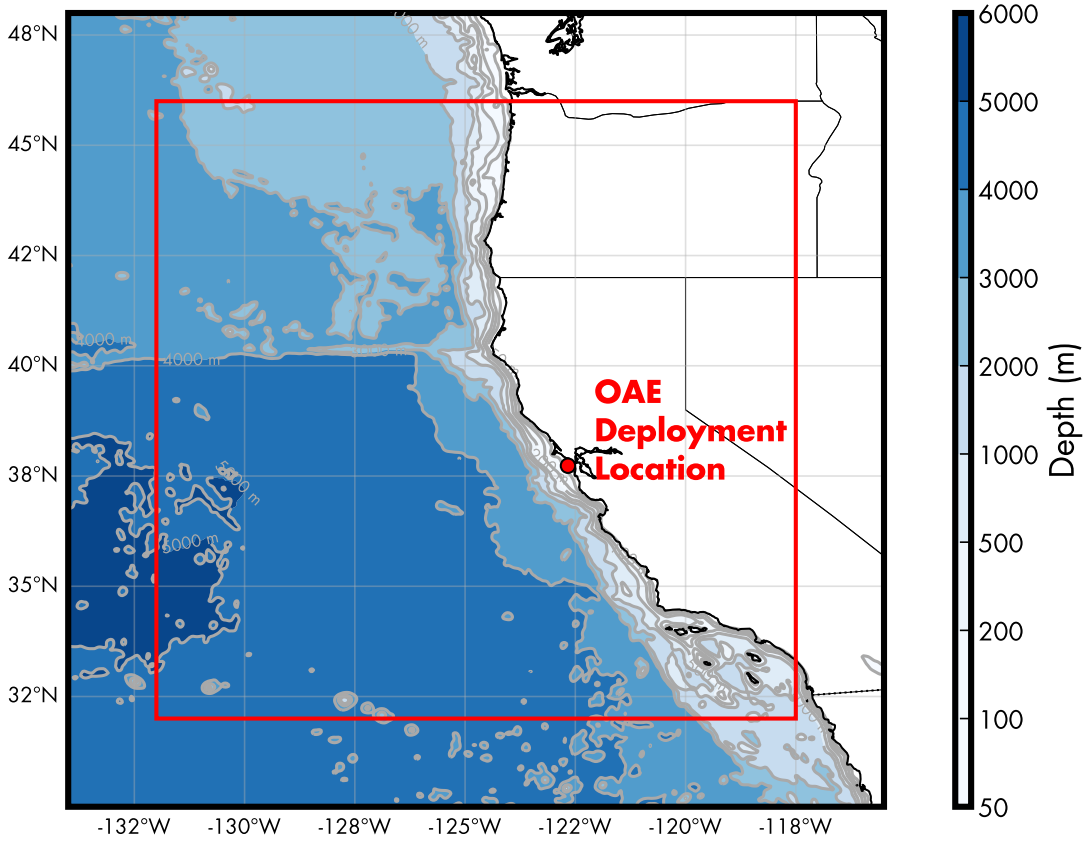

Figure 3.4: ROMS model domain for the California Current System, with bathymetry contours shown in blue. Depths are shown in meters. Inside the red square indicates the region analyzed in this study to avoid edge effects. The location of the ocean alkalinity enhancement (OAE) deployment is marked off the coast of San Francisco.

zooplankton size classes (microzooplankton, mesozooplankton, and predatory zooplankton), and three detrital pools (dissolved and particulate organic nitrogen and particulate silica).

The model also integrates carbon and oxygen cycles (Fiechter et al., 2014). The carbon submodel simulates dissolved inorganic carbon (DIC), total alkalinity (TA), and calcium carbonate ($CaCO_3$). Ocean pH and partial pressure of CO_2 (pCO_2) are computed using the Ocean Carbon Model Intercomparison Project (OCMIP) carbonate chemistry formulation (Orr et al., 2017). Atmospheric pCO_2 is fixed at 400 ppm.

3.7.2 Model Enhancements and Modifications

Carbon Isotope Implementation

To extend the diagnostic capabilities of the NEMUCSC biogeochemical model, stable carbon isotopes (^{13}C) and radiocarbon (^{14}C) were incorporated as additional tracers. The model tracks concentrations of the isotopic forms of dissolved inorganic carbon (DI^{13}C and DI^{14}C). To minimize numerical error from carrying small numbers, we scale these isotope tracers by their respective standard ratios, 1.12372×10^{-8} for ^{13}C (Craig, 1957) and 1.176×10^{-12} for ^{14}C (Karlen et al., 1965). For ^{14}C, all fractionation factors are doubled because isotopic fractionation scales with the mass difference between isotopes. Since ^{14}C is two atomic mass units heavier than ^{12}C, compared to ^{13}C, which is only one atomic mass unit heavier, the fractionation effects for ^{14}C are approximately twice as large (Zeebe & Wolf-Gladrow, 2001).

Air-Sea Gas Exchange of ^{13}C

The air–sea flux of ^{13}C is calculated following Zhang et al. (1995):

$$F^{13} = CO_2^{sol} \cdot k \cdot \alpha_{\mathrm{aqg}} \cdot \alpha_k \cdot \left(R^{13}_{\mathrm{atm}} \cdot pCO_2^{\mathrm{air}} - \frac{R^{13}_{\mathrm{DIC}} \cdot pCO_2^{\mathrm{ocean}}}{\alpha_{\mathrm{DICg}}} \right).$$

where

$$k = 0.31 \cdot u^2 (Sc/660)^{-1/2}.$$

CO_2^{sol} is the temperature and salinity dependent solubility of CO_2, pCO_2^{air} is the CO_2 partial pressure in the atmosphere and pCO_2^{ocean} is the partial pressure of CO_2 in sea-

water. Oceanic pCO_2^{ocean} is calculated from DIC, alkalinity, temperature and salinity using the standard OCMIP carbonate chemistry routines (Orr et al., 2017). The routines used the carbonic acid dissociation constants of Mehrbach et al. (1973), as refit by Dickson and Millero (1987) and Dickson (1990). The pressure effect on the solubility was estimated from the equation of Mucci (1983), including the adjustments to the constants recommended by Millero (1995). The gas transfer coefficient, k, is given by Wanninkhof (1992) and dependent on the square of the instantaneous wind speed (u) and the temperature dependent Schmidt number (Sc).

Carbon Isotope Implementation

$\alpha_k = 0.99919$ is the constant kinetic fractionation factor from Zhang et al. (1995), where the associated **kinetic enrichment factor** is $\varepsilon_k = -0.81‰$. The fractionation factor is related to the enrichment factor by:

$$\alpha_k = \frac{\varepsilon_k}{1000} + 1.$$

Kinetic fractionation occurs during gas exchange due to the faster diffusion of $^{12}CO_2$ compared to $^{13}CO_2$, leading to preferential uptake of the lighter isotope.

α_{aqg} represents the **equilibrium fractionation factor** associated with the dissolution of CO_2 gas into aqueous solution. This fractionation is temperature dependent and is given by the corresponding **equilibrium enrichment factor** ε_{aqg}, derived from Zhang et al. (1995):

$$\varepsilon_{\text{aqg}} = -0.0049 \cdot \text{T } (^\circ\text{C}) - 1.31.$$

The temperature and carbonate fraction (f_{CO_3}) dependent fractionation factor (α_{DICg}) between total DIC and CO_2 is based on the empirical relationship for $\varepsilon_{\text{DICg}}$, which represents the **equilibrium enrichment factor** associated with carbon speciation between DIC and gaseous CO_2:

$$\varepsilon_{\text{DICg}} = 0.014 \cdot \text{T } (^\circ\text{C}) \cdot f_{CO_3} - 0.105 \cdot \text{T } (^\circ\text{C}) + 10.53.$$

However, following Schmittner et al. (2013), we ignore f_{CO_3} due to its relatively small impact on $\varepsilon_{\mathrm{DICg}}$ compared to temperature.

R^{13}_{atm} is the $^{13}C/^{12}C$ ratio in atmospheric CO_2. The value of $\delta^{13}C_{\mathrm{atm}}$ is held constant at -8.4‰ (Graven et al., 2020). R^{13}_{DIC} is the $^{13}C/^{12}C$ ratio of dissolved inorganic carbon, calculated from the simulated DIC and DI^{13}C pools.

Biological Fractionation of ^{13}C

Isotopic fractionation during photosynthesis ($\alpha_{\mathrm{POC}\leftarrow\mathrm{DIC}}$, herein α_p) is calculated as:

$$\alpha_p = \alpha_{\mathrm{aq}\leftarrow\mathrm{g}} \cdot \alpha_{\mathrm{DIC}\leftarrow\mathrm{g}} \cdot \alpha_{\mathrm{POC}\leftarrow\mathrm{aq}},$$

where:

- $\alpha_{\mathrm{POC}\leftarrow\mathrm{DIC}}$ (α_p) is the overall fractionation factor from dissolved inorganic carbon (DIC) to particulate organic carbon (POC).

- $\alpha_{\mathrm{aq}\leftarrow\mathrm{g}}$ is the fractionation factor between gaseous CO_2 and aqueous CO_2.

- $\alpha_{\mathrm{DIC}\leftarrow\mathrm{g}}$ represents the equilibrium fractionation between the total DIC pool and gaseous CO_2.

- $\alpha_{\mathrm{POC}\leftarrow\mathrm{aq}}$ is the fractionation factor between aqueous CO_2 and POC.

Empirical relationships for these fractionation factors ($\alpha_{\mathrm{aq}\leftarrow\mathrm{g}}$, $\alpha_{\mathrm{DIC}\leftarrow\mathrm{g}}$, and $\alpha_{\mathrm{POC}\leftarrow\mathrm{aq}}$) have been established through laboratory experiments, observations of modern oceans and lakes, and analysis of the sedimentary record. However, there are still uncertainties in parameterizing $\alpha_{\mathrm{POC}\leftarrow\mathrm{aq}}$, particularly due to biological variability in fractionation.

Following Popp et al. (1998), we use the fractionation factor from aqueous CO_2 to POC as:

$$\alpha_{\mathrm{POC}\leftarrow\mathrm{aq}} = -0.017 \cdot \log(C_{\mathrm{surf}}) + 1.0034,$$

where C_{surf} represents the concentration of aqueous CO_2 at the surface. Because dissolved CO_2 and carbonic acid (H_2CO_3) exist in rapid equilibrium in seawater, they are often combined into a single term, denoted as $CO_2{}^*$.

Passive Tracers

Passive tracers were introduced to track the fate of added alkalinity through the model domain. These tracers facilitate detailed budget analyses, allowing for the quantification of intervention-induced changes in TA across depth and spatial scales.

Refinements to Alkalinity and Carbon Dynamics

Several refinements were made to improve the representation of alkalinity and carbon fluxes:

- Alkalinity changes due to respiration were explicitly linked to the production of nitrate ($NO_3{}^-$) and ammonium ($NH_4{}^+$).
- Zooplankton excretion was incorporated as a source of ammonium-driven alkalinity changes.
- Nitrification was corrected to reduce alkalinity by 2 equivalents per mole of ammonium oxidized, resolving a discrepancy in the prior implementation.
- Decomposition of particulate organic nitrogen (PON) and dissolved organic nitrogen (DON) into ammonium was explicitly linked to alkalinity changes.

3.7.3 Experimental Design

The OAE scenario was designed to simulate a large-scale intervention off the coast of San Francisco. A total of 0.4 Tmol of alkalinity was added over the course of one year, corresponding to approximately 14 Gt of CO_2 removal, assuming an efficiency of $\Delta\text{DIC}/\Delta\text{ALK} = 0.8$. After the alkalinity addition stopped, the model was simulated for an additional year to observe the resulting effects. Atmospheric $\delta^{13}C$ was fixed at $-8.4‰$ (Graven et al., 2020), and atmospheric CO_2 was held constant at 400 ppm.

Concluding remarks

This dissertation demonstrates the versatility of carbon isotopes for understanding both past carbon cycle dynamics and future climate solutions. By analyzing radiocarbon anomalies in the Eastern Tropical North Pacific, we refined constraints on a natural analog to ocean alkalinity enhancement (OAE) during the last deglaciation. Through a combination of global and regional modeling approaches, constrained by multiple isotope systems, we showed that large-scale release of neutralized carbon represents the only plausible explanation for these long-standing anomalies, effectively resolving a key uncertainty in the interpretation of past ^{14}C records.

This finding provides valuable insights into the feasibility of OAE as a carbon dioxide removal (CDR) strategy by demonstrating that substantial neutralized carbon addition can be durably stored in the ocean without significantly altering ocean chemistry or driving atmospheric CO_2 rise. Our results suggest that up to 2,400 Pg C—nearly five times cumulative anthropogenic CO_2 emissions (∼500 Pg C; Friedlingstein et al., 2022)—could have been added to the ocean without large-scale disruptions to carbonate chemistry at the basin scale. This reinforces the potential for OAE as a durable and safe CDR strategy.

Moreover, these results highlight the dynamic nature of the glacial-interglacial carbon cycle, suggesting that seafloor carbon fluxes may have played a more significant role than previously recognized. If such large-scale neutralized carbon addition occurred during the last deglaciation, similar processes may have operated throughout Earth's history. Investigating these natural events further could provide valuable context for both OAE feasibility and broader carbon cycle dynamics, offering new perspectives on Earth's ability to regulate atmospheric CO_2 over geologic timescales.

Building on these paleoceanographic insights, this dissertation also establishes that carbon isotopes can serve as robust verification tools for modern alkalinity enhancement. Our modeling of the California Current System demonstrates that stable carbon isotopes (δ^{13}C) can effectively track atmospheric CO_2 uptake following OAE, providing a direct diagnostic of net air-sea carbon exchange. Unlike traditional carbonate system measurements, which require closing the full carbon budget to quantify CO_2 uptake, δ^{13}C offers a distinct advantage by encoding the atmospheric isotopic fingerprint into the ocean. Additionally, because isotopic equilibration occurs more slowly than CO_2 equilibration, δ^{13}C provides a longer-lasting signal of net carbon uptake, extending the timeframe for detection. This property allows for more reliable attribution of CO_2 removal to OAE interventions, enhancing the rigor of monitoring, reporting, and verification (MRV) frameworks.

Despite these advancements, key challenges remain. While δ^{13}C provides a persistent signal of net carbon uptake, its signal-to-noise ratio is lower than other chemical tracers such as pH, DIC, and pCO_2. However, the noise estimates presented in this study are conservative, and further refinements—such as integrating complementary tracers to account for predictable variability—can reduce the noise and, in turn, the detectability of a δ^{13}C signal. Expanding δ^{13}C measurements, particularly in pilot-scale OAE deployments, will be crucial for validating its role in MRV frameworks. Moving forward, establishing a reliable verification framework for marine CDR will require a comprehensive, multi-tracer approach that leverages all available tools. Given the urgency of scaling carbon removal, an adaptive strategy—testing multiple methods, refining approaches, and integrating new insights as they emerge—will be essential for ensuring effective and credible CDR.

The broader significance of this research lies in its dual contributions to understanding both natural and engineered alkalinity addition in the ocean. By identifying and characterizing a natural OAE analog during the last deglaciation, this work provides a real-world example of how large-scale neutralized carbon addition operates in the Earth system. This natural experiment—recorded in radiocarbon and boron isotope signatures—demonstrates that substantial quantities of carbon can be durably sequestered through alkalinity-mediated processes without destabilizing ocean chemistry. Such paleoceanographic evidence offers crucial validation for OAE as a carbon removal approach,

showing that similar processes have occurred naturally at scales relevant to our current climate challenges.

At the same time, this dissertation underscores the value of paleoclimate science in addressing modern climate challenges. Carbon isotope geochemistry, long used to reconstruct past Earth system dynamics, can also serve as a critical tool for monitoring carbon removal in the future. By integrating isotope-based approaches into regional ocean models and MRV frameworks, this work bridges fundamental and applied carbon cycle science, demonstrating how paleoclimate expertise can inform solutions to the climate crisis. As efforts to scale CDR accelerate, these connections between past and future carbon cycle dynamics will be essential, reinforcing the idea that some of our most powerful tools for addressing climate change come from studying Earth's history.

Appendix A

Supplementary materials for: Deglacial Pulse of Neutralized Carbon From the Pacific Seafloor: A Natural Analog for Ocean Alkalinity Enhancement?

Text S1 Model configuration

We use the CYCLOPS global carbon cycle box model and deglacial carbon cycle scenario of Hain et al. (2014) as our baseline control run, but with an initial 2700 Pg terrestrial carbon reservoir and an increased model temperature of 1.1C, to raise the simulated LGM CO_2 from 179 ppm in Hain et al. (2014) to 188 ppm and preindustrial CO_2 from 268 ppm in Hain et al. (2014) to 281 ppm (Figure 2a). The model includes a constant $CaCO_3$ weathering flux of 0.192 Pg C yr^{-1} and saturation state dependent $CaCO_3$ preservation and burial on the deep seafloor, yielding a 113 μmol kg^{-1} net loss of bulk ocean alkalinity throughout the deglacial control run (i.e., 1875 Pg C net $CaCO_3$ burial). The control run deglacial scenario (Hain et al., 2014) includes changes in ocean circulation, nutrient utilization, and productivity intended to mimic LGM Subantarc-

tic iron fertilization, shoaling of the Atlantic Meridional overturning circulation, and Antarctic surface isolation (Hain et al., 2010; Sigman et al., 2021). In this scenario, the ocean's biological pump weakens during the deglaciation, causing a deglacial $CaCO_3$ preservation event, with the loss of biological carbon sequestration and ocean alkalinity significantly contributing to the simulated CO_2 rise (Hain et al., 2010). The model also includes time-varying ^{14}C production modulated by the GLOPIS-75 record of Earth's magnetic field (Kovaltsov et al., 2012; Laj et al., 2004), as described in Hain et al. (2014), yielding a 19% decline in the global ^{14}C inventory since the LGM and simulated atmospheric $\Delta^{14}C$ broadly matching the temporal pattern of the IntCal13 and IntCal20 data products (Reimer et al., 2013, 2020) (Figure 2a, d, g, j). The simulations presented in this study include all these background changes of the control run, providing us with a framework to assess other fluxes of the open-system carbon cycle. We acknowledge that the control run from (Hain et al., 2014) has certain limitations, and by utilizing it as a starting point, we inevitably integrate all its biases into our future experiments. However, the LGM carbon cycle forcing of CYCLOPS is well documented (Hain et al., 2010) and consistent with reconstructed surface ocean pH changes (Chalk et al., 2017; Hain et al., 2018), and the deglacial model scenario of (Hain et al., 2014) agrees reasonably well with subsequent ^{14}C measurements and data compilations (Rafter et al., 2022).

Text S2. Numerical Algorithm Design

We develop a numerical algorithm based on Powell's method (Press et al., 2007) to iteratively minimize the deviation between $CO_{2\text{model}}$ and $\Delta^{14}C_{\text{model}}$ compared to $CO_{2\text{obs}}$ (Bereiter et al., 2015) and $\Delta^{14}C_{\text{obs}}$ (Reimer et al., 2020). The algorithm is evaluated at 100-year time steps to find the optimized rate of open-system carbon and alkalinity fluxes (terrestrial and submarine) to minimize the mismatch represented by the weighted objective function. The objective function is given approximately equal weight to the two data constraints by scaling the misfit relative to the 90 ppm and the 250‰ magnitude of glacial/interglacial CO_2 and $\Delta^{14}C$ change presumed to be driven by the global carbon cycle:

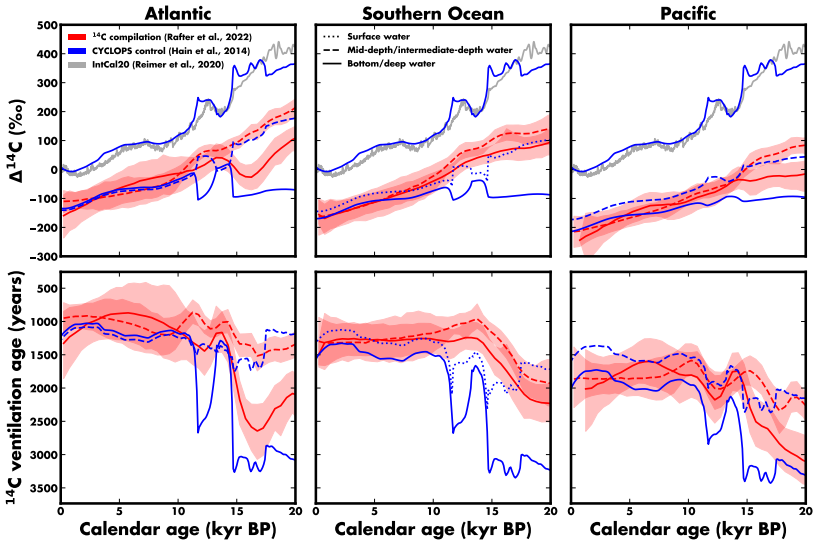

Figure A.1: Comparison of the deglacial scenario from our control simulation (Hain et al., 2014) with a new ^{14}C compilation (Rafter et al., 2022). Simulated Δ^{14}C and ^{14}C ventilation ages from (Hain et al., 2014) are compared to observed Δ^{14}C and ^{14}C ventilation ages from (Rafter et al., 2022). The envelope around the red lines represents the LOESS 95% confidence interval for the ^{14}C compilations. Blue dashed lines depict CYCLOPS intermediate-depth waters (200–1500 m depth; (Hain et al., 2014)), and red dashed lines represent mid-depth waters (27.5–28.0 kg m^{-3} neutral density surfaces; (Rafter et al., 2022)). Blue solid lines show CYCLOPS deep water (>1500 m depth), while red solid lines represent bottom water (>28.0 kg m^{-3} neutral density surfaces; (Rafter et al., 2022)).

$$\{(\mathrm{CO_2}, \Delta^{14}\mathrm{C}) = \frac{|\mathrm{CO_{2obs}} - \mathrm{CO_{2model}}|}{90 \text{ ppm}} + \frac{|\Delta^{14}\mathrm{C_{obs}} - \Delta^{14}\mathrm{C_{model}}|}{250‰}$$

Further, we implement a dampening strategy to introduce a low-pass filter suppressing short-term fluctuations in carbon and alkalinity release while allowing the algorithm to converge on $\mathrm{CO_{2obs}}$ and $\Delta^{14}\mathrm{C_{obs}}$ over timescales greater than the minimization time step of 100 years. Additionally, since the objective function is based on instantaneous atmospheric values ($\mathrm{CO_{2obs}}$ and $\Delta^{14}\mathrm{C_{obs}}$), we use a greater dampening effect (smaller dampening term) for optimized submarine fluxes compared to optimized terrestrial carbon cycle fluxes, to account for the residence time of oceanic carbon before ventilation with the atmosphere. As a result, our dampening parameters are 0.016 for optimized submarine carbon cycle fluxes and 0.55 for optimized terrestrial carbon cycle fluxes. These parameters were also optimized by selecting values between 0 and 1 that mini-

mize the model-data misfit.

Text S3 Experimental Design

We present four experiments, progressively adding optimized and imposed open-system carbon and alkalinity fluxes:

1. We invert for the optimal rates of carbon and alkalinity release to the mid-depth North Pacific region of the model (**experiment NP**).

2. We add the possibility of land carbon uptake to the optimization (**experiment NP+LC**).

3. We include the release of ^{14}C-free permafrost carbon (**experiment NP+LC+PF**).

4. We adjust the initial LGM ^{14}C inventory by +3.5% (**experiment NP+LC+PF+RC**).

All these scenarios include the identical background forcings of the control run.

The first experiment (**NP**) allows for the release of ^{14}C-free carbon with a variable proportion of alkalinity to the mid-depth North Pacific model region, but only if the simulated Δ^{14}C is greater than IntCal20, since geologic carbon will ultimately lower atmospheric Δ^{14}C. Removal of DIC is not permitted, and the alkalinity flux is constrained to ALK-to-DIC ratios in the range 0 to 2, where a ratio of 0 corresponds to CO_2 release, a ratio of 1 corresponds to HCO_3^- (bicarbonate ion) release, and a ratio of 2 corresponds to adding CO_3^{2-} (carbonate ion, likely through the addition of dissolved $CaCO_3$). As discussed further below, the $\Delta^{14}C_{obs}$ constraint tends to determine the optimal carbon release rate, while the CO_{2obs} constraint mainly affects the optimal ALK-to-DIC ratio.

The second experiment (**NP+LC**) allows for net land carbon uptake in addition to North Pacific carbon/alkalinity release, but only if CO_{2model} is greater than CO_{2obs} and the atmospheric Δ^{14}C model-data misfit is less than 20‰. These conditions were selected to favor land carbon uptake during the Holocene, when simulated alkalinity loss from ongoing carbonate compensation in the control run tends to raise atmospheric CO_2. With this deliberate heuristic, our algorithm can determine the optimal instantaneous rate of land carbon uptake and hence the integrated change in land carbon

storage through time. The CO_{2obs} constraint primarily drives the optimization of land carbon uptake with only a minor impact on simulated atmospheric $\Delta^{14}C$ stemming indirectly from the CO_2 dependence of the air/sea carbon isotope equilibration (Bard, 1998; Galbraith et al., 2015).

The third experiment (**NP+LC+PF**) allows the addition of ^{14}C-free CO_2 into the atmosphere to represent the impact of permafrost destabilization and carbon release. This optimized open-system permafrost flux is only activated when the optimization algorithm would otherwise add CO_2 into the mid-depth North Pacific, instead releasing the equivalent amount of CO_2 directly to the atmosphere. The algorithm still optimizes for the geologic addition of bicarbonate and carbonate into the mid-depth North Pacific as in the previous experiments. This sensitivity experiment intends to assess how early deglacial permafrost carbon release changes the inversion solution relative to the **NP+LC** experiment, with the expectation that permafrost carbon release will reduce the opportunity for geologic carbon release based on the $\Delta^{14}C_{obs}$ constraint.

The fourth experiment (**NP+LC+PF+RC**) imposes a 3.5% greater initial ^{14}C inventory as a means of assessing model bias from the uncertain history of Earth's magnetic field and ^{14}C production (Dinauer et al., 2020; Roth & Joos, 2013), which are used to calculate $\Delta^{14}C_{model}$ (Hain et al., 2014). Additionally, this experiment accounts for uncertainty in $\Delta^{14}C_{obs}$ at the LGM, as there has been disagreement in the last three iterations of IntCal (Fig. 3a). After this change in the initial state, the LGM $\Delta^{14}C_{model}$ increases from 365‰ in the control run to 413‰, bringing the model's initial LGM $\Delta^{14}C$ into closer agreement with reconstructions (∼425‰). This speculative sensitivity experiment intends to assess how the model bias of a low LGM ^{14}C inventory may hide a substantial opportunity for geologic carbon release within the $\Delta^{14}C_{obs}$ constraint.

Text S4 Neutralized carbon sources considered and their $\delta^{13}C$ values

We consider two plausible geological carbon sources in the marine sedimentary environment that produce neutralized carbon.

The first was suggested by (Rafter et al., 2019), combining the two known sedimentary

processes of basaltic sill intrusion and anaerobic oxidation of methane (AOM). Basaltic sill intrusion can produce thermogenic methane from sedimentary organic carbon, and that methane can be anaerobically oxidized into bicarbonate. We use a $\delta^{13}C$ value of -25‰ for this pathway due to the $\delta^{13}C$ of marine organic matter ranging from -31‰ to -19‰ (Mackensen & Schmiedl, 2019).

The second geologic source was proposed by (Skinner & Bard, 2022), consisting of subsurface geologic CO_2 (L. Stott et al., 2019) dissolving carbonates deep in the sediment column. With mantle CO_2 estimated to have a $\delta^{13}C$ value of approximately -5‰ and $CaCO_3$ shells around 0‰ (Mackensen & Schmiedl, 2019), we designate a $\delta^{13}C$ value of -2.5‰ for the carbonate dissolution pathway.

Table A.1: Results from the four experimental simulations. All carbon amounts are in Pg C, except "Net ALK-to-DIC ratio" and "% HCO_3^-" which are unitless. Values reported are totals at the end of the 20 kyr simulation.

Variable	**NP**	**NP+LC**	**NP+LC+PF**	**NP+LC+PF+RC**
CO_2 (Pg C)	143	145	-	-
HCO_3^- (Pg C)	568	678	711	1933
CO_3^{2-} (Pg C)	219	149	138	464
Geologic carbon added (Pg C)	929	970	846	2396
Terrestrial carbon uptake (Pg C)	-	300	279	550
Terrestrial carbon release (Pg C)	-	-	105	97
Net ALK-to-DIC ratio	1.08	1.00	1.16	1.19
% HCO_3^-	61	70	84	81

Appendix B

Additional Work Related to Chapter 3

Supplementary Work for Chapter 3

This appendix includes additional work conducted during the development of Chapter 3. The following sections provide an overview of various experiments, modeling approaches, and preliminary results that contribute to the broader context of this research.

B.1 OAE Budget Analysis

A key aspect of this study is evaluating the effectiveness of ocean alkalinity enhancement (OAE) in the California Current System (CCS). While Chapter 3 primarily focuses on using $\delta^{13}C$ as a measurement, reporting, and verification (MRV) tool, it is equally important to demonstrate that the OAE intervention effectively removes atmospheric CO_2. To address this, we conducted a comprehensive budget analysis to quantify carbon and alkalinity transport within and beyond the model domain.

Most previous estimates of OAE efficiency have been derived from global ocean models (Zhou et al., 2024), which provide valuable system-wide tracking of carbon and alkalinity over long timescales. These models offer critical insights into large-scale overturning circulation and ventilation processes. However, their coarse resolution limits their ability

to resolve fine-scale ocean circulation, which strongly influences whether added alkalinity remains in surface waters for CO_2 uptake or is transported away before equilibration occurs.

To overcome these limitations, regional ocean models provide higher spatial resolution, allowing us to resolve key physical processes controlling the fate of added alkalinity. Regional models have been successfully applied to coastal OAE studies, such as Mongin et al. (2021) in the Great Barrier Reef and Wang et al. (2023) in the Bering Sea, demonstrating their ability to simulate alkalinity transport and air-sea CO_2 exchange with greater detail than global models. However, a major limitation of regional models is that they cannot track carbon and alkalinity beyond their domain boundaries, meaning any CO_2 uptake occurring outside the model's spatial extent remains unaccounted for. This issue is particularly relevant in open-ocean systems, where alkalinity-enriched waters may exit the domain before fully equilibrating with the atmosphere (Wang et al., 2023).

In this study, we bridge this gap by using a high-resolution (1/10°) Regional Ocean Modeling System (ROMS) simulation to track the fate of alkalinity both within the model domain and beyond its boundaries. Unlike previous studies that only estimated boundary losses, we explicitly quantify the amount of un-equilibrated alkalinity leaving the model and estimate the additional CO_2 uptake that occurs beyond the regional domain. By assessing total efficiency across surface and subsurface waters, both within and outside the model domain, we provide a more complete evaluation of OAE effectiveness in the CCS.

Figure B.1 presents the preliminary results of this budget analysis, tracking the fate of added alkalinity (OAE), its interaction with dissolved inorganic carbon (DIC), and the net CO_2 removal (CDR) across the system. The top row shows net fluxes of alkalinity (blue; OAE), CO_2 uptake (red/orange; CDR), and unreacted alkalinity—representing OAE-affected waters that have yet to reach their full CDR potential (dashed black)—within the model domain (left), beyond the model domain (center), and across the total system (right). The bottom row tracks cumulative inventories of alkalinity and DIC over time, distinguishing between retained and exported fractions.

These results confirm that the majority of added alkalinity remains within the surface

ocean long enough to facilitate CO_2 uptake, with the model approaching the theoretical maximum efficiency of ~0.8 mol CO_2 per mol ALK added within two years. While some unequilibrated alkalinity is transported outside the model boundaries before fully equilibrating, our results show that additional CO_2 uptake will continue beyond the domain until the system reaches its full CDR potential. By explicitly quantifying these fluxes, this analysis provides a more comprehensive picture of OAE efficiency, overcoming the limitations of both global and regional models.

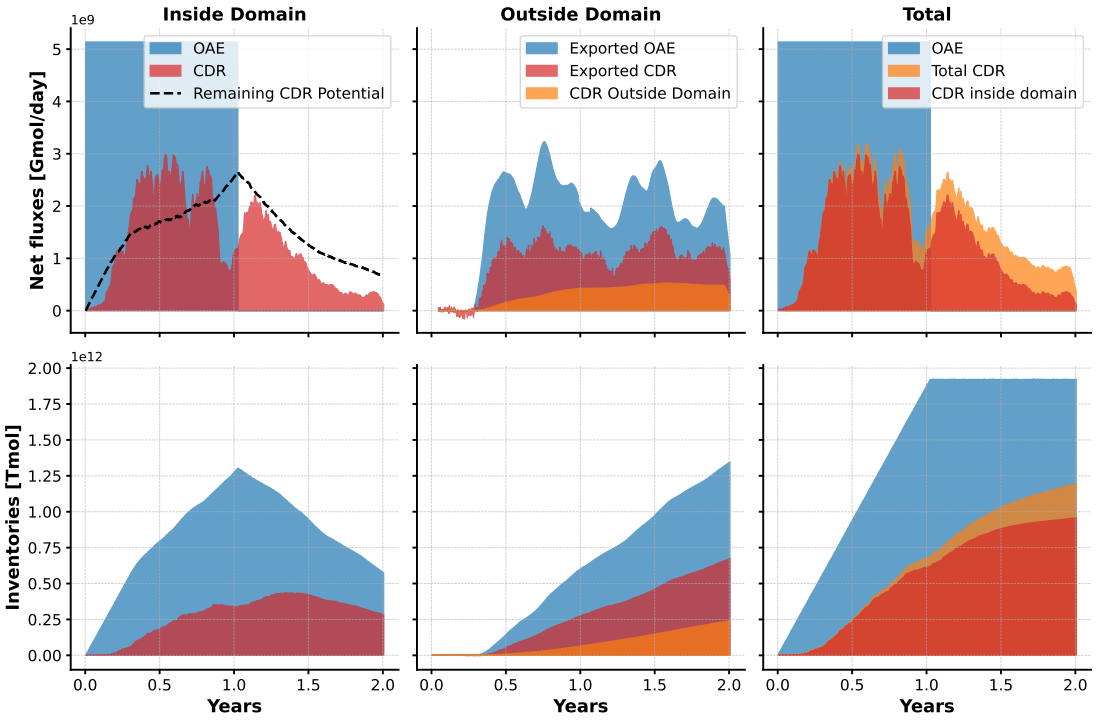

Figure B.1: Budget analysis of OAE intervention in the California Current System. The top row shows net fluxes of alkalinity, CO_2 uptake, and unreacted alkalinity inside, outside, and across the total system. The bottom row shows cumulative inventories of alkalinity and DIC, highlighting retained and exported fractions.

B.2 Isotope-Enabled Box Model

To better understand isotopic processes relevant to Chapter 3, we developed an isotope-enabled box model with the capabilities to simulate different mCDR methods. This model simulates a generic water column with a mixed layer depth of 30 m and a surface area of 1 m^2 and a fixed atmospheric pCO_2 of 395 μatm with a $\delta^{13}C$ of -8‰ (adjustable

in the `constants.py` file). The model tracks key state variables, including dissolved inorganic carbon (DIC), alkalinity (ALK), δ^{13}C-DIC, and Δ^{14}C-DIC, under various forcing conditions. The model builds on the foundational work of Lynch-Stieglitz et al. (1995) and Cai et al. (2020).

Forcings

The following forcings are applied to the model to simulate realistic oceanic conditions:

- **Temperature and Salinity**: Derived from the Mercator 1/12° data-assimilated General Circulation Model, provided at daily resolution.
- **Wind Speed**: Prescribed seasonally: 7 m/s from March through September and 10.5 m/s from October through February.
- **Net Community Production (NCP)**: Derived from weekly averages of daily changes in satellite-derived chlorophyll (Chl) for the year 2015 using the daily MODIS Aqua 4 km Level 3 product. The NCP values are interpolated to daily time series, with a maximum NCP of ∼0.1 mmol C day^{-1} m^{-3}. More details can be found in Cai et al. (2020).
- **Vertical Mixing**: Vertical mixing during winter months (October through February) is simulated based on a fixed mixing flux of 0.1 mmol m^{-3} day^{-1} (Cai et al., 2020). The mixing flux is converted to a unitless daily mixing rate by dividing by the current surface DIC concentration. This rate determines the flux of tracers (DIC, ALK, δ^{13}C, and Δ^{14}C) between the subsurface (DIC = 2200 μmol kg^{-1}, ALK = 2400 μmol kg^{-1}, δ^{13}C = 1‰, Δ^{14}C = -100‰) and surface layers. No mixing occurs during summer (March through September).

Isotopic Fractionation During Biology

Biological processes influence the carbon isotopic composition of the ocean (Fontugne & Duplessy, 1978). During photosynthesis, organisms preferentially utilize ^{12}C (the lighter carbon isotope), enriching the surface ocean in ^{13}C and relatively enriching the underlying waters in ^{12}C upon remineralization. A constant isotopic fractionation of

-22‰ for photosynthesis (Toggweiler & Sarmiento, 1985; Vogel et al., 1970) is used, and a small fractionation of +2‰ for calcium carbonate formation is applied, following Jahn et al. (2015).

Isotopic Fractionation During Air-Sea Gas Exchange

The kinetic fractionation factor (α_k) for CO_2 transfer across the air-sea interface is set to 0.9995 (Siegenthaler & Miinnich, 1981; Zhang & Quay, 1995). The equilibrium fractionation between atmospheric CO_2 and dissolved CO_2 in seawater is temperature-dependent, calculated using:

$$\alpha_{CO2} = -0.373/T_k + 1.00019$$

from Vogel et al. (1970). The overall fractionation factor for air-sea carbon transfer is $\alpha_k \times \alpha_{CO2}$.

Following Lynch-Stieglitz et al. (1995), the temperature-dependent equilibrium fractionation between dissolved CO_2 and DIC is approximated using:

$$\alpha_{HCO3} = -9.866/T_k + 1.02412.$$

The fractionation factor for sea-air carbon transfer is calculated as $\alpha_k \times \alpha_{HCO3}$. Fractionation factors (α) are converted to isotopic enrichment factors (ϵ) to align with delta notation (units per mil). For ^{14}C, all isotopic enrichment factors are doubled (Zeebe & Wolf-Gladrow, 2001).

Equilibrium Assumptions

Chemical and isotopic equilibrium occurs on timescales of seconds (Zeebe et al., 1999), much faster than the years to decades required for air-sea equilibrium of CO_2 and carbon isotopes (W. S. Broecker & Peng, 1982; Schmittner et al., 2013). Thus, the model assumes that carbon species in the mixed layer are in chemical and isotopic equilibrium for all timescales relevant to the experiments.

Model Initiation and Iteration

The model is spun up for 5 years to ensure a steady state of isotopic equilibrium with the atmosphere. It is initialized with a δ^{13}C-DIC of 1‰ and a Δ^{14}C-DIC of 0‰. Following Cai et al. (2020), the carbonate system is initialized with values calculated from PyCO2SYS (Humphreys et al., 2021) based on a $pCO_{2(aq)}$ in equilibrium with atmospheric values (395 μatm) and alkalinity calculated based on salinity. ΔDIC_{bio} and $\Delta DIC_{vertical}$ are prescribed as fractional changes (values mentioned above), while $\Delta pCO_{2air\text{-}sea}$ is calculated at each time step using the relationship:

$$\Delta pCO_{2air\text{-}sea} = 0.24 \cdot k \cdot K_0 \cdot (pCO_{2t(aq)} - pCO_{2atm}),$$

where K_0 is the CO_2 gas solubility (Weiss, 1974) and k is defined as $0.251 \cdot W^2 \cdot (Sc/660)^{-0.5}$, with W as wind speed in m/s and Sc as the Schmidt number (Wanninkhof, 1992, 2014). For $\Delta pCO_{2air\text{-}sea}$, $pCO_{2t(aq)}$ is calculated using an iterative CO_2 solver. At each time step, DIC_{t+1} is updated based on ΔDIC_{bio}, $\Delta DIC_{vertical}$, and $\Delta pCO_{2air\text{-}sea}$. At the end of the simulation, PyCO2SYS is used to back-calculate pCO_2, pH, and $\Omega_{aragonite}$ based on the model's DIC, ALK, and temperature and salinity forcing.

Running the Model

To run the model using `conda`, follow these steps:

1. Ensure `conda` or Anaconda is installed:

   If you don't have `conda` installed, you can download and install Miniconda or Anaconda.

2. Clone the repository:

   ```
   git clone https://github.com/RyanAGreen/mld-box-model-c-isotopes.git
   cd mld-box-model-c-isotopes
   ```

3. Create and activate a `conda` environment:

   ```
   conda env create -f environment.yaml
   conda activate mld-box-model
   ```

4. Adjust model parameters:

   You can modify the experiment length, mixed layer properties, atmospheric conditions, prescribed forcings, and other parameters within `src/utils/constants.py` as needed.

5. Run the model:

   ```
   python src/model.py
   ```

   Note that this will take a minute or two the first time the code is run. After that, each simulation should take only a few seconds (depending on the length of the experiment). An overview figure will be generated and saved as `model_results.png` in the `data/plots` directory. Additionally, a text file containing the model results will be saved as `model_results.txt` in the `data` directory for further analysis.

6. Deactivate the `conda` environment:

   ```
   conda deactivate
   ```

   Note: If you want to work on the model later, remember to reactivate the `conda` environment before running any code:

   ```
   conda activate mld-box-model
   ```

Code Structure

The table below explains the files and directories included in this project.

Directory/File	Description
`README.md`	Project documentation (this file).
`LICENSE`	License information.
`environment.yml`	Conda environment file for dependencies.
`data`	Directory for data used or generated by the model.
`src`	Source code for the model.
`src/model.py`	Main model code.
`src/utils`	Utility functions or modules.
`src/utils/constants.py`	Constants used in the model.
`src/utils/fluxes.py`	Flux calculations for the model.
`src/utils/data_input.py`	Data input functions.
`src/utils/data_output.py`	Data output functions.
`src/utils/plotting.py`	Plotting functions.
`src/utils/indata/mercator_tseries.h5`	Temperature, salinity, and net community production forcing data.
`src/__init__.py`	Python package initialization file.

Output

The model generates:

- **Overview Figure**: Saved in the `data/plots` directory. This figure shows the seasonal salinity and SST forcing, DIC and $\delta^{13}C$ model tracers, and pCO_2, pH, and Ω_{arag} generated with PyCO2SYS from the simulated DIC and ALK with the seasonal salinity and SST forcings. This figure is similar to Fig 6a,b,c from Cai et al. (2020).
- **Text File of Results**: Saved in the `data` directory. This contains the model tracers (DIC, alkalinity, $\delta^{13}C$, and $\Delta^{14}C$), salinity and SST forcing, and time in

units of years. Other carbonate parameters can be calculated from these DIC, alkalinity, salinity, and SST using PyCO2SYS/CO2SYS or another CO_2 solver.

Both outputs are designed for further data analysis and visualization.

Code Availability

The code is publicly available on GitHub, enabling transparency and reproducibility. Readers can access the code and documentation here: [https://github.com/RyanAGreen/mld-box-model-c-isotopes].

B.3 Simulating Direct Ocean Capture/Removal in ROMS

Overview and Rationale

In addition to Ocean Alkalinity Enhancement (OAE) experiments, we conducted simulations of Direct Ocean Capture (DOC) by removing dissolved inorganic carbon (DIC) directly from the surface ocean in ROMS. DOC is another promising method for marine carbon dioxide removal (mCDR) and has the potential to be highly effective (NASEM, 2021; NOAA, 2023). These experiments were conducted at the same location as the OAE simulations, allowing for direct comparison between the two methods.

Preliminary Findings

Preliminary analysis revealed that, as expected, the carbon removal efficiency of OAE was offset by approximately 0.2 compared to DOC simulations. Equilibrium timescales for achieving maximum efficiencies were similar between the two methods. These findings provide a foundation for future research, and we encourage graduate students or other researchers to build upon this work and further analyze these results.

Data Archiving and Accessibility

These simulation outputs are archived on the Storm server (`storm.pmc.ucsc.edu`) under the directory: `bigdata/wc15_dor_SF_0.4Tmol/out/....`

B.4 Offshore Deployment Simulations

Overview and Rationale

While early OAE deployments are likely to occur in near-coastal regions due to their proximity to infrastructure, energy supply, and human resources, future deployments may shift offshore. With large spatial variability in mCDR effectiveness (Zhou et al., 2024), comparing offshore and coastal deployment in high-resolution models is crucial to understanding optimal deployment locations moving forward.

Methodology and Deployment Details

For the offshore deployment simulation, we shifted the OAE location two degrees off the coast from the San Francisco deployment site used in other runs. This adjustment placed the deployment outside the upwelling zone, allowing us to investigate how differences in temperature and mixed layer depth might influence the residence time of alkalinity and, consequently, mCDR efficiency. While we have not yet analyzed this data, we encourage future students and researchers to explore these results.

Data Archiving and Accessibility

Simulation outputs are archived on the Storm server (`storm.pmc.ucsc.edu`) under the directory: `bigdata/wc15_oae_SF_offshore_0.4Tmol/out/...`.

Bibliography

Archer, D., Eby, M., Brovkin, V., Ridgwell, A., Cao, L., Mikolajewicz, U., Caldeira, K., Matsumoto, K., Munhoven, G., Montenegro, A., & Tokos, K. (2009). Atmospheric Lifetime of Fossil Fuel Carbon Dioxide. *Annual Review of Earth and Planetary Sciences*, *37*(1), 117–134. https://doi.org/10.1146/annurev.earth.031208.100206

Bach, L. T., & Boyd, P. W. (2021). Seeking natural analogs to fast-forward the assessment of marine CO2 removal. *Proceedings of the National Academy of Sciences*, *118*(40), e2106147118. https://doi.org/10.1073/pnas.2106147118

Bard, E. (1998). Geochemical and geophysical implications of the radiocarbon calibration. *Geochimica et Cosmochimica Acta*, *62*(12), 2025–2038. https://doi.org/10.1016/S0016-7037(98)00130-6

Barker, S., Greaves, M., & Elderfield, H. (2003). A study of cleaning procedures used for foraminiferal Mg/Ca paleothermometry. *Geochemistry, Geophysics, Geosystems*, *4*(9). https://doi.org/10.1029/2003GC000559

Becker, M., Andersen, N., Fiedler, B., Fietzek, P., Körtzinger, A., Steinhoff, T., & Friedrichs, G. (2012). Using cavity ringdown spectroscopy for continuous monitoring of 13C(CO2) and fCO2 in the surface ocean. *Limnology and Oceanography: Methods*, *10*(10), 752–766. https://doi.org/10.4319/lom.2012.10.752

Bereiter, B., Eggleston, S., Schmitt, J., Nehrbass-Ahles, C., Stocker, T. F., Fischer, H., Kipfstuhl, S., & Chappellaz, J. (2015). Revision of the EPICA Dome C CO2 record from 800 to 600 kyr before present. *Geophysical Research Letters*, *42*(2), 542–549. https://doi.org/10.1002/2014GL061957

Bolin, B. (1960). On the Exchange of Carbon Dioxide between the Atmosphere and the Sea. *Tellus*, *12*(3), 274–281. https://doi.org/10.3402/tellusa.v12i3.9402

Bova, S. C., Herbert, T. D., & Altabet, M. A. (2018). Ventilation of Northern and Southern Sources of Aged Carbon in the Eastern Equatorial Pacific During the Younger Dryas Rise in Atmospheric CO2. *Paleoceanography and Paleoclimatology*, *33*(11), 1151–1168. https://doi.org/10.1029/2018PA003386

Briggs, E. M., & Ringham, M. C. (2023, May). *Observing Marine Inorganic Carbon*. American Chemical Society. https://doi.org/10.1021/acsinfocus.7e7010

Broecker, W., & Barker, S. (2007). A 190‰ drop in atmosphere's 14C during the "Mystery Interval" (17.5 to 14.5 kyr). *Earth and Planetary Science Letters*, *256*(1-2), 90–99. https://doi.org/10.1016/j.epsl.2007.01.015

Broecker, W. S., & Peng, T.-H. (1974). Gas exchange rates between air and sea1. *Tellus*, *26*(1-2), 21–35. https://doi.org/10.3402/tellusa.v26i1-2.9733

Broecker, W. S., & Peng, T.-H. (1982). *Tracers in the Sea*. Lamont-Doherty Geological Observatory, Palisades, New York.

Broecker, W. (2009). The Mysterious 14C Decline. *Radiocarbon*, *51*(1), 109–119. https://doi.org/10.1017/S0033822200033737

Broecker, W., Barker, S., Clark, E., Hajdas, I., Bonani, G., & Stott, L. (2004). Ventilation of the Glacial Deep Pacific Ocean. *Science*, *306*(5699), 1169–1172. https://doi.org/10.1126/science.1102293

Broecker, W. S., & Maier-Reimer, E. (1992). The influence of air and sea exchange on the carbon isotope distribution in the sea. *Global Biogeochemical Cycles*, *6*(3), 315–320. https://doi.org/10.1029/92GB01672

Bryan, S. P., Marchitto, T. M., & Lehman, S. J. (2010). The release of 14C-depleted carbon from the deep ocean during the last deglaciation: Evidence from the Arabian Sea. *Earth and Planetary Science Letters*, *298*(1), 244–254. https://doi.org/10.1016/j.epsl.2010.08.025

Cai, W.-J., Xu, Y.-Y., Feely, R. A., Wanninkhof, R., Jönsson, B., Alin, S. R., Barbero, L., Cross, J. N., Azetsu-Scott, K., Fassbender, A. J., Carter, B. R., Jiang, L.-Q., Pepin, P., Chen, B., Hussain, N., Reimer, J. J., Xue, L., Salisbury, J. E., Hernández-Ayón, J. M., ... Gledhill, D. K. (2020). Controls on surface water carbonate chemistry along North American ocean margins. *Nature Communications*, *11*(1), 2691. https://doi.org/10.1038/s41467-020-16530-z

Cartapanis, O., Galbraith, E. D., Bianchi, D., & Jaccard, S. L. (2018). Carbon burial in deep-sea sediment and implications for oceanic inventories of carbon and alka-

linity over the last glacial cycle. *Climate of the Past*, *14*(11), 1819–1850. https://doi.org/10.5194/cp-14-1819-2018

Chalk, T. B., Hain, M. P., Foster, G. L., Rohling, E. J., Sexton, P. F., Badger, M. P. S., Cherry, S. G., Hasenfratz, A. P., Haug, G. H., Jaccard, S. L., Martínez-García, A., Pälike, H., Pancost, R. D., & Wilson, P. A. (2017). Causes of ice age intensification across the Mid-Pleistocene Transition. *Proceedings of the National Academy of Sciences*, *114*(50), 13114–13119. https://doi.org/10.1073/pnas.1702143114

Charles, C. D., Wright, J. D., & Fairbanks, R. G. (1993). Thermodynamic influences on the marine carbon isotope record. *Paleoceanography*, *8*(6), 691–697. https://doi.org/10.1029/93PA01803

Chen, T., Robinson, L. F., Burke, A., Claxton, L., Hain, M. P., Li, T., Rae, J. W. B., Stewart, J., Knowles, T. D. J., Fornari, D. J., & Harpp, K. S. (2020). Persistently well-ventilated intermediate-depth ocean through the last deglaciation. *Nature Geoscience*, *13*(11), 733–738. https://doi.org/10.1038/s41561-020-0638-6

Cook, M. S., & Keigwin, L. D. (2015). Radiocarbon profiles of the NW Pacific from the LGM and deglaciation: Evaluating ventilation metrics and the effect of uncertain surface reservoir ages. *Paleoceanography*, *30*(3), 174–195. https://doi.org/10.1002/2014PA002649

Cook, M. S., Keigwin, L. D., Birgel, D., & Hinrichs, K.-U. (2011). Repeated pulses of vertical methane flux recorded in glacial sediments from the southeast Bering Sea. *Paleoceanography*, *26*(2). https://doi.org/10.1029/2010PA001993

Craig, H. (1957). The Natural Distribution of Radiocarbon and the Exchange Time of Carbon Dioxide Between Atmosphere and Sea. *Tellus*, *9*(1), 1–17. https://doi.org/10.3402/tellusa.v9i1.9078

De Pol-Holz, R., Keigwin, L., Southon, J., Hebbeln, D., & Mohtadi, M. (2010). No signature of abyssal carbon in intermediate waters off Chile during deglaciation. *Nature Geoscience*, *3*(3), 192–195. https://doi.org/10.1038/ngeo745

Dickson, A. G., & Millero, F. J. (1987). A comparison of the equilibrium constants for the dissociation of carbonic acid in seawater media. *Deep Sea Research Part A. Oceanographic Research Papers*, *34*(10), 1733–1743. https://doi.org/10.1016/0198-0149(87)90021-5

Dickson, A. G. (1990). Thermodynamics of the dissociation of boric acid in synthetic seawater from 273.15 to 318.15 K. *Deep Sea Research Part A. Oceanographic*

Research Papers, *37*(5), 755–766. https://doi.org/10.1016/0198-0149(90)90004-F

Dinauer, A., Adolphi, F., & Joos, F. (2020). Mysteriously high 14C of the glacial atmosphere: Influence of 14C production and carbon cycle changes. *Climate of the Past*, *16*(4), 1159–1185. https://doi.org/10.5194/cp-16-1159-2020

Drake, P. T., Edwards, C. A., & Barth, J. A. (2011). Dispersion and connectivity estimates along the U.S. west coast from a realistic numerical model. *Journal of Marine Research*, *69*(1), 1–37. https://doi.org/10.1357/002224011798147615

Dubinina, E. O., Kossova, S. A., & Chizhova, Y. N. (2024). High-Precision Determination of Carbon Isotope Composition and Concentration of Dissolved Inorganic Carbon in Seawater. *Geochemistry International*, *62*(1), 45–54. https://doi.org/10.1134/S0016702924010038

Feng, E. Y., Koeve, W., Keller, D. P., & Oschlies, A. (2017). Model-Based Assessment of the CO2 Sequestration Potential of Coastal Ocean Alkalinization. *Earth's Future*, *5*(12), 1252–1266. https://doi.org/10.1002/2017EF000659

Fiechter, J., Curchitser, E. N., Edwards, C. A., Chai, F., Goebel, N. L., & Chavez, F. P. (2014). Air-sea CO2 fluxes in the California Current: Impacts of model resolution and coastal topography. *Global Biogeochemical Cycles*, *28*(4), 371–385. https://doi.org/10.1002/2013GB004683

Fine, R. A., Maillet, K. A., Sullivan, K. F., & Willey, D. (2001). Circulation and ventilation flux of the Pacific Ocean. *Journal of Geophysical Research: Oceans*, *106*(C10), 22159–22178. https://doi.org/10.1029/1999JC000184

Flude, S., Györe, D., Stuart, F. M., Zurakowska, M., Boyce, A. J., Haszeldine, R. S., Chalaturnyk, R., & Gilfillan, S. M. V. (2017). The inherent tracer fingerprint of captured CO2. *International Journal of Greenhouse Gas Control*, *65*, 40–54. https://doi.org/10.1016/j.ijggc.2017.08.010

Fontugne, M., & Duplessy, J. C. (1978). Carbon isotope ratio of marine plankton related to surface water masses. *Earth and Planetary Science Letters*, *41*(3), 365–371. https://doi.org/10.1016/0012-821X(78)90191-7

Foster, G. L. (2008). Seawater pH, pCO2 and [CO2- 3] variations in the Caribbean Sea over the last 130 kyr: A boron isotope and B/Ca study of planktic foraminifera. *Earth and Planetary Science Letters*, *271*(1-4), 254–266.

Foster, G. L., Hönisch, B., Paris, G., Dwyer, G. S., Rae, J. W., Elliott, T., Gaillardet, J., Hemming, N. G., Louvat, P., & Vengosh, A. (2013). Interlaboratory comparison of boron isotope analyses of boric acid, seawater and marine CaCO3 by MC-ICPMS and NTIMS. *Chemical Geology*, *358*, 1–14.

Friedlingstein, P., O'Sullivan, M., Jones, M. W., Andrew, R. M., Gregor, L., Hauck, J., Le Quéré, C., Luijkx, I. T., Olsen, A., Peters, G. P., Peters, W., Pongratz, J., Schwingshackl, C., Sitch, S., Canadell, J. G., Ciais, P., Jackson, R. B., Alin, S. R., Alkama, R., ... Zheng, B. (2022). Global Carbon Budget 2022. *Earth System Science Data*, *14*(11), 4811–4900. https://doi.org/10.5194/essd-14-4811-2022

Friedrichs, G., Bock, J., Temps, F., Fietzek, P., Körtzinger, A., & Wallace, D. W. R. (2010). Toward continuous monitoring of seawater 13CO2/12CO2 isotope ratio and pCO2: Performance of cavity ringdown spectroscopy and gas matrix effects. *Limnology and Oceanography: Methods*, *8*(10), 539–551. https://doi.org/10.4319/lom.2010.8.539

Galbraith, E. D., Kwon, E. Y., Bianchi, D., Hain, M. P., & Sarmiento, J. L. (2015). The impact of atmospheric pCO2 on carbon isotope ratios of the atmosphere and ocean. *Global Biogeochemical Cycles*, *29*(3), 307–324. https://doi.org/https://doi.org/10.1002/2014GB004929

Ganeshram, R. S., & Pedersen, T. F. (1998). Glacial-interglacial variability in upwelling and bioproductivity off NW Mexico: Implications for Quaternary paleoclimate. *Paleoceanography*, *13*(6), 634–645. https://doi.org/10.1029/98PA02508

Gardner, J. V., Dean, W. E., & Dartnell, P. (1997). Biogenic sedimentation beneath the California Current System for the past 30 kyr and its paleoceanographic significance. *Paleoceanography*, *12*(2), 207–225. https://doi.org/10.1029/96PA03567

Gehrie, E., Archer, D., Emerson, S., Stump, C., & Henning, C. (2006). Subsurface ocean argon disequilibrium reveals the equatorial Pacific shadow zone. *Geophysical Research Letters*, *33*(18). https://doi.org/10.1029/2006GL026935

Gómez-Valdivia, F., Parés-Sierra, A., & Flores-Morales, A. L. (2015). The Mexican Coastal Current: A subsurface seasonal bridge that connects the tropical and subtropical Northeastern Pacific. *Continental Shelf Research*, *110*, 100–107. https://doi.org/10.1016/j.csr.2015.10.010

Graven, H., Keeling, R. F., & Rogelj, J. (2020). Changes to Carbon Isotopes in Atmospheric CO2 Over the Industrial Era and Into the Future. *Global Biogeochemical Cycles*, *34*(11), e2019GB006170. https://doi.org/10.1029/2019GB006170

Green, R. A., Hain, M. P., & Rafter, P. A. (2024). Deglacial Pulse of Neutralized Carbon From the Pacific Seafloor: A Natural Analog for Ocean Alkalinity Enhancement? *Geophysical Research Letters*, *51*(8), e2024GL108271. https://doi.org/10.1029/2024GL108271

Gruber, N., Keeling, C. D., & Bates, N. R. (2002). Interannual Variability in the North Atlantic Ocean Carbon Sink. *Science*, *298*(5602), 2374–2378. https://doi.org/10.1126/science.1077077

Haidvogel, D. B., Arango, H., Budgell, W. P., Cornuelle, B. D., Curchitser, E., Di Lorenzo, E., Fennel, K., Geyer, W. R., Hermann, A. J., Lanerolle, L., Levin, J., McWilliams, J. C., Miller, A. J., Moore, A. M., Powell, T. M., Shchepetkin, A. F., Sherwood, C. R., Signell, R. P., Warner, J. C., & Wilkin, J. (2008). Ocean forecasting in terrain-following coordinates: Formulation and skill assessment of the Regional Ocean Modeling System. *Journal of Computational Physics*, *227*(7), 3595–3624. https://doi.org/10.1016/j.jcp.2007.06.016

Hain, M. P., Foster, G. L., & Chalk, T. (2018). Robust Constraints on Past CO2 Climate Forcing From the Boron Isotope Proxy. *Paleoceanography and Paleoclimatology*, *33*(10), 1099–1115. https://doi.org/https://doi.org/10.1029/2018PA003362

Hain, M. P., Sigman, D. M., & Haug, G. H. (2010). Carbon dioxide effects of Antarctic stratification, North Atlantic Intermediate Water formation, and subantarctic nutrient drawdown during the last ice age: Diagnosis and synthesis in a geochemical box model. *Global Biogeochemical Cycles*, *24*(4), n/a–n/a. https://doi.org/10.1029/2010GB003790

Hain, M. P., Sigman, D. M., & Haug, G. H. (2011). Shortcomings of the isolated abyssal reservoir model for deglacial radiocarbon changes in the mid-depth Indo-Pacific Ocean. *Geophysical Research Letters*, *38*(4). https://doi.org/10.1029/2010GL046158

Hain, M. P., Sigman, D. M., & Haug, G. H. (2014). Distinct roles of the Southern Ocean and North Atlantic in the deglacial atmospheric radiocarbon decline. *Earth and Planetary Science Letters*, *394*, 198–208. https://doi.org/10.1016/j.epsl.2014.03.020

Hain, M. P., Sigman, D. M., Higgins, J. A., & Haug, G. H. (2015). The effects of secular calcium and magnesium concentration changes on the thermodynamics of seawater acid/base chemistry: Implications for Eocene and Cretaceous ocean carbon chemistry and buffering. *Global Biogeochemical Cycles*, *29*(5), 517–533. https://doi.org/https://doi.org/10.1002/2014GB004986

He, J., & Tyka, M. D. (2023). Limits and CO2 equilibration of near-coast alkalinity enhancement. *Biogeosciences*, *20*(1), 27–43. https://doi.org/10.5194/bg-20-27-2023

Hersbach, H., Bell, B., Berrisford, P., Hirahara, S., Horányi, A., Muñoz-Sabater, J., Nicolas, J., Peubey, C., Radu, R., Schepers, D., Simmons, A., Soci, C., Abdalla, S., Abellan, X., Balsamo, G., Bechtold, P., Biavati, G., Bidlot, J., Bonavita, M., ... Thépaut, J.-N. (2020). The ERA5 global reanalysis. *Quarterly Journal of the Royal Meteorological Society*, *146*(730), 1999–2049. https://doi.org/10.1002/qj.3803

Ho, D. T., Bopp, L., Palter, J. B., Long, M. C., Boyd, P., Neukermans, G., & Bach, L. (2023, June). *Chapter 6: Monitoring, Reporting, and Verification for Ocean Alkalinity Enhancement* (preprint). https://doi.org/10.5194/sp-2023-2

Hodell, D. A., Venz, K. A., Charles, C. D., & Ninnemann, U. S. (2003). Pleistocene vertical carbon isotope and carbonate gradients in the South Atlantic sector of the Southern Ocean. *Geochemistry, Geophysics, Geosystems*, *4*(1), 1–19. https://doi.org/10.1029/2002GC000367

Holzer, M., DeVries, T., & de Lavergne, C. (2021). Diffusion controls the ventilation of a Pacific Shadow Zone above abyssal overturning. *Nature Communications*, *12*(1), 4348. https://doi.org/10.1038/s41467-021-24648-x

Humphreys, M. P., Lewis, E. R., Sharp, J. D., & Pierrot, D. (2021, June). *PyCO2SYS v1.7: Marine carbonate system calculations in Python* (preprint). Oceanography. https://doi.org/10.5194/gmd-2021-159

Huybers, P., & Langmuir, C. (2009). Feedback between deglaciation, volcanism, and atmospheric CO2. *Earth and Planetary Science Letters*, *286*(3), 479–491. https://doi.org/10.1016/j.epsl.2009.07.014

Ito, T., & Follows, M. J. (2005). Preformed phosphate, soft tissue pump and atmospheric CO2. *Journal of Marine Research*, *63*(4), 813–839. https://doi.org/10.1357/0022240054663231

Jahn, A., Lindsay, K., Giraud, X., Gruber, N., Otto-Bliesner, B. L., Liu, Z., & Brady, E. C. (2015). Carbon isotopes in the ocean model of the Community Earth System Model (CESM1). *Geoscientific Model Development*, *8*(8), 2419–2434. https://doi.org/10.5194/gmd-8-2419-2015

Jean-Michel, L., Eric, G., Romain, B.-B., Gilles, G., Angélique, M., Marie, D., Clément, B., Mathieu, H., Olivier, L. G., Charly, R., Tony, C., Charles-Emmanuel, T., Florent, G., Giovanni, R., Mounir, B., Yann, D., & Pierre-Yves, L. T. (2021). The Copernicus Global 1/12° Oceanic and Sea Ice GLORYS12 Reanalysis. *Frontiers in Earth Science*, *9*. https://doi.org/10.3389/feart.2021.698876

Jones, D. C., Ito, T., Takano, Y., & Hsu, W.-C. (2014). Spatial and seasonal variability of the air-sea equilibration timescale of carbon dioxide. *Global Biogeochemical Cycles*, *28*(11), 1163–1178. https://doi.org/10.1002/2014GB004813

Joos, F., Prentice, I. C., Sitch, S., Meyer, R., Hooss, G., Plattner, G.-K., Gerber, S., & Hasselmann, K. (2001). Global warming feedbacks on terrestrial carbon uptake under the Intergovernmental Panel on Climate Change (IPCC) Emission Scenarios. *Global Biogeochemical Cycles*, *15*(4), 891–907. https://doi.org/10.1029/2000GB001375

Karlen, I., Olsson, I. U., Kallberg, P., & Kilicci, S. (1965). ABSOLUTE DETERMINATION OF THE ACTIVITY OF TWO C-14 DATING STANDARDS. *Arkiv Geofysik.*, *Vol: 4*.

Keeling, C. D. (1979). The Suess effect: 13Carbon-14Carbon interrelations. *Environment International*, *2*(4), 229–300. https://doi.org/10.1016/0160-4120(79)90005-9

Keigwin, L. D., & Jones, G. A. (1990). Deglacial climatic oscillations in the Gulf of California. *Paleoceanography*, *5*(6), 1009–1023. https://doi.org/10.1029/PA005i006p01009

Keir, R. S. (1988). On the Late Pleistocene ocean geochemistry and circulation. *Paleoceanography*, *3*(4), 413–445. https://doi.org/https://doi.org/10.1029/PA003i004p00413

Khatiwala, S., Schmittner, A., & Muglia, J. (2019). Air-sea disequilibrium enhances ocean carbon storage during glacial periods. *Science Advances*, *5*(6), eaaw4981. https://doi.org/10.1126/sciadv.aaw4981

Kishi, M. J., Kashiwai, M., Ware, D. M., Megrey, B. A., Eslinger, D. L., Werner, F. E., Noguchi-Aita, M., Azumaya, T., Fujii, M., Hashimoto, S., Huang, D., Iizumi, H., Ishida, Y., Kang, S., Kantakov, G. A., Kim, H.-c., Komatsu, K., Navrotsky,

V. V., Smith, S. L., ... Zvalinsky, V. I. (2007). NEMURO—a lower trophic level model for the North Pacific marine ecosystem. *Ecological Modelling*, *202*(1), 12–25. https://doi.org/10.1016/j.ecolmodel.2006.08.021

Köhler, P., Abrams, J. F., Völker, C., Hauck, J., & Wolf-Gladrow, D. A. (2013). Geoengineering impact of open ocean dissolution of olivine on atmospheric CO 2 , surface ocean pH and marine biology. *Environmental Research Letters*, *8*(1), 014009. https://doi.org/10.1088/1748-9326/8/1/014009

Köhler, P., Knorr, G., & Bard, E. (2014). Permafrost thawing as a possible source of abrupt carbon release at the onset of the Bølling/Allerød. *Nature Communications*, *5*(1), 5520. https://doi.org/10.1038/ncomms6520

Kovaltsov, G. A., Mishev, A., & Usoskin, I. G. (2012). A new model of cosmogenic production of radiocarbon 14C in the atmosphere. *Earth and Planetary Science Letters*, *337-338*, 114–120. https://doi.org/10.1016/j.epsl.2012.05.036

Laj, C., Kissel, C., & Beer, J. (2004). High Resolution Global Paleointensity Stack Since 75 kyr (GLOPIS-75) Calibrated to Absolute Values. In *Timescales Of The Paleomagnetic Field* (pp. 255–265). American Geophysical Union (AGU). https://doi.org/10.1029/145GM19

Lauvset, S. K., Lange, N., Tanhua, T., Bittig, H. C., Olsen, A., Kozyr, A., Álvarez, M., Azetsu-Scott, K., Brown, P. J., Carter, B. R., Cotrim da Cunha, L., Hoppema, M., Humphreys, M. P., Ishii, M., Jeansson, E., Murata, A., Müller, J. D., Pérez, F. F., Schirnick, C., ... Key, R. M. (2024). The annual update GLODAPv2.2023: The global interior ocean biogeochemical data product. *Earth System Science Data*, *16*(4), 2047–2072. https://doi.org/10.5194/essd-16-2047-2024

Lavín, M. F., & Marinone, S. G. (2003). An Overview of the Physical Oceanography of the Gulf of California. In O. U. Velasco Fuentes, J. Sheinbaum, & J. Ochoa (Eds.), *Nonlinear Processes in Geophysical Fluid Dynamics: A tribute to the scientific work of Pedro Ripa* (pp. 173–204). Springer Netherlands. https://doi.org/10.1007/978-94-010-0074-1_11

Lee, H., Calvin, K., Dasgupta, D., Krinner, G., Mukherji, A., Thorne, P., Trisos, C., Romero, J., Aldunce, P., & Barret, K. (2023). IPCC, 2023: Climate Change 2023: Synthesis Report, Summary for Policymakers. Contribution of Working Groups I, II and III to the Sixth Assessment Report of the Intergovernmental

Panel on Climate Change [Core Writing Team, H. Lee and J. Romero (eds.)]. IPCC, Geneva, Switzerland.

Lindsay, C. M., Lehman, S. J., Marchitto, T. M., Carriquiry, J. D., & Ortiz, J. D. (2016). New constraints on deglacial marine radiocarbon anomalies from a depth transect near Baja California. *Paleoceanography*, *31*(8), 1103–1116. https://doi.org/10.1002/2015PA002878

Lindsay, C. M., Lehman, S. J., Marchitto, T. M., & Ortiz, J. D. (2015). The surface expression of radiocarbon anomalies near Baja California during deglaciation. *Earth and Planetary Science Letters*, *422*, 67–74. https://doi.org/10.1016/j.epsl.2015.04.012

Lord, N. S., Ridgwell, A., Thorne, M. C., & Lunt, D. J. (2016). An impulse response function for the "long tail" of excess atmospheric CO2 in an Earth system model. *Global Biogeochemical Cycles*, *30*(1), 2–17. https://doi.org/10.1002/2014GB005074

Lund, D. C., Asimow, P. D., Farley, K. A., Rooney, T. O., Seeley, E., Jackson, E. W., & Durham, Z. M. (2016). Enhanced East Pacific Rise hydrothermal activity during the last two glacial terminations. *Science*, *351*(6272), 478–482. https://doi.org/10.1126/science.aad4296

Lund, D. C., & Asimow, P. D. (2011). Does sea level influence mid-ocean ridge magmatism on Milankovitch timescales? *Geochemistry, Geophysics, Geosystems*, *12*(12). https://doi.org/10.1029/2011GC003693

Lund, D. C., Pavia, F. J., Seeley, E. I., McCart, S. E., Rafter, P. A., Farley, K. A., Asimow, P. D., & Anderson, R. F. (2019). Hydrothermal scavenging of 230Th on the Southern East Pacific Rise during the last deglaciation. *Earth and Planetary Science Letters*, *510*, 64–72. https://doi.org/10.1016/j.epsl.2018.12.037

Lynch-Stieglitz, J., Stocker, T. F., Broecker, W. S., & Fairbanks, R. G. (1995). The influence of air-sea exchange on the isotopic composition of oceanic carbon: Observations and modeling. *Global Biogeochemical Cycles*, *9*(4), 653–665. https://doi.org/10.1029/95GB02574

Mackensen, A., & Schmiedl, G. (2019). Stable carbon isotopes in paleoceanography: Atmosphere, oceans, and sediments. *Earth-Science Reviews*, *197*, 102893. https://doi.org/10.1016/j.earscirev.2019.102893

Maher, D. T., Cowley, K., Santos, I. R., Macklin, P., & Eyre, B. D. (2015). Methane and carbon dioxide dynamics in a subtropical estuary over a diel cycle: Insights

from automated in situ radioactive and stable isotope measurements. *Marine Chemistry*, *168*, 69–79. https://doi.org/10.1016/j.marchem.2014.10.017

Marchitto, T. M., Lehman, S. J., Ortiz, J. D., Flückiger, J., & Van Geen, A. (2007). Marine Radiocarbon Evidence for the Mechanism of Deglacial Atmospheric CO2 Rise. *Science*, *316*(5830), 1456–1459. https://doi.org/10.1126/science.1138679

Marcott, S. A., Bauska, T. K., Buizert, C., Steig, E. J., Rosen, J. L., Cuffey, K. M., Fudge, T. J., Severinghaus, J. P., Ahn, J., Kalk, M. L., McConnell, J. R., Sowers, T., Taylor, K. C., White, J. W. C., & Brook, E. J. (2014). Centennial-scale changes in the global carbon cycle during the last deglaciation. *Nature*, *514*(7524), 616–619. https://doi.org/10.1038/nature13799

Margolskee, A., Frenzel, H., Emerson, S., & Deutsch, C. (2019). Ventilation Pathways for the North Pacific Oxygen Deficient Zone. *Global Biogeochemical Cycles*, *33*(7), 875–890. https://doi.org/10.1029/2018GB006149

Marinov, I., Follows, M., Gnanadesikan, A., Sarmiento, J. L., & Slater, R. D. (2008). How does ocean biology affect atmospheric pCO2? Theory and models. *Journal of Geophysical Research: Oceans*, *113*(C7). https://doi.org/10.1029/2007JC004598

Marinov, I., Gnanadesikan, A., Sarmiento, J. L., Toggweiler, J. R., Follows, M., & Mignone, B. K. (2008). Impact of oceanic circulation on biological carbon storage in the ocean and atmospheric pCO2. *Global Biogeochemical Cycles*, *22*(3). https://doi.org/10.1029/2007GB002958

Masson-Delmotte, V. P., Zhai, P., Pirani, S. L., Connors, C., Péan, S., Berger, N., Caud, Y., Chen, L., Goldfarb, M. I., & Scheel Monteiro, P. M. (2021). Ipcc, 2021: Summary for policymakers. in: Climate change 2021: The physical science basis. contribution of working group i to the sixth assessment report of the intergovernmental panel on climate change.

McManus, J. F., Francois, R., Gherardi, J.-M., Keigwin, L. D., & Brown-Leger, S. (2004). Collapse and rapid resumption of Atlantic meridional circulation linked to deglacial climate changes. *Nature*, *428*(6985), 834–837. https://doi.org/10.1038/nature02494

Mehrbach, C., Culberson, C. H., Hawley, J. E., & Pytkowicx, R. M. (1973). Measurement of the Apparent Dissociation Constants of Carbonic Acid in Seawater at Atmospheric Pressure. *Limnology and Oceanography*, *18*(6), 897–907. https://doi.org/10.4319/lo.1973.18.6.0897

Millero, F. J. (1995). Thermodynamics of the carbon dioxide system in the oceans. *Geochimica et Cosmochimica Acta*, *59*(4), 661–677. https://doi.org/10.1016/0016-7037(94)00354-O

Mongin, M., Baird, M. E., Lenton, A., Neill, C., & Akl, J. (2021). Reversing ocean acidification along the Great Barrier Reef using alkalinity injection. *Environmental Research Letters*, *16*(6), 064068. https://doi.org/10.1088/1748-9326/ac002d

Mook, W., Bommerson, J., & Staverman, W. (1974). Carbon isotope fractionation between dissolved bicarbonate and gaseous carbon dioxide. *Earth and Planetary Science Letters*, *22*(2), 169–176. https://doi.org/10.1016/0012-821X(74)90078-8

Mu, L., Palter, J. B., & Wang, H. (2023). Considerations for hypothetical carbon dioxide removal via alkalinity addition in the Amazon River watershed. *Biogeosciences*, *20*(10), 1963–1977. https://doi.org/10.5194/bg-20-1963-2023

Mucci, A. (1983). The solubility of calcite and aragonite in seawater at various salinities, temperatures, and one atmosphere total pressure. *American Journal of Science*, *283*(7), 780–799. https://doi.org/10.2475/ajs.283.7.780

NASEM. (2021). *A Research Strategy for Ocean-based Carbon Dioxide Removal and Sequestration*. National Academies Press. https://doi.org/10.17226/26278

Nix, R. K. (2013). The Gulf of California. *A physical, geological and biological study. University of Texas, Dallas.*

NOAA. (2023). Strategy for NOAA Carbon Dioxide Removal Research.

Orr, J. C., Najjar, R. G., Aumont, O., Bopp, L., Bullister, J. L., Danabasoglu, G., Doney, S. C., Dunne, J. P., Dutay, J.-C., Graven, H., Griffies, S. M., John, J. G., Joos, F., Levin, I., Lindsay, K., Matear, R. J., McKinley, G. A., Mouchet, A., Oschlies, A., ... Yool, A. (2017). Biogeochemical protocols and diagnostics for the CMIP6 Ocean Model Intercomparison Project (OMIP). *Geoscientific Model Development*, *10*(6), 2169–2199. https://doi.org/10.5194/gmd-10-2169-2017

Ortiz, J., O'Connell, S., DelViscio, J., Dean, W., Carriquiry, J., Marchitto, T., Zheng, Y., & Van Geen, A. (2004). Enhanced marine productivity off western North America during warm climate intervals of the past 52 k.y. *Geology*, *32*(6), 521. https://doi.org/10.1130/G20234.1

Oschlies, A., Stevenson, A., Bach, L. T., Fennel, K., Rickaby, R. E. M., Satterfield, T., Webb, R., & Gattuso, J.-P. (2023, November). *Guide to Best Practices in*

Ocean Alkalinity Enhancement Research (tech. rep.). Copernicus GmbH. https://doi.org/10.5194/sp-2-oae2023

Paduan, J. B., Zierenberg, R. A., Clague, D. A., Spelz, R. M., Caress, D. W., Troni, G., Thomas, H., Glessner, J., Lilley, M. D., Lorenson, T., Lupton, J., Neumann, F., Santa Rosa-del Rio, M. A., & Wheat, C. G. (2018). Discovery of Hydrothermal Vent Fields on Alarcón Rise and in Southern Pescadero Basin, Gulf of California. *Geochemistry, Geophysics, Geosystems*, *19*(12), 4788–4819. https://doi.org/10.1029/2018GC007771

Poggemann, D.-W., Nürnberg, D., Hathorne, E. C., Frank, M., Rath, W., Reißig, S., & Bahr, A. (2018). Deglacial Heat Uptake by the Southern Ocean and Rapid Northward Redistribution Via Antarctic Intermediate Water. *Paleoceanography and Paleoclimatology*, *33*(11), 1292–1305. https://doi.org/10.1029/2017PA003284

Pollack, H. N., Hurter, S. J., & Johnson, J. R. (1993). Heat flow from the Earth's interior: Analysis of the global data set. *Reviews of Geophysics*, *31*(3), 267–280. https://doi.org/10.1029/93RG01249

Popp, B. N., Laws, E. A., Bidigare, R. R., Dore, J. E., Hanson, K. L., & Wakeham, S. G. (1998). Effect of Phytoplankton Cell Geometry on Carbon Isotopic Fractionation. *Geochimica et Cosmochimica Acta*, *62*(1), 69–77. https://doi.org/10.1016/S0016-7037(97)00333-5

Press, W. H., Teukolsky, S. A., Vetterling, W. T., & Flannery, B. P. (2007, September). *Numerical Recipes 3rd Edition: The Art of Scientific Computing*. Cambridge University Press.

Quay, P., Sonnerup, R., Munro, D., & Sweeney, C. (2017). Anthropogenic CO2 accumulation and uptake rates in the Pacific Ocean based on changes in the 13C/12C of dissolved inorganic carbon. *Global Biogeochemical Cycles*, *31*(1), 59–80. https://doi.org/10.1002/2016GB005460

Quay, P., Sonnerup, R., Stutsman, J., Maurer, J., Körtzinger, A., Padin, X. A., & Robinson, C. (2007). Anthropogenic CO2 accumulation rates in the North Atlantic Ocean from changes in the 13C/12C of dissolved inorganic carbon. *Global Biogeochemical Cycles*, *21*(1). https://doi.org/10.1029/2006GB002761

Quay, P., Sonnerup, R., Westby, T., Stutsman, J., & McNichol, A. (2003). Changes in the 13C/12C of dissolved inorganic carbon in the ocean as a tracer of anthropogenic

CO2 uptake. *Global Biogeochemical Cycles*, *17*(1), 4–1–4–20. https://doi.org/10.1029/2001GB001817

Quay, P. D., Tilbrook, B., & Wong, C. S. (1992). Oceanic Uptake of Fossil Fuel CO$_2$: Carbon- 13 Evidence. *Science*, *256*(5053), 74–79.

Quay, P., & Stutsman, J. (2003). Surface layer carbon budget for the subtropical N. Pacific: 13C<math><mtext></mtext><msup><mi></mi><mn>13</mn></msup><mtext>C<
constraints at station ALOHA. *Deep Sea Research Part I: Oceanographic Research Papers*, *50*(9), 1045–1061. https://doi.org/10.1016/S0967-0637(03)00116-X

Rae, J. W. B. (2018). Boron Isotopes in Foraminifera: Systematics, Biomineralisation, and CO2 Reconstruction. In H. Marschall & G. Foster (Eds.), *Boron Isotopes* (pp. 107–143). Springer International Publishing. https://doi.org/10.1007/978-3-319-64666-4_5

Rae, J. W., Foster, G. L., Schmidt, D. N., & Elliott, T. (2011). Boron isotopes and B/Ca in benthic foraminifera: Proxies for the deep ocean carbonate system. *Earth and Planetary Science Letters*, *302*(3-4), 403–413. https://doi.org/10.1016/j.epsl.2010.12.034

Rafter, P. A., Carriquiry, J. D., Herguera, J.-C., Hain, M. P., Solomon, E. A., & Southon, J. R. (2019). Anomalous > 2000-Year-Old Surface Ocean Radiocarbon Age as Evidence for Deglacial Geologic Carbon Release. *Geophysical Research Letters*, *46*(23), 13950–13960. https://doi.org/10.1029/2019GL085102

Rafter, P. A., Gray, W. R., Hines, S. K., Burke, A., Costa, K. M., Gottschalk, J., Hain, M. P., Rae, J. W., Southon, J. R., Walczak, M. H., Yu, J., Adkins, J. F., & DeVries, T. (2022). Global reorganization of deep-sea circulation and carbon storage after the last ice age. *Science Advances*, *8*(46), eabq5434. https://doi.org/10.1126/sciadv.abq5434

Rafter, P. A., Herguera, J.-C., & Southon, J. R. (2018). Extreme lowering of deglacial seawater radiocarbon recorded by both epifaunal and infaunal benthic foraminifera in a wood-dated sediment core. *Climate of the Past*, *14*(12), 1977–1989. https://doi.org/10.5194/cp-14-1977-2018

Reimer, P. J., Austin, W. E. N., Bard, E., Bayliss, A., Blackwell, P. G., Ramsey, C. B., Butzin, M., Cheng, H., Edwards, R. L., Friedrich, M., Grootes, P. M., Guilderson, T. P., Hajdas, I., Heaton, T. J., Hogg, A. G., Hughen, K. A., Kromer, B.,

Manning, S. W., Muscheler, R., ... Talamo, S. (2020). The IntCal20 Northern Hemisphere Radiocarbon Age Calibration Curve (0–55 cal kBP). *Radiocarbon*, *62*(4), 725–757. https://doi.org/10.1017/RDC.2020.41

Reimer, P. J., Bard, E., Bayliss, A., Beck, J. W., Blackwell, P. G., Ramsey, C. B., Buck, C. E., Cheng, H., Edwards, R. L., Friedrich, M., Grootes, P. M., Guilderson, T. P., Haflidason, H., Hajdas, I., Hatté, C., Heaton, T. J., Hoffmann, D. L., Hogg, A. G., Hughen, K. A., ... Plicht, J. v. d. (2013). IntCal13 and Marine13 Radiocarbon Age Calibration Curves 0–50,000 Years cal BP. *Radiocarbon*, *55*(4), 1869–1887. https://doi.org/10.2458/azu_js_rc.55.16947

Renforth, P., & Henderson, G. (2017). Assessing ocean alkalinity for carbon sequestration. *Reviews of Geophysics*, *55*(3), 636–674. https://doi.org/https://doi.org/10.1002/2016RG000533

Revelle, R., & Suess, H. E. (1957). Carbon Dioxide Exchange Between Atmosphere and Ocean and the Question of an Increase of Atmospheric CO2 during the Past Decades. *Tellus*, *9*(1), 18–27. https://doi.org/10.1111/j.2153-3490.1957.tb01849.x

Ronge, T. A., Tiedemann, R., Lamy, F., Köhler, P., Alloway, B. V., De Pol-Holz, R., Pahnke, K., Southon, J., & Wacker, L. (2016). Radiocarbon constraints on the extent and evolution of the South Pacific glacial carbon pool. *Nature Communications*, *7*(1), 11487. https://doi.org/10.1038/ncomms11487

Rose, K. A., Sikes, E. L., Guilderson, T. P., Shane, P., Hill, T. M., Zahn, R., & Spero, H. J. (2010). Upper-ocean-to-atmosphere radiocarbon offsets imply fast deglacial carbon dioxide release. *Nature*, *466*(7310), 1093–1097. https://doi.org/10.1038/nature09288

Roth, R., & Joos, F. (2013). A reconstruction of radiocarbon production and total solar irradiance from the Holocene ^{14}C and CO_2 records: Implications of data and model uncertainties. *Climate of the Past*, *9*(4), 1879–1909. https://doi.org/10.5194/cp-9-1879-2013

Roth, R., & Joos, F. (2012). Model limits on the role of volcanic carbon emissions in regulating glacial–interglacial CO2 variations. *Earth and Planetary Science Letters*, *329-330*, 141–149. https://doi.org/10.1016/j.epsl.2012.02.019

Sabine, C. L., & Tanhua, T. (2010). Estimation of Anthropogenic CO_2 Inventories in the Ocean. *Annual Review of Marine Science*, *2*(1), 175–198. https://doi.org/10.1146/annurev-marine-120308-080947

Schmittner, A., Gruber, N., Mix, A. C., Key, R. M., Tagliabue, A., & Westberry, T. K. (2013). Biology and air–sea gas exchange controls on the distribution of carbon isotope ratios (¹³C) in the ocean. *Biogeosciences*, *10*(9), 5793–5816. https://doi.org/10.5194/bg-10-5793-2013

Shakun, J. D., Clark, P. U., He, F., Marcott, S. A., Mix, A. C., Liu, Z., Otto-Bliesner, B., Schmittner, A., & Bard, E. (2012). Global warming preceded by increasing carbon dioxide concentrations during the last deglaciation. *Nature*, *484*(7392), 49–54. https://doi.org/10.1038/nature10915

Shchepetkin, A. F., & McWilliams, J. C. (2005). The regional oceanic modeling system (ROMS): A split-explicit, free-surface, topography-following-coordinate oceanic model. *Ocean Modelling*, *9*(4), 347–404. https://doi.org/10.1016/j.ocemod.2004.08.002

Siani, G., Michel, E., De Pol-Holz, R., DeVries, T., Lamy, F., Carel, M., Isguder, G., Dewilde, F., & Lourantou, A. (2013). Carbon isotope records reveal precise timing of enhanced Southern Ocean upwelling during the last deglaciation. *Nature Communications*, *4*(1), 2758. https://doi.org/10.1038/ncomms3758

Siegenthaler, U., & Miinnich, K. O. (1981). C/12 C fractionation during CO 2 transfer from air to sea. *Scope*, *16*, 246–257.

Siegenthaler, U., Stocker, T. F., Monnin, E., Lüthi, D., Schwander, J., Stauffer, B., Raynaud, D., Barnola, J.-M., Fischer, H., Masson-Delmotte, V., & Jouzel, J. (2005). Stable Carbon Cycle–Climate Relationship During the Late Pleistocene. *Science*, *310*(5752), 1313–1317. https://doi.org/10.1126/science.1120130

Sigman, D. M., & Haug, G. H. (2003). 6.18 The Biological Pump in the Past.

Sigman, D. M., Fripiat, F., Studer, A. S., Kemeny, P. C., Martínez-García, A., Hain, M. P., Ai, X., Wang, X., Ren, H., & Haug, G. H. (2021). The Southern Ocean during the ice ages: A review of the Antarctic surface isolation hypothesis, with comparison to the North Pacific. *Quaternary Science Reviews*, *254*, 106732. https://doi.org/10.1016/j.quascirev.2020.106732

Sigman, D. M., Hain, M. P., & Haug, G. H. (2010). The polar ocean and glacial cycles in atmospheric CO 2 concentration. *Nature*, *466*(7302), 47–55. https://doi.org/10.1038/nature09149

Skinner, L. C., & Bard, E. (2022). Radiocarbon as a Dating Tool and Tracer in Paleoceanography. *Reviews of Geophysics*, *60*(1), e2020RG000720. https://doi.org/10.1029/2020RG000720

Skinner, L. C., Fallon, S., Waelbroeck, C., Michel, E., & Barker, S. (2010). Ventilation of the Deep Southern Ocean and Deglacial CO2 Rise. *Science*, *328*(5982), 1147–1151. https://doi.org/10.1126/science.1183627

Sonnerup, R. E., Chang, B. X., Warner, M. J., & Mordy, C. W. (2019). Timescales of ventilation and consumption of oxygen and fixed nitrogen in the eastern tropical South Pacific oxygen deficient zone from transient tracers. *Deep Sea Research Part I: Oceanographic Research Papers*, *151*, 103080. https://doi.org/10.1016/j.dsr.2019.103080

Stott, L., Davy, B., Shao, J., Coffin, R., Pecher, I., Neil, H., Rose, P., & Bialas, J. (2019). CO2 Release From Pockmarks on the Chatham Rise-Bounty Trough at the Glacial Termination. *Paleoceanography and Paleoclimatology*, *34*(11), 1726–1743. https://doi.org/10.1029/2019PA003674

Stott, L., Southon, J., Timmermann, A., & Koutavas, A. (2009). Radiocarbon age anomaly at intermediate water depth in the Pacific Ocean during the last deglaciation. *Paleoceanography*, *24*(2), n/a–n/a. https://doi.org/10.1029/2008PA001690

Stott, L., & Timmermann, A. (2011). Hypothesized Link Between Glacial/Interglacial Atmospheric CO2 Cycles and Storage/Release of CO2-Rich Fluids From Deep-Sea Sediments. In H. Rashid, L. Polyak, & E. Mosley-Thompson (Eds.), *Geophysical Monograph Series* (pp. 123–138, Vol. 193). American Geophysical Union. https://doi.org/10.1029/2010GM001052

Stott, L. D., Harazin, K. M., & Krupinski, N. B. Q. (2019). Hydrothermal carbon release to the ocean and atmosphere from the eastern equatorial Pacific during the last glacial termination. *Environmental Research Letters*, *14*(2), 025007. https://doi.org/10.1088/1748-9326/aafe28

Studer, A. S., Mekik, F., Ren, H., Hain, M. P., Oleynik, S., Martínez-García, A., Haug, G. H., & Sigman, D. M. (2021). Ice Age-Holocene Similarity of Foraminifera-Bound Nitrogen Isotope Ratios in the Eastern Equatorial Pacific. *Paleoceanog-*

raphy and Paleoclimatology, *36*(5), e2020PA004063. https://doi.org/10.1029/2020PA004063

Stuiver, M., & Polach, H. A. (1977). Discussion Reporting of 14C Data. *Radiocarbon*, *19*(3), 355–363. https://doi.org/10.1017/S0033822200003672

Tans, P. P. (1980). On calculating the transfer of carbon-13 in reservoir models of the carbon cycle. *Tellus*, *32*(5), 464–469. https://doi.org/10.1111/j.2153-3490.1980.tb00973.x

Tans, P. P., Berry, J. A., & Keeling, R. F. (1993). Oceanic 13C/12C observations: A new window on ocean CO2 uptake. *Global Biogeochemical Cycles*, *7*(2), 353–368. https://doi.org/10.1029/93GB00053

Toggweiler, J. R., & Sarmiento, J. L. (1985). Glacial to Interglacial Changes in Atmospheric Carbon Dioxide: The Critical Role of Ocean Surface Water in High Latitudes. In *The Carbon Cycle and Atmospheric CO2: Natural Variations Archean to Present* (pp. 163–184). American Geophysical Union (AGU). https://doi.org/10.1029/GM032p0163

Trudgill, M., Nuber, S., Block, H. E., Crumpton-Banks, J., Jurikova, H., Littley, E., Shankle, M., Xu, C., Steele, R. C. J., & Rae, J. W. B. (2024). A Simple, Low-Blank Batch Purification Method for High-Precision Boron Isotope Analysis. *Geochemistry, Geophysics, Geosystems*, *25*(3), e2023GC011350. https://doi.org/10.1029/2023GC011350

van Geen, A., Smethie Jr., W. M., Horneman, A., & Lee, H. (2006). Sensitivity of the North Pacific oxygen minimum zone to changes in ocean circulation: A simple model calibrated by chlorofluorocarbons. *Journal of Geophysical Research: Oceans*, *111*(C10). https://doi.org/10.1029/2005JC003192

Veneziani, M., Edwards, C. A., Doyle, J. D., & Foley, D. (2009). A central California coastal ocean modeling study: 1. Forward model and the influence of realistic versus climatological forcing. *Journal of Geophysical Research: Oceans*, *114*(C4). https://doi.org/10.1029/2008JC004774

Virtanen, P., Gommers, R., Oliphant, T. E., Haberland, M., Reddy, T., Cournapeau, D., Burovski, E., Peterson, P., Weckesser, W., Bright, J., van der Walt, S. J., Brett, M., Wilson, J., Millman, K. J., Mayorov, N., Nelson, A. R. J., Jones, E., Kern, R., Larson, E., ... van Mulbregt, P. (2020). SciPy 1.0: Fundamental

algorithms for scientific computing in Python. *Nature Methods*, *17*(3), 261–272. https://doi.org/10.1038/s41592-019-0686-2

Vogel, J. C., Grootes, P. M., & Mook, W. G. (1970). Isotopic fractionation between gaseous and dissolved carbon dioxide. *Zeitschrift für Physik A Hadrons and nuclei*, *230*, 225–238.

Walczak, M. H., Mix, A. C., Cowan, E. A., Fallon, S., Fifield, L. K., Alder, J. R., Du, J., Haley, B., Hobern, T., Padman, J., Praetorius, S. K., Schmittner, A., Stoner, J. S., & Zellers, S. D. (2020). Phasing of millennial-scale climate variability in the Pacific and Atlantic Oceans. *Science*, *370*(6517), 716–720. https://doi.org/10.1126/science.aba7096

Wang, H., Pilcher, D. J., Kearney, K. A., Cross, J. N., Shugart, O. M., Eisaman, M. D., & Carter, B. R. (2023). Simulated Impact of Ocean Alkalinity Enhancement on Atmospheric CO2 Removal in the Bering Sea. *Earth's Future*, *11*(1), e2022EF002816. https://doi.org/10.1029/2022EF002816

Wanninkhof, R. (1992). Relationship between wind speed and gas exchange over the ocean. *Journal of Geophysical Research: Oceans*, *97*(C5), 7373–7382. https://doi.org/10.1029/92JC00188

Wanninkhof, R. (2014). Relationship between wind speed and gas exchange over the ocean revisited. *Limnology and Oceanography: Methods*, *12*(6), 351–362. https://doi.org/10.4319/lom.2014.12.351

Webb, J. R., Maher, D. T., & Santos, I. R. (2016). Automated, in situ measurements of dissolved CO_2 , CH_4 , and ^{13} C values using cavity enhanced laser absorption spectrometry: Comparing response times of air-water equilibrators. *Limnology and Oceanography: Methods*, *14*(5), 323–337. https://doi.org/10.1002/lom3.10092

Westerhold, T., Marwan, N., Drury, A. J., Liebrand, D., Agnini, C., Anagnostou, E., Barnet, J. S. K., Bohaty, S. M., De Vleeschouwer, D., Florindo, F., Frederichs, T., Hodell, D. A., Holbourn, A. E., Kroon, D., Lauretano, V., Littler, K., Lourens, L. J., Lyle, M., Pälike, H., … Zachos, J. C. (2020). An astronomically dated record of Earth's climate and its predictability over the last 66 million years. *Science*, *369*(6509), 1383–1387. https://doi.org/10.1126/science.aba6853

Xu, C., Jurikova, H., Nuber, S., Steele, R. C. J., Trudgill, M., Barker, S., Lear, C. H., Burke, A., & Rae, J. (2024). A Rapid, Simple, and Low-Blank Pumped Ion-

Exchange Column Chromatography Technique for Boron Purification From Carbonate and Seawater Matrices. *Geochemistry, Geophysics, Geosystems*, *25*(2), e2023GC011228. https://doi.org/10.1029/2023GC011228

Yu, J., Anderson, R. F., Jin, Z., Rae, J. W. B., Opdyke, B. N., & Eggins, S. M. (2013). Responses of the deep ocean carbonate system to carbon reorganization during the Last Glacial–interglacial cycle. *Quaternary Science Reviews*, *76*, 39–52. https://doi.org/10.1016/j.quascirev.2013.06.020

Yu, J., Broecker, W. S., Elderfield, H., Jin, Z., McManus, J., & Zhang, F. (2010). Loss of Carbon from the Deep Sea Since the Last Glacial Maximum. *Science*, *330*(6007), 1084–1087. https://doi.org/10.1126/science.1193221

Yu, J., Elderfield, H., & Piotrowski, A. M. (2008). Seawater carbonate ion-13C systematics and application to glacial–interglacial North Atlantic ocean circulation. *Earth and Planetary Science Letters*, *271*(1), 209–220. https://doi.org/10.1016/j.epsl.2008.04.010

Zachos, J. (2001). Trends, Rhythms, and Aberrations in Global Climate 65 Ma to Present. *Science*, *292*(5517), 686–693. https://doi.org/10.1126/science.1059412

Zeebe, R. E., Wolf-Gladrow, D. A., & Jansen, H. (1999). On the time required to establish chemical and isotopic equilibrium in the carbon dioxide system in seawater. *Marine Chemistry*, *65*(3), 135–153. https://doi.org/10.1016/S0304-4203(98)00092-9

Zeebe, R. E., & Wolf-Gladrow, D. (2001). *CO2 in seawater: Equilibrium, kinetics, isotopes* (Vol. 65). Gulf Professional Publishing.

Zhang, J., & Quay, P. D. (1995). Carbon isotope fractionation during gas-water exchange and dissolution of CO, 8.

Zhao, N., & Keigwin, L. D. (2018). An atmospheric chronology for the glacial-deglacial Eastern Equatorial Pacific. *Nature Communications*, *9*(1), 3077. https://doi.org/10.1038/s41467-018-05574-x

Zhao, N., Marchal, O., Keigwin, L., Amrhein, D., & Gebbie, G. (2018). A Synthesis of Deglacial Deep-Sea Radiocarbon Records and Their (In)Consistency With Modern Ocean Ventilation. *Paleoceanography and Paleoclimatology*, *33*(2), 128–151. https://doi.org/10.1002/2017PA003174

Zhou, M., Tyka, M. D., Ho, D. T., Yankovsky, E., Bachman, S., Nicholas, T., Karspeck, A. R., & Long, M. C. (2024). Mapping the global variation in the efficiency

of ocean alkalinity enhancement for carbon dioxide removal. *Nature Climate Change*, 1–7. https://doi.org/10.1038/s41558-024-02179-9